DEVELOPMENT OF A VARIABLE-TEMPERATURE ION MOBILITY/ TIME-OF-FLIGHT MASS SPECTROMETER FOR SEPARATION OF ELECTRONIC ISOMERS

A Dissertation

by

GUIDO FRIDOLIN VERBECK, IV

Submitted to the Office of Graduate Studies of
Texas A&M University
in partial fulfillment of the requirements for the degree of

DOCTOR OF PHILOSOPHY

May 2005

Major Subject: Chemistry

DEVELOPMENT OF A VARIABLE-TEMPERATURE ION MOBILITY/ TIME-OF-FLIGHT MASS SPECTROMETER FOR SEPARATION OF ELECTRONIC ISOMERS

A Dissertation

by

GUIDO FRIDOLIN VERBECK, IV

Submitted to the Office of Graduate Studies of
Texas A&M University
in partial fulfillment of the requirements for the degree of

DOCTOR OF PHILOSOPHY

Approved as to style and content by:

David H. Russell (Chair of Committee)	Simon W. North (Member)
Paul S. Cremer (Member)	Emile A. Schweikert (Head of Department)
David A. Church (Member)	

May 2005

Major Subject: Chemistry

ABSTRACT

Development of a Variable-Temperature Ion Mobility/ Time-of-Flight Mass Spectrometer for Separation of Electronic Isomers. (May 2005)

Guido Fridolin Verbeck, IV, B.S., Northeast Louisiana University;

M.S., University of Alabama at Birmingham

Chair of Advisory Committee: Dr. David H. Russell

The construction of a liquid nitrogen-cooled ion mobility spectrometer coupled with time-of-flight mass spectrometry was implemented to demonstrate the ability to discriminate between electronic isomers. Ion mobility allows for the separation of ions based on differing cross-sections-to-charge ratio. This allows for the possible discrimination of species with same mass if the ions differ by cross-section. Time-of-flight mass spectrometry was added to mass identify the separated peak for proper identification.

A liquid nitrogen-cooled mobility cell was employed for a two-fold purpose. First, the low temperatures increase the peak resolution to aid in resolving the separated ions. This is necessary when isomers may have similar cross-sections. Second, low temperature shortens the mean free path and decreases the neutral buffer gas speeds allowing for more interactions between the ions and the drift gas. Kr^{2+} study was performed to verify instrument performance.

The variable-temperature ion mobility spectrometer was utilized to separate the distonic and conventional ion forms of CH_3OH, CH_3F, and CH_3NH_2 and to discriminate between the keto and enol forms of the acetone radical cation. Density functional theory

and *ab initio* calculations were employed to aid in proper identification of separating isomers. Monte Carlo integration tools were also developed to predict ion cross-section and resolution within a buffer gas.

DEDICATION

This dissertation is dedicated to my loving family: my wife, Gennie Pair Verbeck, who has endured my many years of graduate school, and truly supported me every step of the way, my daughter, Annah Van Duyn Verbeck, who brightens my life everyday, and inspires me to be the best I can be, my father, The Rev. Guido Verbeck, III, who's faith in me and God has inspired me through this journey, and my late Grandmother, Dorothea Van Duyn Verbeck, who taught me that education is the greatest door opener. To these people, thank you.

ACKNOWLEDGEMENTS

I must first acknowledge my advisor, Professor David H. Russell for his inspirational advice and support throughout my graduate studies. His guidance and council helped me become a better chemist. I would like to thank the whole Russell research group, especially my classmates Brandon Ruotolo and Holly Sawyer, who shared the graduate path with me, and to my mentees, Jody May and Kate Stumpo who allowed me to share my graduate experiences. I would also like to thank my committee for their contribution of time and comment on my research project, especially Dr. Paul Cremer and Dr. Simon North for their open door policy, allowing many meaningful discussions and thoughts. I would like to acknowledge the support of Dr. Michael Hall and the Laboratory for Molecular Simulations, especially Dr. Lisa Perez and Dr. Charles Webster, who spent much time developing my computational skills. Lastly, I would like to thank Tony Montalbano and Ken Greer for all their help and guidance in machining. Without the support of the great departmental shops, this dissertation could not have been completed.

TABLE OF CONTENTS

Page

CHAPTER Page

Page

LIST OF FIGURES

Page

Page

Page

Page

LIST OF TABLES

Page

CHAPTER I

INTRODUCTION

Background

Ion mobility spectrometry (IMS) has been utilized for a wide range of ion separations for many years.[1-3] In recent years, however, the utility of IMS as a structural probe for a broad range of studies of gas-phase ions (*i.e.,* studies of small organic ions[4,5] to peptides, protein, and DNA) has emerged. [6-12] Recent work by Bowers,[9] Jarrold,[6] Clemmer,[7] and Russell[11] firmly establishes IMS combined with mass spectrometry (MS) and computational chemistry methods as powerful structural probe techniques for large molecules, but earlier work on $C_2H_5O^+$ isomers of Harland and coworkers[13] illustrate the ability of IMS to separate small gas-phase ions (<100 m/z) on the basis of structure dependent collision cross-sections. Many reports have focused on structural determination of gas-phase ions by mass spectrometry, but in most cases structural information is derived from ions containing sufficient internal energies to dissociate with unimolecular rate constants of $>10^5$ s^{-1}, energies of several eV above the ground state. On the other hand, IM-MS can be used to investigate ions having low internal energies, and using variable temperature IM-MS it may be possible to probe the energetics of inter-conversion processes, *i.e.,* electronic and/or structural rearrangement reactions.[14-16]

In this chapter a fundamental introduction to ion mobility will be presented. Current trends in analytical nomenclature and calculations from groups active in this field will also be reviewed. The added degree of orthogonality and analysis of 2-D IM-

---

This dissertation follows the style of *The Journal of Physical Chemistry.*

MS data will be illustrated by an IM-TOF spectrum of a carbon cluster mixture and a peptide mixture.

Ion Mobility

The mobility (K) of an ion through a neutral buffer gas is defined as the ratio of drift velocity (v_d) to applied electric field (E_o).[17]

$$K = \frac{v_d}{E_o} \tag{1}$$

To facilitate comparisons of mobility values obtained under different experimental conditions, mobility is usually reported as the reduced mobility, *i.e.,* the mobility at standard temperature and pressure.

$$K_O = \frac{p}{760}\frac{273.15}{T}K \tag{2}$$

As the collision energy approaches the thermal energy of the system, then the ion mobility approaches the so-called "low-field" limit.[18] In the low-field limit, an ion's mobility is inversely proportional to the collision cross-section (Ω_o), and to the square root of the reduced mass of the neutral and the ion collision pair (μ).

$$K = \frac{3}{16}\frac{q}{N}\left(\frac{1}{\mu}\frac{2\pi}{k_b T}\right)^{\frac{1}{2}}\frac{1}{\Omega_O} \tag{3}$$

Where N is the number density of the drift gas, q is the ion charge, k_b is Boltzmann's constant, and T is the temperature of the system. Although the collision cross-section can be relatively simple for large molecules, where the cross-section is correlated to the "hard-sphere" cross-section of the ion, the cross-section for atomic and small molecular ions must include all related interaction potentials.[19]

For large molecules (>500 amu) a trajectory cross-section (approximated by simple hard-sphere) accurately predicts an ion's collision size in a neutral drift gas. However for smaller molecules, the interaction of the ion with the neutral drift gas must be considered.[16] Chapman and Enskog developed the theory used to evaluate elastic collisions between and ion and neutral in a uniform electric field.[13,20] The collision cross-section can be determined by solving a triple integral involving the relative collision energy (E'), impact parameter (b), deflection angle (θ(b,E')), internuclear distance (r), and ion neutral interaction potential (V(r)).

$$\Omega^{(1,1)} = \frac{1}{2(k_b T)^3}\int_0^\infty E'^2\, Q^{(1)}(E')\exp\left(\frac{-E'}{k_b T}\right)dE' \tag{4}$$

$$Q^{(1)}(E') = 2\pi\int_0^\infty \left(1-\cos\theta(b,E')\right)bdb \tag{5}$$

$$\theta(b,E') = \pi - 2b\int_{r_0}^\infty \left(1-\frac{b^2}{r^2}-\frac{V(r)}{E'}\right)^{-\frac{1}{2}}\frac{dr}{r^2} \tag{6}$$

To accurately predict these cross-sections, a suitable interaction potential must be chosen. Bowers *et al.* developed a generalized potential equation for ion-molecule collisions,[21] which includes ion-induced dipole, dipole-induced dipole, and centrifugal capture of the neutral.

$$V(r) = \varepsilon\left(\left(\frac{r_o}{r}\right)^{12} - 2\left(\frac{r_o}{r}\right)^6\right) - \frac{\alpha_p dq}{8\pi\varepsilon_o r^5} - \frac{\alpha_p q^2}{8\pi\varepsilon_o r^4} + \frac{L}{2\mu r^2}^2 \tag{7}$$

The terms of this equation include potential well depth (ε), polarizability of the neutral (α_p), dipole of the ion (d), orbital angular momentum (L), and gas permittivity of free

space (ε_o). Equations 4 to 7 provide an accurate approximation of the collision cross-section of small spherical ions, from which ion mobilities (K) can be calculated.

Ion Mobility Spectrometry has become an important analytical tool over the past 25 years.[22] Known also as plasma chromatography and ion chromatography[2], it has mainly been applied to the analysis of volatile organic compounds[23,24] and used as a tool to probe the electronic states of ions[25]. Recently, IM has been applied to the analysis of biomolecules employing electrospray ionization (ESI)[26-29] and matrix-assisted laser-desorption ionization (MALDI) sources[30-32]. These combined with mass spectrometry create a powerful tool in the analysis of ion-molecule reaction chemistry, volatile organics, and the separation of proteins and peptides.

IM-MS Data Analysis

When developing a multi-dimensional technique, it is desirable that the dimensions evaluate unrelated molecular properties of the analyte of interest. When the dimensions of a technique are completely independent of each other they are said to be orthogonal[33]. If the molecular properties analyzed by the dimensions are not completely unrelated a multi-dimensional technique can be reduced to a one-dimensional technique with signal distributed along a diagonal. As can be seen from the mass-mobility plot of C_{60}/C_{70}, shown Figure 1, the signal is distributed along a trend line, indicating that the dimensions of IM-MS have a large amount of cross-information i.e. there is a high degree of correlation between the mobility and mass of an ion.

The large amount of cross-information present in a mass-mobility plot does not reduce the utility of IM-MS, rather the cross-information guides the analysis of the

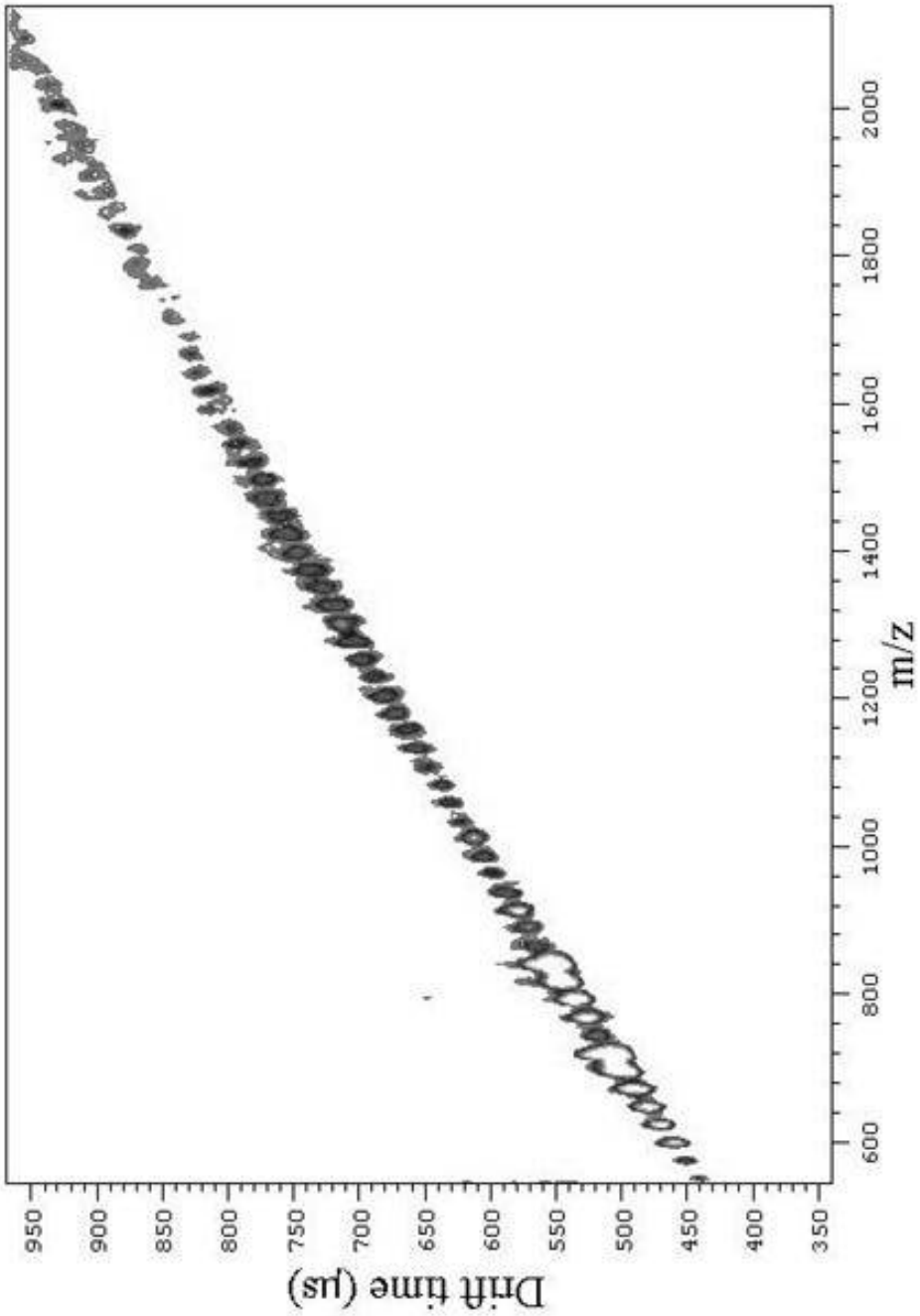

Figure 1. MALDI-IM-TOF mass spectra of carbon cluster fragments from 90% C_{60} to 10% C_{70}.

complex mixture[34]. For example, the analysis of complex mixtures is often directed by the presence of multiple trend lines in a mass-mobility data set, as illustrated by figure 2, which combines trend lines for both peptides and carbon cluster fragment ions. Trend lines are present in the mass-mobility plots due to the high correlation between an ion's mass and collision cross-section. Addition of mass within an ion series can be likened to adding subunits to a polymer; as the subunits are added the gas-phase volume is increased in a linear fashion over a limited mass range. C_{60} and related carbon clusters have a very tight and uniform (spherical) conformation, resulting in a highly linear mass-mobility trend, whereas peptide ions have a more open conformation. Due to the differences in which different ion classes increase their collision cross-section upon mass addition different trend lines result.

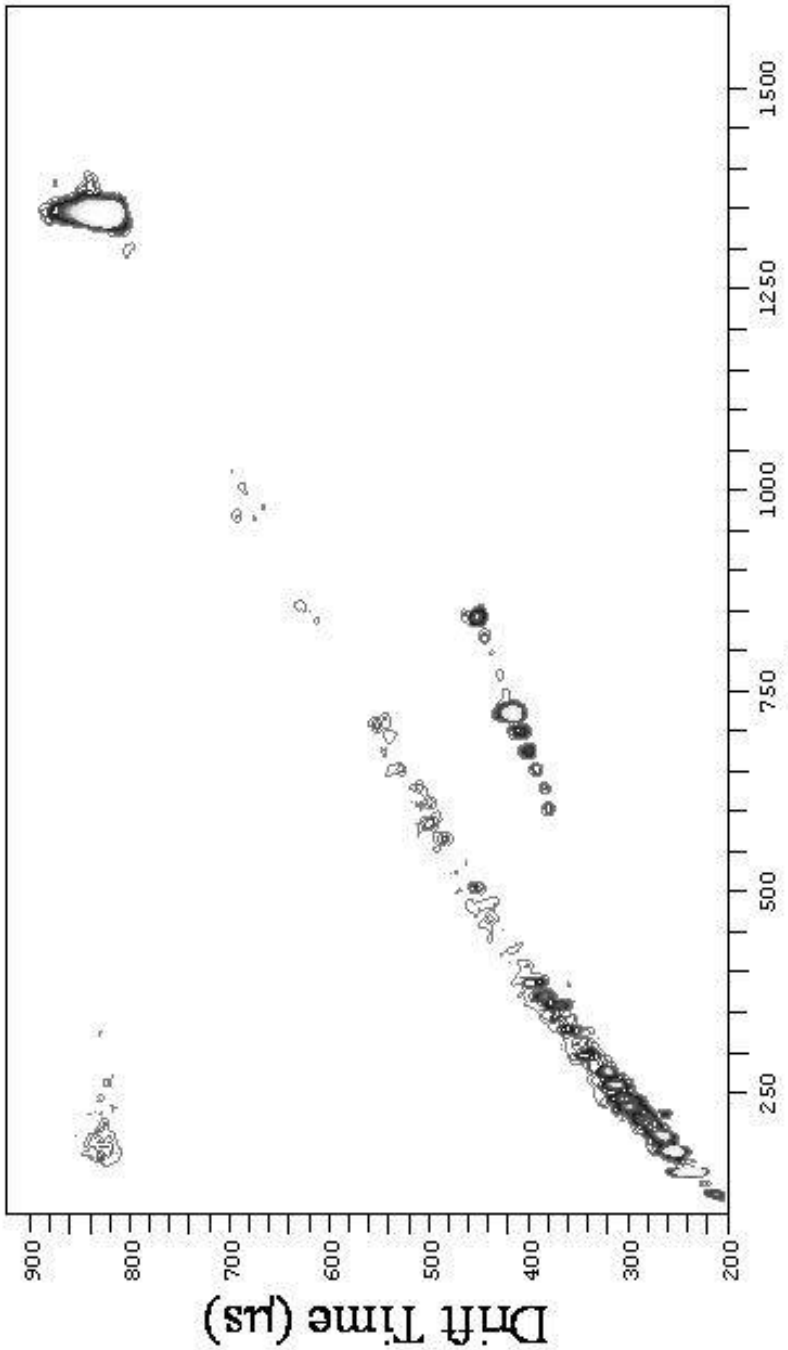

Figure 2. MALDI-IM-TOF mass spectra of the peptide, substance P, with carbon cluster fragments from 90% C_{60} to 10% C_{70}.

CHAPTER II

RESOLUTION EQUATIONS APPLIED TO HIGH-FIELD ION MOBILITY

Background

Separations based on the mobility of an ion through a neutral buffer gas (*i.e.*, ion mobility spectrometry (IMS))[2,22] has become an important technology for separation of long-lived electronic states of gas-phase ions and a sensitive method for detection of air-borne species.[3,25] Recent work which demonstrates the utility of IMS for analyzing gas-phase ionized biopolymers (*i.e.*, peptides, proteins, DNA, etc.) has renewed interest in the analytical applications and led to development of several high-resolution drift tube designs.[26-32] In order to effect separation of near-thermal populations of structural isomers of gas-phase ions, most IMS measurements are performed near the low-field limit. The advantage of operating under low-field conditions is that band broadening is limited to longitudinal diffusion and, these conditions minimize adverse effects of ion activation by ion-neutral collisions.

The use of IMS can be divided into two pressure regimes, *viz.* high pressure (typically low-field) and low pressure (either low or high applied fields), and there are distinct advantages associated with both pressure regimes. At high pressure, the number of ion-neutral collisions is high (about 1.87×10^{10} collisions/s for C_{60} in 760 torr He) and the probability of unwanted collisions with gas impurities is increased relative to low pressure conditions (about 2.45×10^{7} collisions/s for C_{60} in 1 torr He). For example, in a 30cm drift cell maintained at 760 torr He, C_{60} will collide with an impurity of 0.01%

about $6.4x10^5$ times, but at 1 torr He, C_{60} will collide about 11 times. An advantage of low pressure drift tube design is the ease of coupling ion mobility with high vacuum mass spectrometers. High vacuum ion sources and mass spectrometers have been developed for mass selection and ion injection, which is more difficult at high pressures. Lastly, high field mobility decreases ion separation times, leading to higher throughput analysis (approximately 3 orders of magnitude faster for analysis times at 1 torr over 760 torr).

According to Wannier, low-field is defined in terms of the kinetic energy acquired by the ion in the presence of an applied field (E_o). That is, the translational energy gained by the ions between collisions should be less than the thermal energy of the collision gas,[35-36]

$$eE_o\lambda << k_bT \tag{8}$$

where e is the charge on the ion, k_b is Boltzmann's constant, and T is the collision gas temperature. Wannier further describes the mass dependence of the above inequality by expressing equation 8 in terms of drift gas pressure (p) and collision cross-section (σ) rather than the mean free path (λ).

$$\frac{E_o}{p} << \frac{\sigma}{e}\frac{mM}{m^2+M^2} \tag{9}$$

where m is the mass of the ion and M is the mass of the neutral drift gas. Using Eq.9, the low-field limit for a range of masses, pressures, and applied electric fields can be predicted. For example, the low-field limit is generally assumed to be 2 V/cm•torr for

atomic species, but for peptide ions in the m/z range 500-2500, the low field limit ranges from 15-45 V/cm•torr.

This report describes ion mobility resolution under high-field conditions by applying Wannier's diffusion relation to the known expression for ion mobility (IM) resolution. The resulting equation is applicable to IM separations over a much broader range of field conditions. A detailed examination of this new expression suggests that resolution for ions that have low mobilities (*i.e.,* large protein and peptide ions) approach the theoretical low-field resolution, even at high E/p, where small ions exhibit a decrease in resolution.

In addition, the effect of drift tube temperature on resolution as a function of the mobility of the ion is briefly considered, as it is known that resolution under low-field conditions varies as $1/T^{1/2}$. Also, Wannier's diffusion relations indicate that radial diffusion under high-field conditions will be greater than low-field conditions, leading to a decrease of ion transmission in the high-field limit. We examine both figures of merit, resolution and transmission efficiency, in the evaluation of IM separation performed at high E/p.

Theory

The mobility (K) of an ion through a neutral drift gas is determined by the ion's drift velocity (v_d) and applied electric field;[1]

$$v_d = \frac{L}{t_d} = KE_o \qquad (10)$$

where the ion's mobility (K) is described by Revercomb and Mason[37] to be proportional to the reduced mass (μ) of the ion and neutral drift gas, and the collision integral (Ω_o).

$$K \propto \frac{1}{\mu\Omega_o} \tag{11}$$

Mobility resolution has been derived for low-field applications;[38-40] however, high applied fields and low pressure have a distinct effect on mobility resolution.

IM Resolution is usually defined in terms of a single peak;[40]

$$R = \frac{L}{W_{1/2}} \tag{12}$$

where, L is the drift length and $W_{1/2}$ is the peak width at half maximum. The peak width depends on four broadening terms: the initial pulse, diffusion, space charge effects, and ion-molecule reactions.[39] If we assume that the initial ion gate width is narrow with respect to the peak width, the number of ions in each ion packet is low, and the ion-neutral interaction potential with the bath gas is negligible, then we can assume the band broadening is limited to the diffusion term.

$$W \cong W_d \tag{13}$$

A general diffusion profile can be obtained by solving Fick's second law of diffusion (eq. 14) provided that the diffusion coefficient (D) is constant for a particular system (no pressure gradients).[41]

$$\frac{\partial N_i}{\partial t} = -D\frac{\partial^2 N_i}{\partial z^2} \tag{14}$$

The left hand side of the equation is the rate of transfer of ions per unit area per unit time along the z direction and N_i is the number density of ions per unit volume. Assuming

that the diffusion of ions is equal in both directions along the z axis,[41] integration of eq. 14 results in:

$$N_i(x,t_d) = \frac{M}{2\sqrt{\pi D t_d}} e^{\frac{-(x-L)^2}{4Dt_d}} \tag{15}$$

The above distribution equation of the total ion concentration M traveling the drift length L at time t_d can be compared to the Gaussian distribution profile to solve for the peak variance (σ).

$$\sigma = \sqrt{2Dt_d} \tag{16}$$

Knowing that the FWHM (full width at half max) is equal to 2.35 times the variance for a normal Gaussian distribution, we can add the diffusion term (eq. 16) to the peak resolution (eq. 12).

$$R = \frac{L}{3.32\sqrt{Dt_d}} \tag{17}$$

By solving (eq.10) for the drift length (L) and substituting in the resolution equation (eq. 13), we can evaluate the effect of mobility, diffusion, and applied electric field on the peak resolution.[38]

$$R = \frac{KE_o}{3.32}\sqrt{\frac{t_d}{D}} \tag{18}$$

Under low-field conditions, the diffusion coefficient can be approximated by the Nernst-Einstein-Townsend relation.[38]

$$D = \frac{k_b T}{q} K \tag{19}$$

where q is the charge, k_b the Boltzmann constant, and T is the temperature. Temperature is assumed to be the same for both the bath gas and the ion at low field. If we assume that we are in this "low-field limit", then the resolution equation simplifies to:[38]

$$R = 32.33\sqrt{\frac{LE_o q}{T}} \tag{20}$$

where q is the charge number of the ion.

Wannier used the Boltzmann equation to describe the effect of high applied fields on ion diffusion through a neutral drift gas. Wannier calculated the diffusion, both axially (D_z) and radially (D_r), using an isotropic scattering model.[35-36, 42]

$$D_z = \frac{k_b T}{q} K + \frac{M}{3} \cdot \frac{M + 3.2m}{M + 1.908m} \cdot \frac{E^2 K^3}{q} \tag{21}$$

$$D_r = \frac{k_b T}{q} K + \frac{M}{3} \cdot \frac{M + m}{M + 1.908m} \cdot \frac{E^2 K^3}{q} \tag{22}$$

This more complete model of diffusion changes significantly the peak broadening at higher E/p. Also, Equation 22 reduces to the Einstein relation at diminishing applied fields. Here, we utilize Wannier's relations to derive equations to predict mobility peak widths at a variety of field strengths and propose that increased mobility resolution is possible under low pressure conditions.

For completeness, we also consider ion transmission, because it plays a large role on instrument design. Percent ion transmission is defined in terms of Equation 23:[42]

$$\%T = \left(1 - \exp\frac{-r^2}{4D_r t}\right)100 \tag{23}$$

We use Wannier's radial diffusion term to evaluate the broadening of the ion packet and calculate the number of ions that will transmit through the exit orifice (r). Since we know that drift time is directly proportional to drift length (eq. 8), we can see that longer drift cells will decrease transmission. This needs to be accounted for when developing a mobility instrument that fits specific resolution requirements.

Experimental Methods

Ion mobility data was acquired using a matrix-assisted laser desorption ionization (MALDI)-ion mobility (IM)-orthogonal- time-of-flight (o-TOF)- mass spectrometer (MS) built in-house and described elsewhere.[43] Briefly, ions are created at the operating pressure of the drift tube (1 torr He) and allowed to drift over 45 cm in the presence of a superimposed linear and non-linear electric fields.[40] Ions that exit the drift cell are sampled with a 30cm orthogonal TOF for detection and mass analysis. Data is collected using a custom data acquisition software package (Ionwerks, Inc. Houston, TX.) and processed using Transform (IDL, Research Systems, Boulder, CO.). C_{60}/C_{70} and bradykinin were purchased from Sigma-Aldrich (St. Louis, MO.) and used without additional purification. MALDI was performed by diluting a 100 picomole/μL stock solution of bradykinin with a solution of α-cyano-4-hydroxycinnamic acid to a matrix-to-analyte ratio of 2000:1.

The low mass and temperature controlled studies were carried out on a liquid nitrogen-cooled ion mobility orthogonal- time-of-flight mass spectrometer built in-house.[44] The samples are ionized using electron impact and separated in the drift tube at

a constant buffer gas concentration equal to 1 torr at room temperature. The data acquisition package is the same as described above.

Unknown mobility, resolution, diffusion, and transmission values were calculated using a predictive software package called "MobCross" developed at Texas A&M University. This package utilizes known and derived equations to calculate mobility values. It also employs a Monte Carlo simulation to predict ion cross-sections based on *ab initio* and molecular mechanic calculations.[19]

Results and Discussion

In order to evaluate the effects of different control variables on resolution, we need to combine the resolution equation (eq. 18) with Wannier's relation (eq. 21). To reduce the number of terms in Wannier's relation, we condensed the mass term to μ_w, where

$$\mu_w = \frac{m}{3}\frac{m+3.2M}{m+1.908M} \tag{24}$$

$$D_z = \frac{k_b T}{q}K + \mu_w \cdot \frac{E^2K^3}{q} \tag{25}$$

Equation 25 is substituted into equation 18 and simplified.

$$R = 0.301\left(\frac{qLE}{k_bT + \mu_w E^2K^2}\right)^{\frac{1}{2}} \tag{26}$$

Equation 26 represents the broader resolution equation for both low and high-field mobility.

Figure 3A illustrates the large differences between the diffusion for the Nernst-Einstein Relation (eq. 19) and Wannier's relation (eq. 21). The calculations were

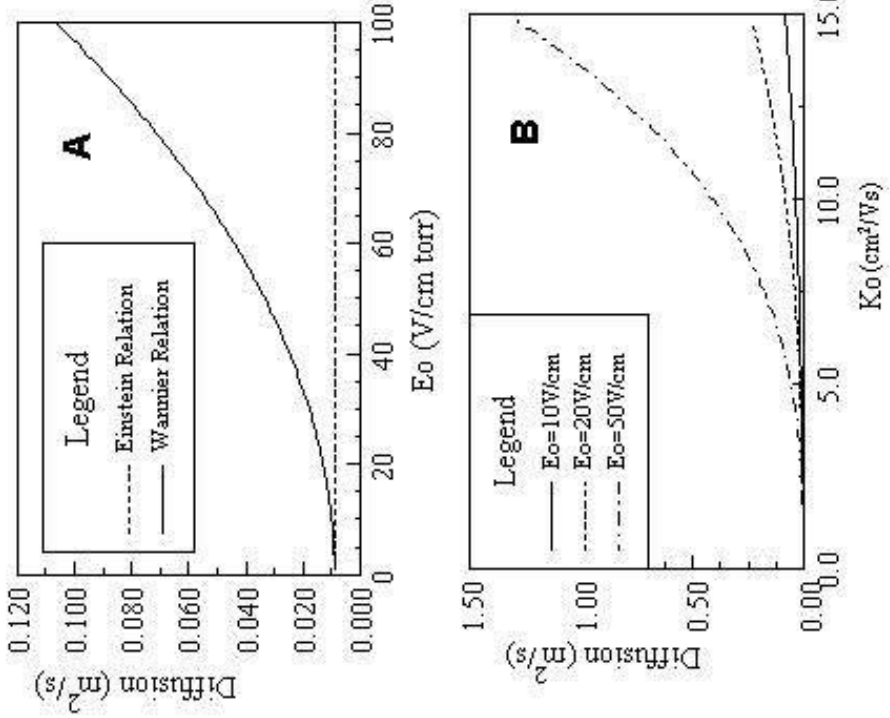

Figure 3. A) Plot of diffusion versus applied field (E_o) at 1 torr drfit pressure for C_{60}. B) Plot of diffusion as a function of reduced mobility for a 15cm drift cell at 1 torr for applied fields of 10, 20, and 50V/cm.

performed for C_{60} ion in a helium drift gas, using a m/z value of 720 and a mobility of 4.31 cm^2/Vs.[45-46] The deviation of the two diffusion relations begins at about 2 V/cm·torr and exceeds three orders of magnitude at fields greater than 40 V/cm·torr. Using Wannier's relation we see that the diffusion changes as a function of the square of the applied field, but also as the cube of the mobility of the ion. Figure 3B, which contains a plot of diffusion versus reduced mobility (K_o) for a range of field strengths, shows that as the mobility of the ion approaches zero, Wannier's relation (eq. 21) approaches the Einstein relation (eq. 19).

Differences in longitudal diffusion also cause dramatic changes in the resolution of the high-field ion mobility measurements. Figure 4A shows the effect of E_o on resolution. Because the Nernst-Einstein relation is independent of applied field, the resolution calculated using equation 19 results in a sizable error in the high-field range. For example, at 60V/cm•torr the calculated resolution would be 45% of the predicted Einstein relation value. On the other hand, Wannier's relation yields substantial improvement over the Nernst-Einstein relation in predicting resolution over a broad range of applied fields. As can be seen in Figure 4A, the resolution reaches a maximum value and then reduces as the applied field is increased; however, this local maximum changes as a function of the mobility. Figure 4B illustrates that at high K_o an increase in E/p results in a decrease in resolution, whereas for ions having a mobility approaching zero, the resolution increases as E/p is increased. Intermediate mobility values display a cross-over point that shows an increase in resolution up to a point, beyond which the

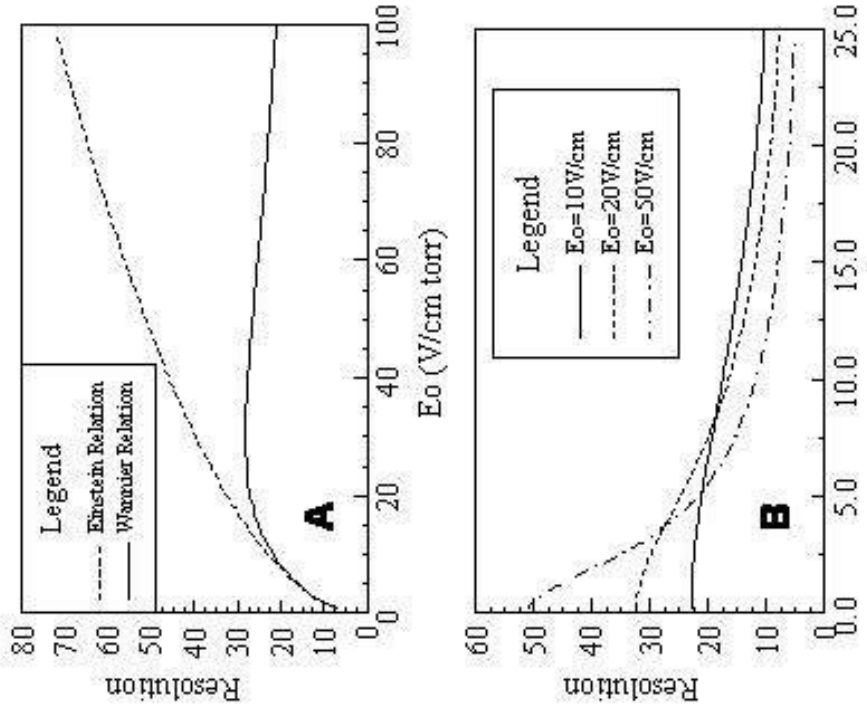

Figure 4. A) Plot of predicted resolution versus applied field for C_{10} at 1 torr drift pressure. B) The resolution versus reduced mobility of a 15cm drift cell at 1 torr for applied fields of 10, 20, and 50W/cm.

resolution decreases. Therefore, as the mobility approaches zero, resolution can be estimated using the Nernst-Townsend-Einstein equation (eq. 30).

Equation 26 is best utilized to obtain an accurate resolution estimate under varying field conditions for a broad range of ions. For ions having $K_o > 1$, it is imperative to use equation 26 in the high field region to obtain accurate resolutions. Figure 5 illustrates the resolution of He^+ in 1 torr He drift gas as a function of E/p. The IM resolution is observed to decrease as the applied field is increased, exhibiting a drop of 38% from 2 V/cm to 10V/cm. This decrease in resolution as a function of increased applied field is contrary to the low-field resolution equation (eq. 20), where resolution should increase with increasing field strength. However, equation 26 explains this trend of decreasing resolution for increasing applied fields for small molecular and atomic ions (large mobilities). The contribution of the ion-neutral interaction is not negligible in this case, due to a charge-exchange mechanism under these conditions.[44]

Figure 6 reproduces the low field and high field approximations from Figure 4A. In addition, experimental data for $C_{60}^{+\bullet}$ is presented for comparison. Within the error of the resolution measurement (expressed as a range over multiple values at a single field strength), the observed experimental trend more closely matches the predicted value from equation 26, than those of equation 20. For example at E/p of 50 V/cm•torr the resolution difference is 4 for the high field prediction, but a difference of 18 compared to the low field estimate.

Resolution for large molecules (low mobility) can be estimated using the low-field equations, and equation 20 becomes an accurate approximation of resolution.

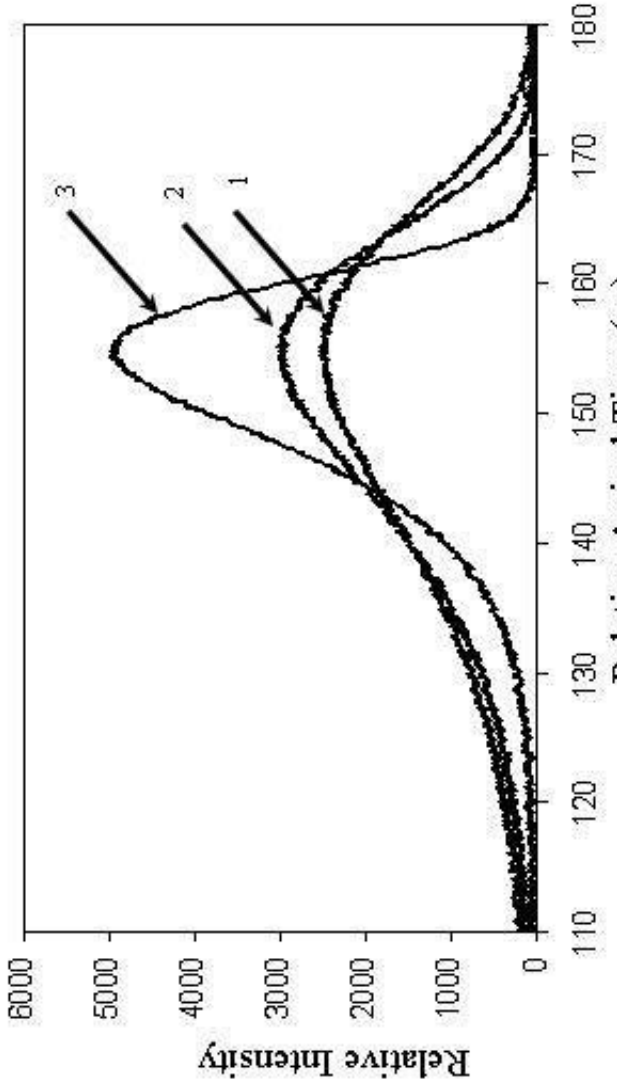

Figure 5. Plot of He^+ in He at 1 torr. 1.) Resolution of 4.8 at E/p=10V/cm*torr 2.) Resolution of 6.5 at E/p=5V/cm*torr 3.)Resolution of 7.8 at 2V/cm*torr.

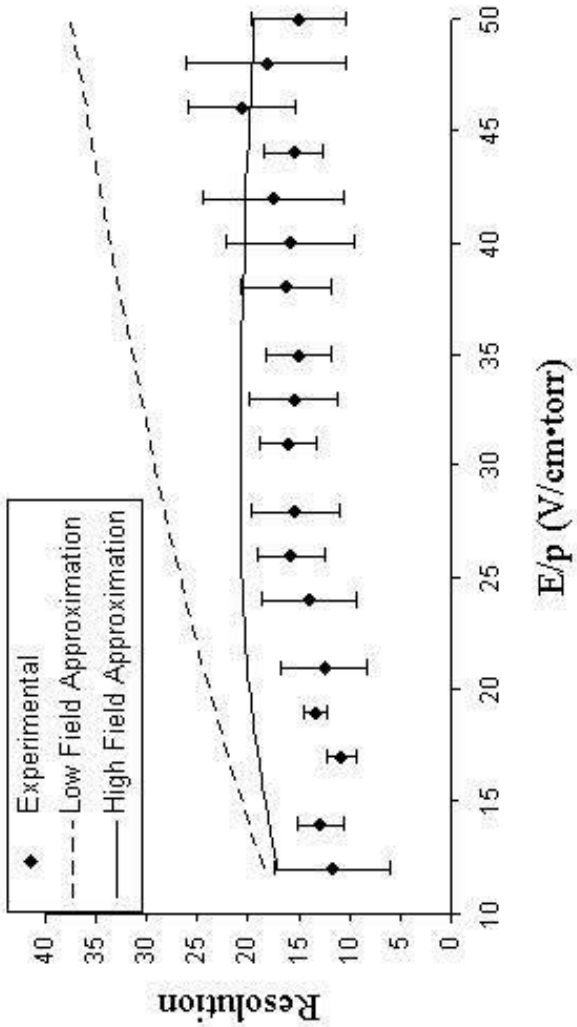

Figure 6. Plot of experimental C_{60} resolution at varying E/p compared to the low field and high field approximations.

Therefore, it can be seen that resolution can increase by applying higher fields for ions with K_o>1. The trend in figure 4B can be illustrated by showing the dependence of mass on peak resolution, since it has been well established that mass and mobility correlate. Figure 7 illustrates this mass dependence on resolution. The mobility resolution was measured for a group of peaks (I-V) at varying m/z. IM resolution ($t/\Delta t$) values for signals I, II, and III are 17.5, 30.3, and 33.0 respectively. Average IM resolution values for the ion signals in regions IV and V of the plot are 35.8 and 41.1 respectively.

Equation 19 also illustrates the dependence of resolution on temperature. Resolution can be substantially increased by decreasing the temperature of the drift gas. At a constant applied field, the resolution can increase 44% by reducing the temperature from 300K to 100K. Figure 8 contains a plot of resolution versus temperature for the Kr^{2+} ion in Kr drift gas. The actual resolution follows closely that predicted by equation 26.

While resolution ($t/\Delta t$) is an important figure of merit for IM cell design, resolving power, the ability of a technique to separate two species, is arguably a more important aspect of any separation. In the case of ion mobility, resolving power is directly proportional to resolution:[47]

$$R_s = R\left(\frac{t_2 - t_1}{t_{avg}}\right) \tag{27}$$

This indicates that increasing the peak resolution for a separation carried out under hard-sphere collision conditions (i.e. large molecule separation) will increase the resolving power. For small molecular ions which display a strong interaction with the buffer gas,

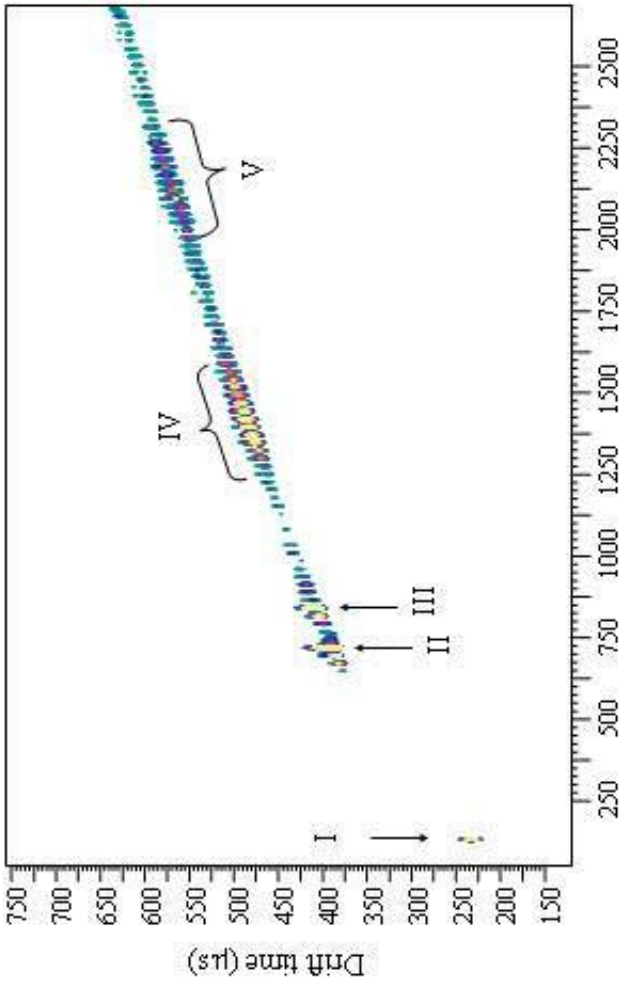

Figure 7. Drift time-m/z plot of a mixture Cs^+(Signal I), C_{60}^+(Signal II), C_{70}^+(Signal III), and other fullerene related carbon clusters (signals for C_{110}-C_{132} ions are labeled as IV, and signals for C_{144}-C_{184} ions are labeled as V) acquired at 66 V cm^{-1} $torr^{-1}$.

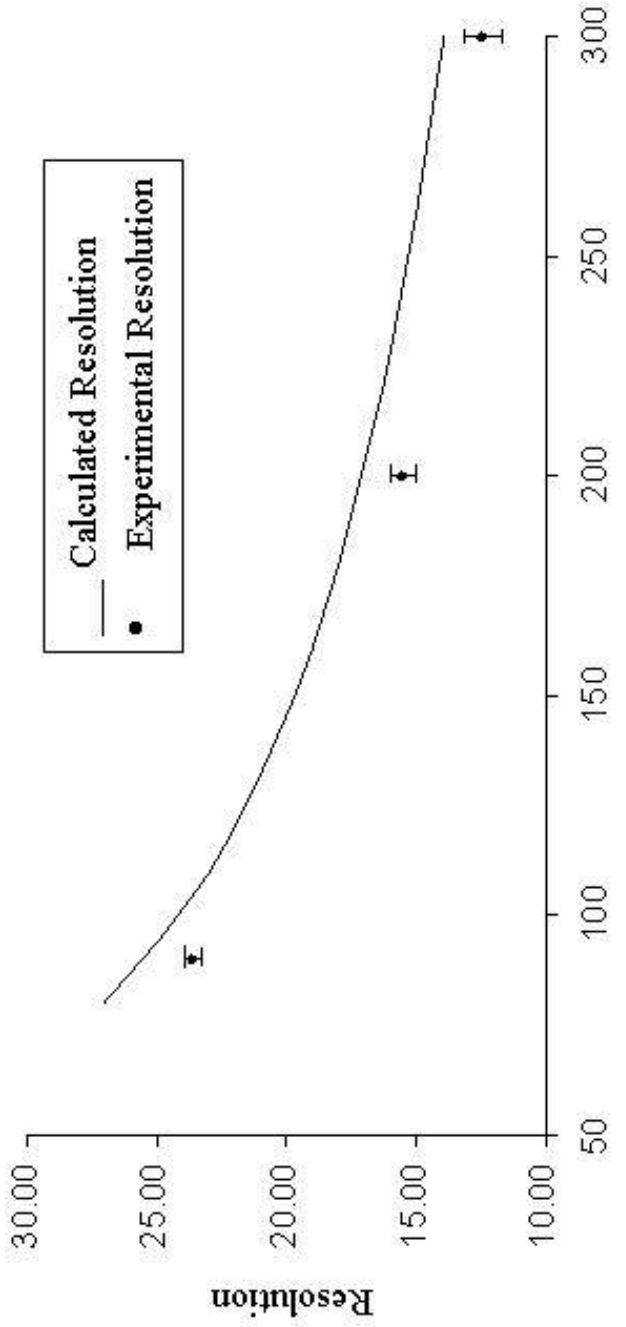

Figure 8. Plot of experimental Kr^{2+} resolution at varying temperature compared to the high field resolution approximations. Applied field is at 4W/cm•torr.

isobaric species can be separated. In these experiments resolving power is a better quantity to express. Figure 9 illustrates the resolving power increase for decreasing buffer gas temperature from 300 K (Figure 9A) to 90 K (Figure 9B). The resolving power is increased by a factor of 4.3 for the different excited and spin states of Kr^{2+} in Kr.

It is also known that the length of the drift region has a great impact on IM resolution. An observation that remains constant at high applied fields (See eq. 26). On the other hand, an increase in the drift region length will have adverse effects on the transmission efficiency of the drift cell, which will also affect the detection limits of the device (eq. 23). The transmission efficiencies of a low pressure instrument operating at high applied fields will suffer from increased ion loss due to the radial diffusion increase predicted by equation 22. Groups have solved some of the transmission problems by implementing methods to focus the radially diffusing ion packet back to the drift cell center. Examples are the implementation of a segmented radiofrequency-only quadrupole,[45] magnetic field,[46] and periodic focusing.[43]

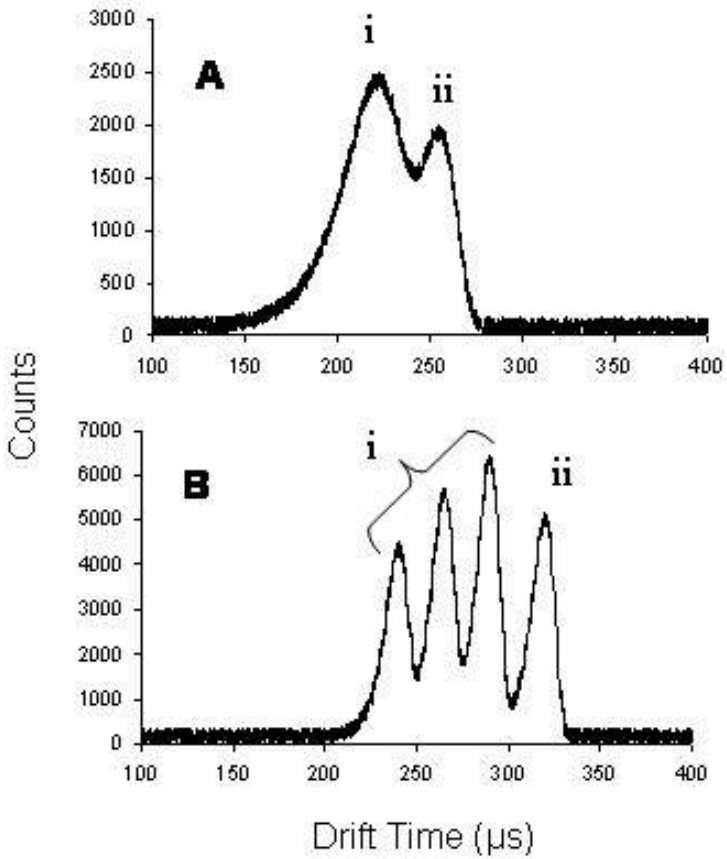

Figure 9. The arrival time distribution of Kr^{3+} in Kr at 0.5 torr, and an applied field at 8V/cm at 300K (**A**) and 90 K (**B**). Peaks i and ii are discussed in the text.

CHAPTER III

PERIODIC FOCUSING EQUATIONS FOR AN AXIALLY SYMMETRIC ELECTROSTATIC MOBILITY CELL

Background

The initial idea for the development of a periodic electrostatic lens came from Brookhaven National Laboratory's discovery of "strong focusing forces" using positive and negative successive sectors in a synchrotron.[48] The idea was further developed by Clogston and Heffner at Bell Labs in 1953 to aid in the problem of focusing long electron beams.[49] Here, they developed the mathematical treatment for axially symmetric periodic electric fields. The next evolution of this technique was to use a series of annular lenses with alternating positive, negative applied potentials to produce the periodic field.[50]

In 1964, Szilagyi of the Research Institute for Technical Physics of the Hungarian Academy of Sciences developed the mathematical treatment for a periodic electrostatic lens using a series of concentric rings interconnected by resistors designed by Dunn *et al.*[51-53] This application was adapted in microwave tubes to maintain the shape of long electron beams.[54] It was discovered here that the optimal electron flow was acquired when the period was greater than the aperture radius of the rings.[51]

Periodic focusing has been developed over the years specifically for the application of confining high energy beams. Segmented quadrupoles have also been employed to produce the focusing, defocusing repetitive pattern for positron and electron

confinement.[55] This had a profound impact in applications due to the fact that periodic focusing eliminated the need for magnetic confinement.[55]

The reason the periodic field maintains the electron or ion beam is due to repetitive focusing, defocusing regions. In this system, the charged particle is always further away from the axis in a focusing region, while closer to the axis in the defocusing region.[56] This allows focusing of the electron or ion beam due to the fact that the charged particle is deflected in the defocusing region, then the focusing region overcompensates by reflecting the ion back to the center. A net focusing effect is observed in the absence of diffusion.

Here, we present the mathematical equations and simulations of a periodic electrostatic lens applied to ions in a neutral buffer gas. We show the effect of ion mass and applied fields on the ion transmission properties as compared to a linear electrostatic lens. Our results incorporate Wannier's diffusion in both the periodic and linear cases.

Mathematic Derivation

Figure 10 shows a waveform and its properties. Here the sinusoidal plot illustrates an applied field (E_o) on a periodic electrostatic lens.

$$E(z) = E_o + A\sin\left(\frac{2\pi}{L}z_o + \frac{2\pi}{L}z\right) \tag{28}$$

Equation 1 defines the field along the z-axis at r=0 (the radial component). Here, A is the amplitude, z_o is the waveform's starting point offset, and L is the length between electrostatic lenses (Figure 10). To simulate the motion of an ion within this applied

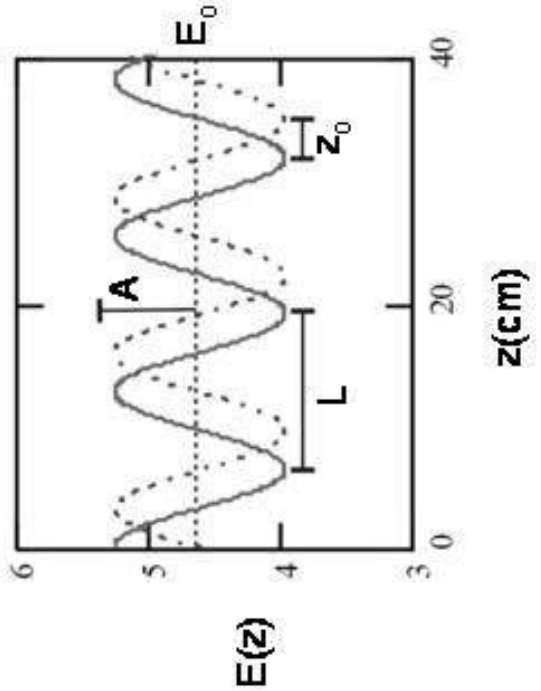

Figure 10. Schematic of a periodic field (dashed with no offset, lined with offset z_0).

field, the radial component (r) must be added. The definition of the potential (V(r,z)) for a cylindrically symmetric lens system is determined by power series expansion (eq. 29) based on the potential in the z-direction (V(z))[57].

$$V(r,z) = V(z) - \frac{r^2 V(z)^{II}}{2^2} + \frac{r^4 V(z)^{IV}}{2^2 \cdot 4^2} ..... \tag{29}$$

From Equations 1 and 2, the field (E(r,z)) must be determined at any radial and translational position to determine the acceleration (a) imposed on the ion.

$$a(r,z) = \frac{E(r,z)e}{m} \tag{30}$$

Here, e is the ion's charge and m is the ion's mass.

In order to solve equation 29, V(z) must be determined by integrating E(z) over all space:

$$V(z) = \int E(z)dz \tag{31}$$

$$V(z) = E_o z - \frac{AL}{2\pi}\cos\left(\frac{2\pi}{L}z_o + \frac{2\pi}{L}z\right) + C \tag{32}$$

where C is a constant of integration. The second and fourth derivative must be determined to complete the expansion of equation 29.

$$V(z)^I = E_o + A\sin\left(\frac{2\pi}{L}z_o + \frac{2\pi}{L}z\right) \tag{33}$$

$$V(z)^{II} = \frac{2A\pi}{L}\cos\left(\frac{2\pi}{L}z_o + \frac{2\pi}{L}z\right) \tag{34}$$

$$V(z)^{III} = -\frac{4A\pi}{L^2}\sin\left(\frac{2\pi}{L}z_o + \frac{2\pi}{L}z\right) \tag{35}$$

$$V(z)^{IV} = -\frac{8A\pi}{L^3}\cos\left(\frac{2\pi}{L}z_o + \frac{2\pi}{L}z\right) \tag{36}$$

By substituting equations 32, 34, and 36 into equation 29, a complete potential equation is obtained.

$$V(r,z) = E_o z - \frac{AL}{2\pi}\cos\left(\frac{2\pi}{L}z_o + \frac{2\pi}{L}z\right) - \frac{r^2 A\pi}{2L}\cos\left(\frac{2\pi}{L}z_o + \frac{2\pi}{L}z\right)$$

$$-\frac{r^4 A\pi^3}{8L^3}\cos\left(\frac{2\pi}{L}z_o + \frac{2\pi}{L}z\right) + C \tag{37}$$

Equation 10 gives the complete potential for any z and r within a cylindrically symmetric periodic electrostatic lens. Figure 11 illustrates the 3-D graphical representation of the potential within the periodic electrostatic lens.

In order to determine ion motion, the field must be determined along the radial and translational axis. This is accomplished by taking the derivative of equation 37 in terms a z at constant r for the translational component, and in terms of r at constant z for the radical component.

$$E(z) = E_o + A\sin\left(\frac{2\pi}{L}z_o + \frac{2\pi}{L}z\right) + \frac{r^2 A\pi^2}{L^2}\cos\left(\frac{2\pi}{L}z_o + \frac{2\pi}{L}z\right)$$

$$+\frac{r^4 A\pi^4}{4L^4}\sin\left(\frac{2\pi}{L}z_o + \frac{2\pi}{L}z\right) \tag{38}$$

$$E(r) = -\frac{rA\pi}{L}\cos\left(\frac{2\pi}{L}z_o + \frac{2\pi}{L}z\right) - \frac{r^3 A\pi^3}{2L^3}\cos\left(\frac{2\pi}{L}z_o + \frac{2\pi}{L}z\right) \tag{39}$$

The radial and translational field can be determined for any (r,z) position.

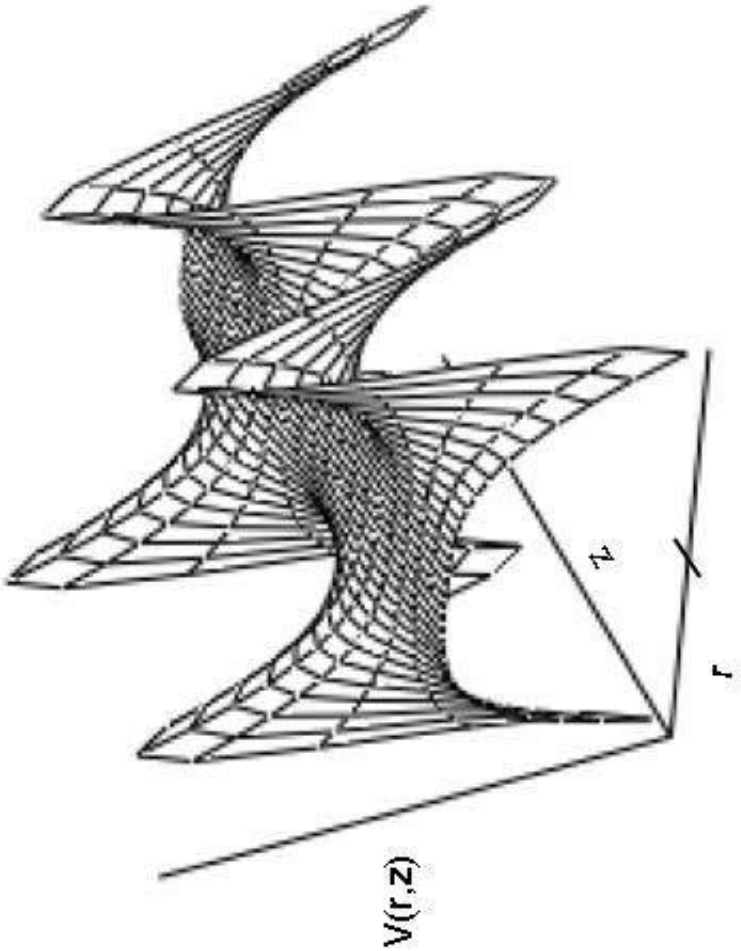

Figure 11. 3-D contour plot of the potential versus radial position(r) and axial position (z)

Results and Discussion

Figure 12 shows the potential (V) behavior as a function of z (the translational axis). As an ion is found further from the center (r=2, 2.5) the potential becomes increasingly periodic (equation 37). Figure 12 shows the 3-D representation of the potential value from equation 37 as a function of both r (radial component) and z. Figure 12 illustrates the focusing, defocusing, etc. nature of the periodic lens assembly.

To prove the focusing effect of a periodic field, it was necessary to run an ion motion simulation in the absence of a neutral drift gas. The ion motion has been shown to have a net focusing effect in the presence of a periodic field for high intensity electron beams.[9] Figure 13 shows the simulated behavior of the ions in a periodic electrostatic lens array using equations 38 and 39, and negating the space-charge effects. An ion in a periodic electrostatic field demonstrates similar focusing effects compared to a periodic field produced from alternating quadrupole fields.

The program developed herein (Appendix B) was designed to simulate an ion's motion in a periodic field in the presence of a neutral buffer gas. Figure 14 shows the front end of the simulation program developed in Visual Basic.Net. Tools are added to vary the diffusion (pressure, temperature), define the ion (mass, mobility, cross-section), and calculate transmission (exit radius). The diffusive pattern figure on the left illustrates the ion diffusion due to Wannier's radial diffusion equation in a linear field. This can be compared to the diffusion pattern of the ions in a periodic field with the same diffusion equations (right figure). Diffusive steps are taking in the radial direction for the periodic simulation based on the diffusion values calculated on Wannier's

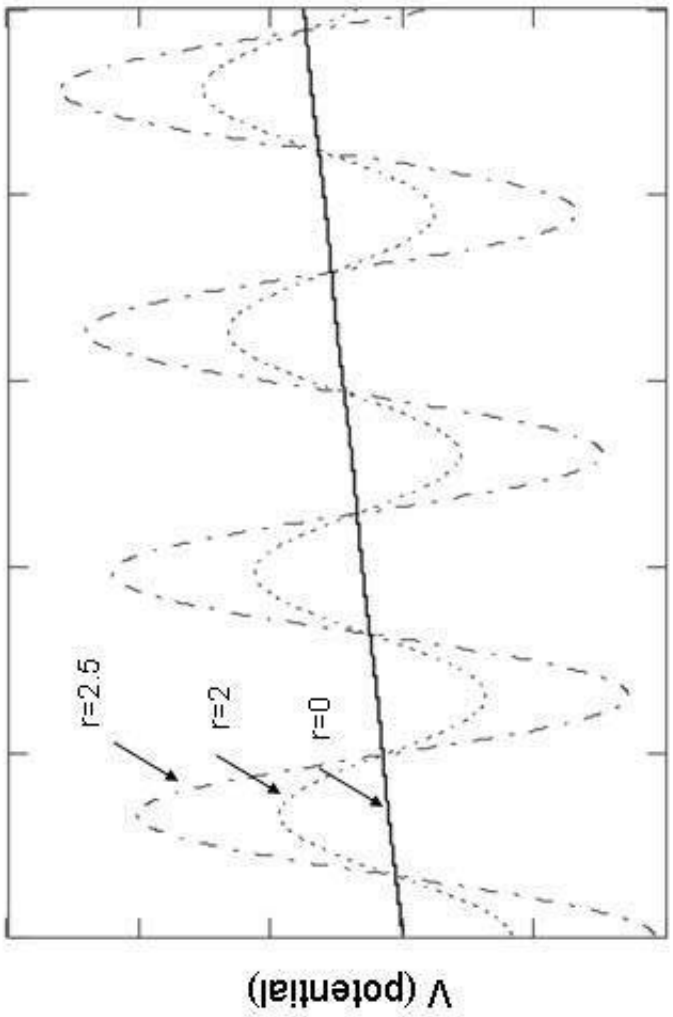

Figure 12. Plot of position along the z axis versus potential for differing radial positions.

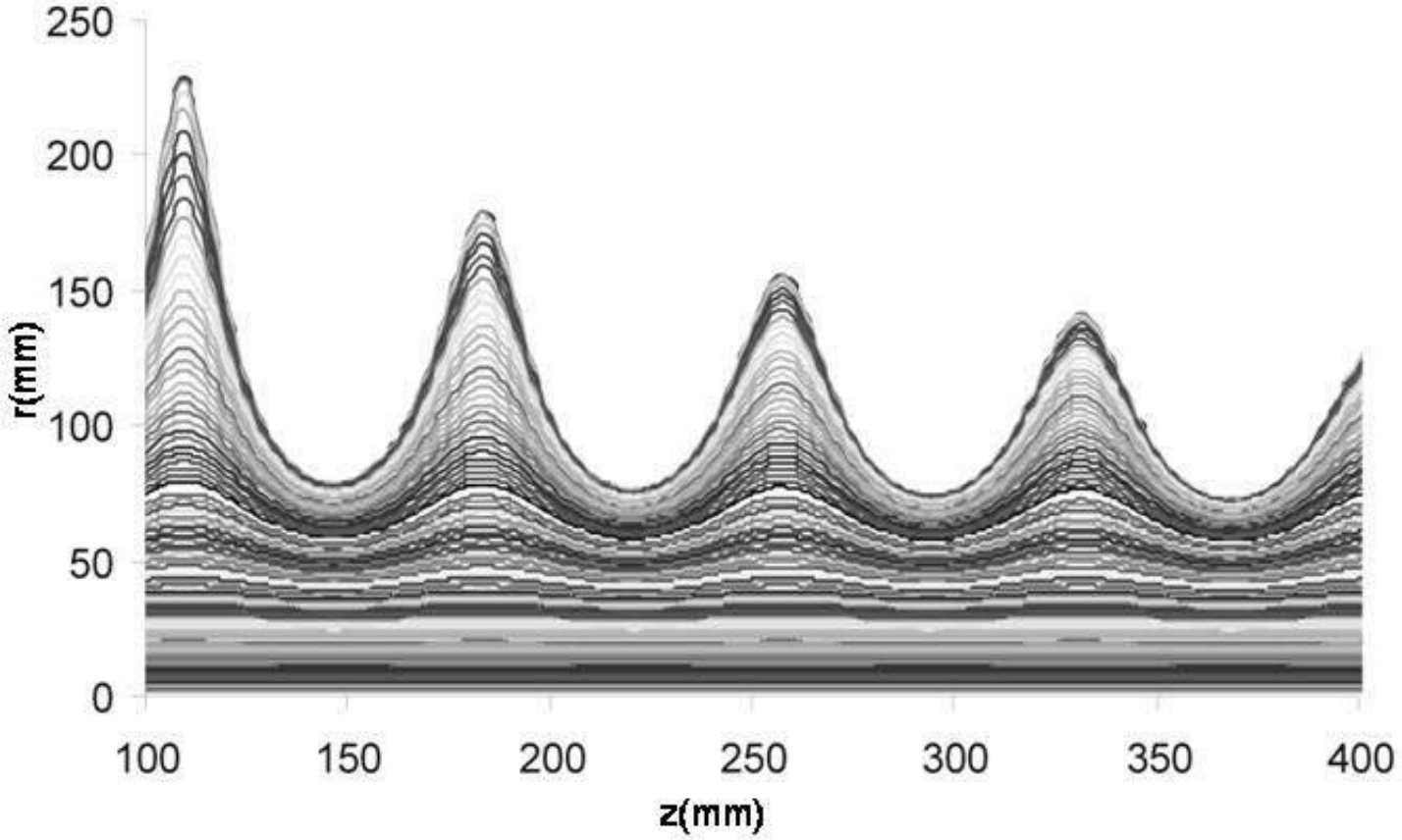

Figure 13. Schematic of the periodic simulation program's front end.

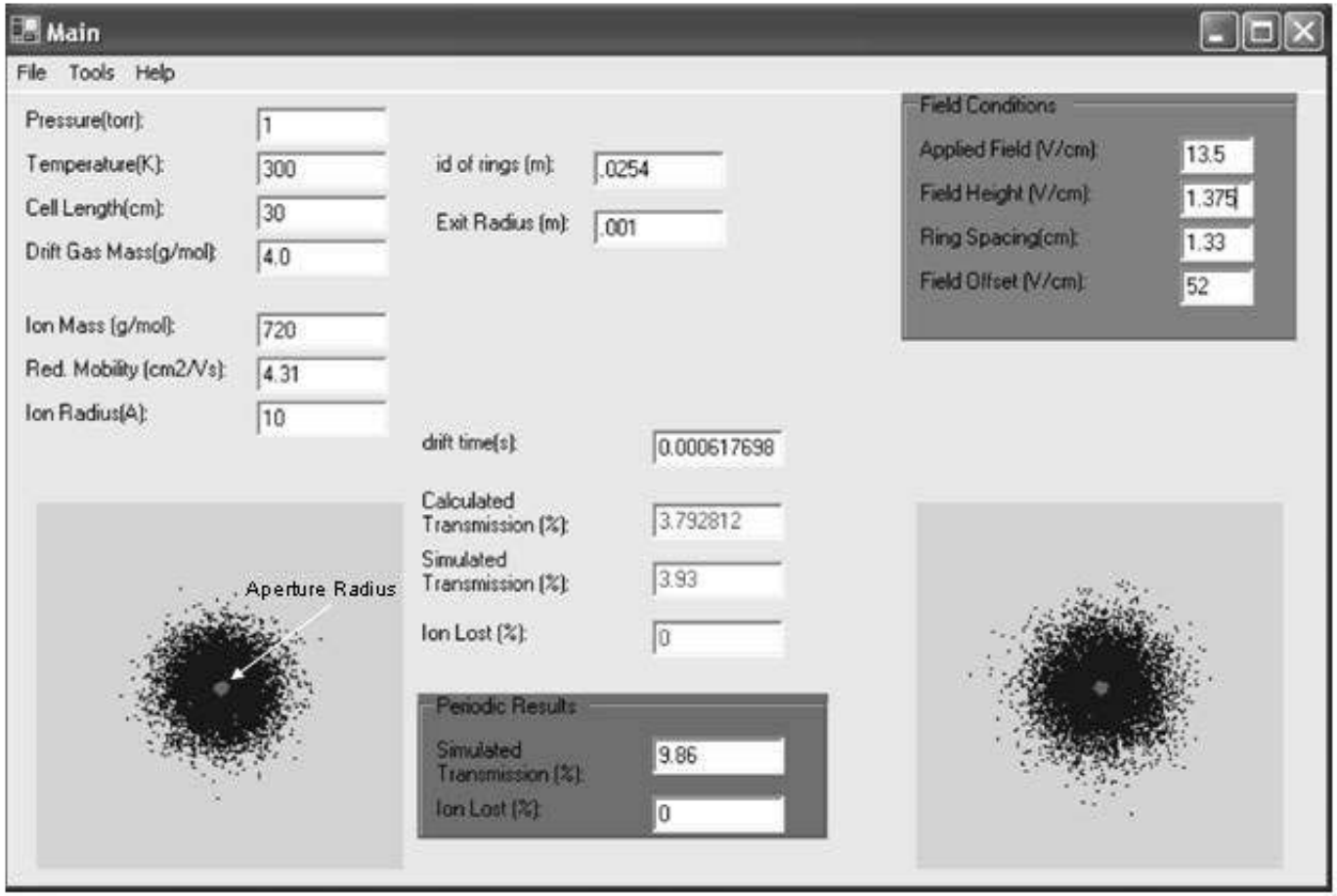

Figure 14. Schematic of the ion radial motion along the z-axis within a periodic electrostatic lens for ions starting from 0 to 100 mm from the radial axis (r=0).

equations in a linear field. The field effects are then determined for the ion location (r,z) and a new position based on these values are determined. These steps are determined by the z value of ¼ the mean free path of the ion. The percent transmission is then determined by the number of ions within the r value of the exit radius (the light colored spot). The program will also output the radial position to an ascii text file to look at the full dispersion of the ions under specific conditions.

Figure 15 shows the ion count distribution for 10000 ions as a function of distance from r=0. Figure 15A shows the distribution for ions of m/z = 720 in a 30cm linear field for an applied field of 13.5V/cm. Figure 15B shows the same ions after a periodic electrostatic lens system of the same length. The number of ions confined towards the center of the cell (r=0) has increased a factor of 35 for m/z=720 for an exit aperture radius of 0.1mm.

Figure 16 and 17 shows the trends of the factor increase in transmission versus cell length and aperture diameter, respectively, for a series of masses in a periodic cell compared to a linear cell. Higher mass ions get better transmission, but since the diffusion is decreased due to an increase in mass (shorter mean free path), the increase in transmission over a linear cell will be less pronounced. These trends also illustrate a better increase in transmission at smaller aperture values.

Figure 18 illustrates the increase in transmission of the periodic cell compared to the linear cell for differing applied electric fields. As can be seen, for a specific cell geometry (ring spacing), a specific field is best applied. The reason why better confinement cannot be attained by increasing the applied field (negating space-charge

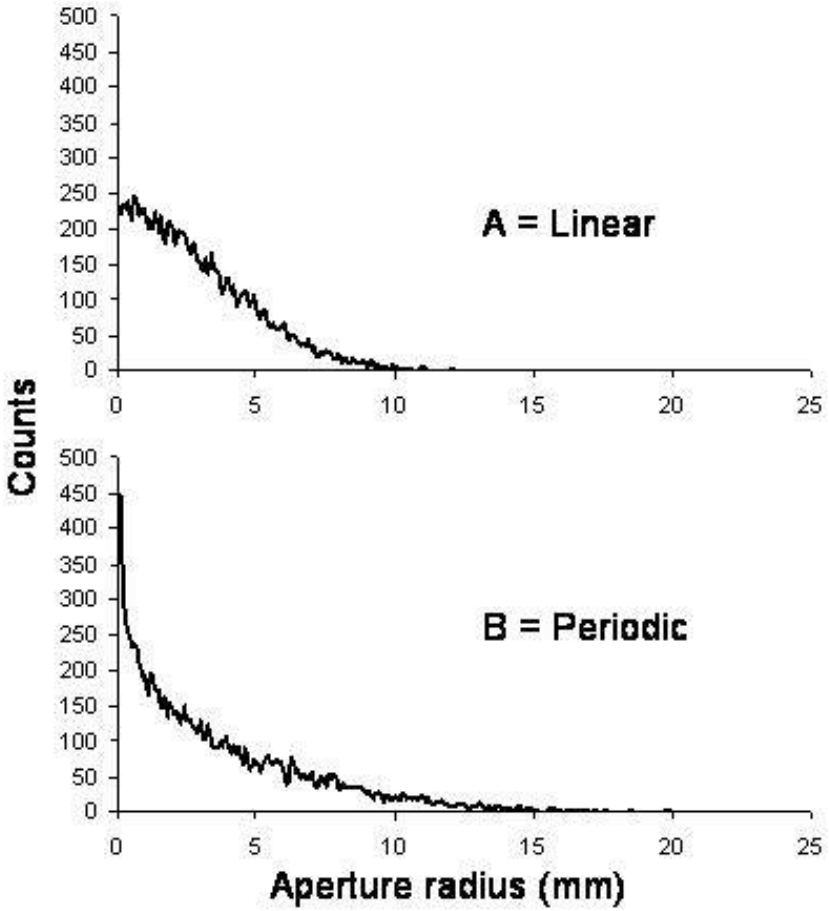

Figure 15. Simulated ion distribution as a function radial position for a linear field at 13V/cm (A) and a periodic field at 13V/cm with a period of 1.3cm (B) for m/z 720.

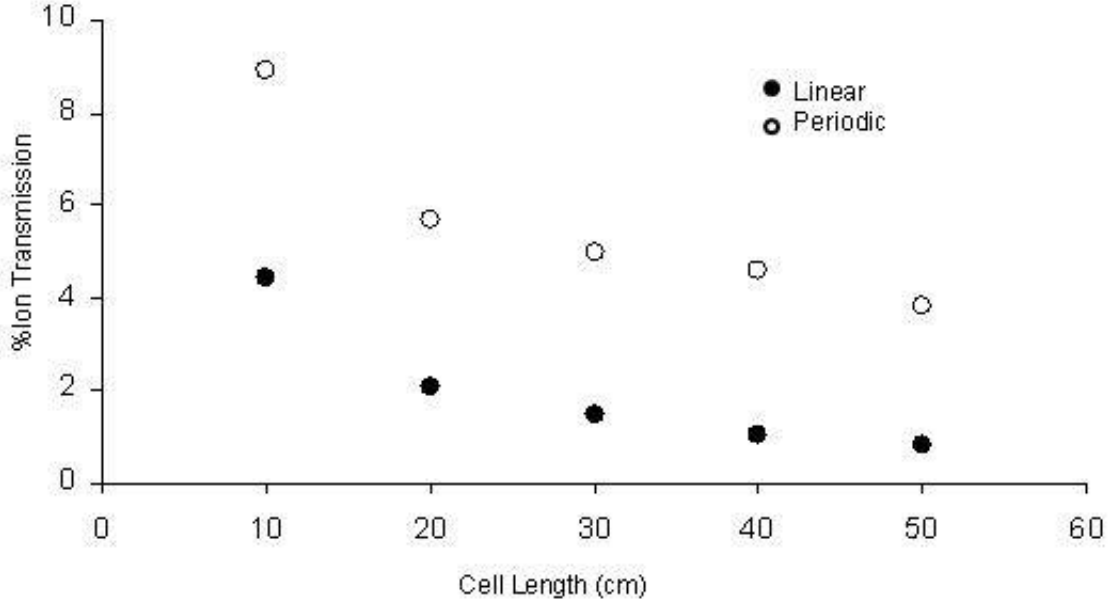

Figure 16. Plot of percent ion transmission versus cell length comparing the results of the linear and periodic fields.

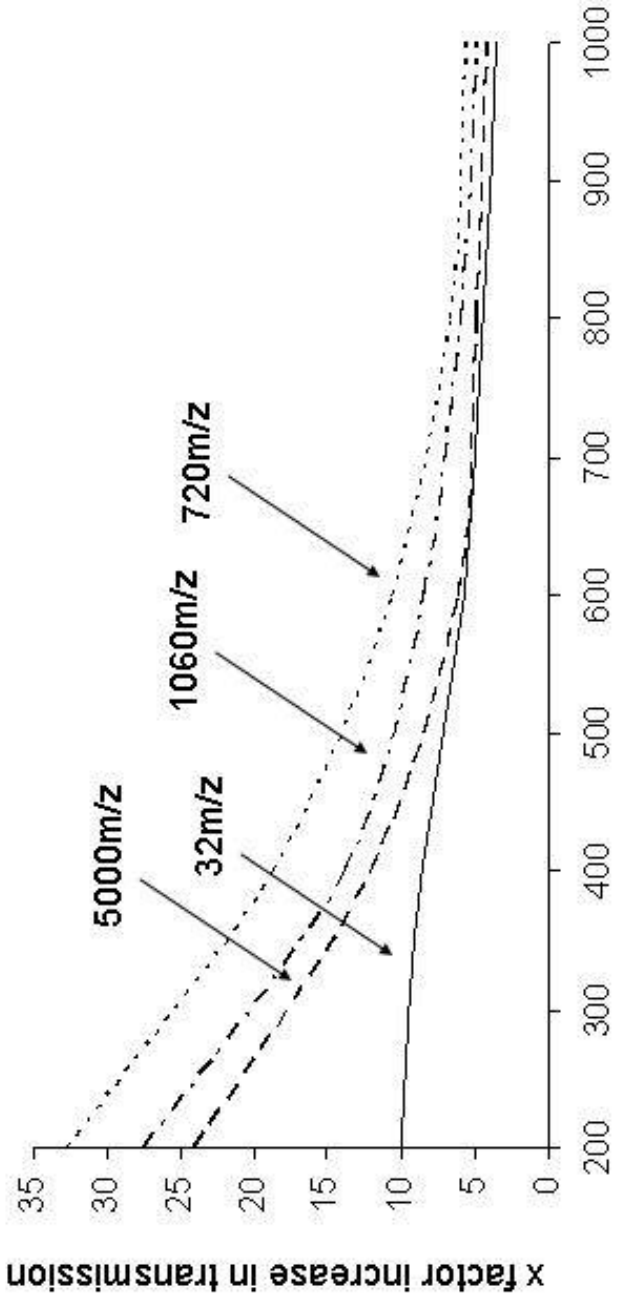

Figure 17. Factor increase of transmission for the periodic field (13.5W/cm) compared to the linear field (13.5W/cm) as a function of aperture diameter for m/z = 32, 720, 1060, and 5000.

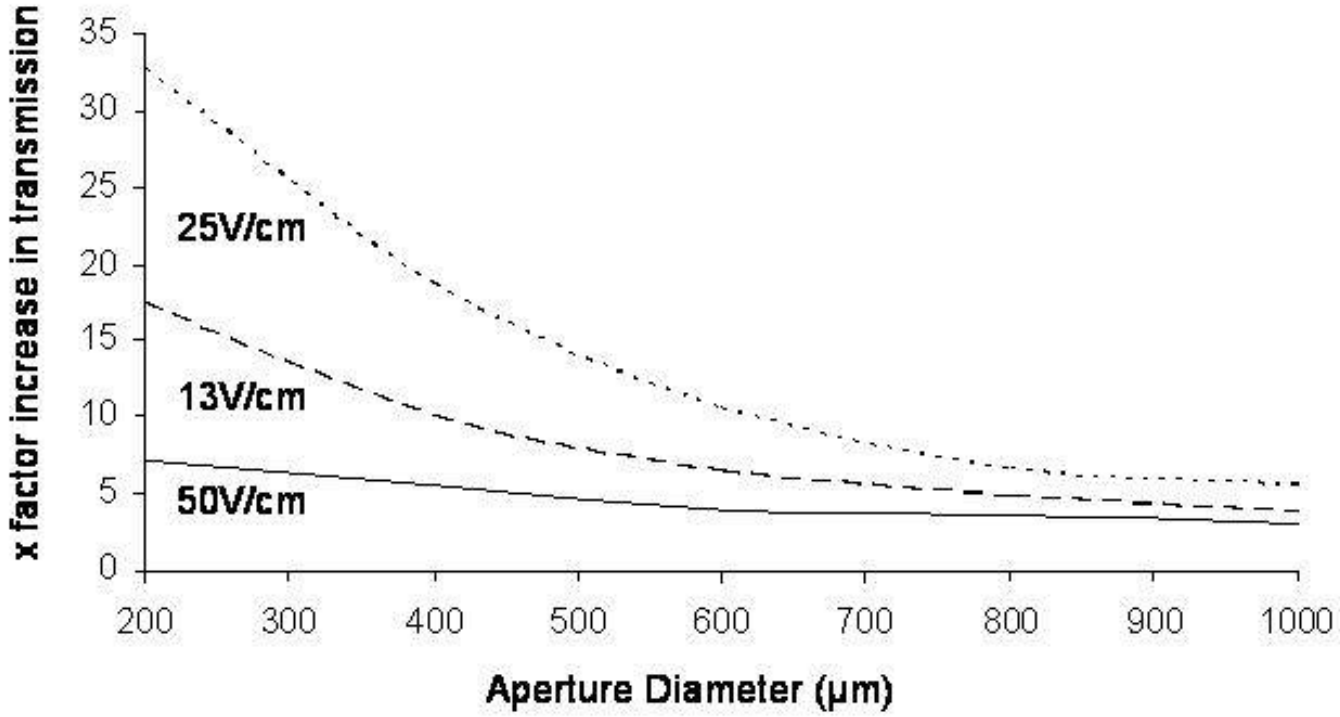

Figure 18. Factor increase of transmission for the periodic field compared to the linear field as a function of aperture diameter for differing applied fields for m/z 720.

effects), is that diffusion increases as a square of the applied field. So, increasing the applied field will increase radial ion confinement, but eventually will be negated by a large ion diffusion value.

CHAPTER IV

DEVELOPMENT OF A MONTE CARLO METHOD FOR DETERMINING COLLISION CROSS-SECTIONS: MOBCROSS

Background

Since the inception of ion mobility, many programs have been developed to predict an ion's motion through a neutral buffer gas[19,58-63]. Since the dawn of using mobility to separate large clusters and biomolecules, one of the most popular computational prediction tools is the Monte Carlo integration technique to determine the orientationally-averaged collision cross section by random rotations of the molecule and calculation of the projection area[64]. For molecules of large molecular weight (>300D) this method has been shown to accurately predict (<3.0% error) collision cross sections compared to experimentally determined values.[65]

Current methods employ Eulerian angles (θ,φ,ψ) which are randomized between 0 and 2π to rotate a rigid nonlinear molecule.[64] This leads to slow programs due to the fact that each angle of rotation must be solved using trigonometric functions, which are computationally expensive. An alternative to this method of orientational moves is to use quaternion parameters.[66-67] The rotational operation adds one more variable, however all equations are solved algebraically.

$$Q = \{q_0, q_1, q_2, q_3\} \tag{40}$$

The quaternion is a unit vector in four-dimensional space,

$$q_0^2 + q_1^2 + q_2^2 + q_3^2 = 1 \tag{41}$$

corresponding to Euler angles.

$$q_0 = \cos\left(\frac{\theta}{2}\right)\cos\left(\frac{\phi+\psi}{2}\right) \tag{42}$$

$$q_1 = \sin\left(\frac{\theta}{2}\right)\cos\left(\frac{\phi-\psi}{2}\right) \tag{43}$$

$$q_2 = \sin\left(\frac{\theta}{2}\right)\sin\left(\frac{\phi-\psi}{2}\right) \tag{44}$$

$$q_3 = \cos\left(\frac{\theta}{2}\right)\sin\left(\frac{\phi+\psi}{2}\right) \tag{45}$$

The matrix (R) is then applied to the rotation of the rigid nonlinear molecule.

$$R = \begin{pmatrix} q_0^2+q_1^2-q_2^2-q_3^2 & 2(q_1q_2-q_0q_3) & 2(q_1q_3+q_0q_2) \\ 2(q_1q_2+q_0q_3) & q_0^2-q_1^2+q_2^2-q_3^2 & 2(q_2q_3-q_0q_1) \\ 2(q_1q_3-q_0q_2) & 2(q_2q_3+q_0q_1) & q_0^2-q_1^2-q_2^2+q_3^2 \end{pmatrix} \tag{46}$$

For each rotation, Vesely has shown a five fold improvement for generating the random variables (q) and applying the rotation matrix for the quaternion Monte Carlo integration over the currently used Eurlerian method.

Experimental

The MobCross projection cross-section program was developed using Microsoft® Visual Studio.Net version 2002. Appendix A shows the details of the program. MobCross inputs two formats; the Gaussian 98® coordinate from a .log output file, and the Cartesian coordinate file from Cerius®. All output is saved in an ASCII text file.

The calculation of the projection cross-section of a species is performed in three steps. First, the coordinate is read in and converted into a center-of-mass coordinate system. All rotations of the molecule are performed about the center of mass point.

Second, a circle is drawn around the molecule with a radius (r) equal to the greatest distance from the center-of-mass. Lastly, the random iterations are performed by rotating the molecule (2000x) about its center-of-mass, within the known circle area. After each rotation, random buffer gas species (5000) are placed within the known area, and determined as a hit (1) or miss (0) of the molecular ion of interest. Total number of hits (n_h) is divided by total number placed (n_t) and multiplied by the known area of the encompassing circle (πr^2). This is performed after each rotation (n_r), than the cross-sectional area (σ) is determined by averaging over all projections.

$$\sigma = \frac{\sum_{1}^{n_r} \frac{n_h(\pi r^2)}{n_t}}{n_r} \tag{47}$$

The amino acid ion ($M+H^+$) structures were determined with a geometry optimization using B3LYP density functional theory (DFT) with the 6-31G basis set. Peptide ion ($M+H^+$) molecular dynamics calculations were performed with the Cerius (Accelrys) suite of programs using the consistent force field (CFF1.01). Model structures for the peptide ions were generated using a simulated annealing cycle where the peptide ion is heated to 1000 Kelvin and held at that temperature for 10 picoseconds and then ramped down to room temperature. The ion structure is minimized following each heating cycle. Three hundred structures were generated for each peptide. Semi-empirical calculations using AM1 parameters were used to determine the energy of each structure. Both amino acids and peptides were compared with published experimental data.

Results and Discussion

Due to the use of the quaternion algorithm to rotate the molecule, it is now possible to run the cross-section simulations on a conventional PC of molecules with mass less than 10000D in under 5 minute computational time (2000 rotations with Monte Carlo integration). This would translate to 10 times longer using Eulerian angles. The projection cross-section algorithm was first tested on 19 amino acids ions, $M+H^+$, with the proton located at the N-terminal site. Figure 19 plots the trend of the calculated and experimental mobility values. Table I shows the calculated mobility versus the experimental,[68] and the percent error of the calculated value. The data shows only 3 outliers (greater than 3.0% error) from the experimental values; glycine, lysine, and arginine. Of these three, lysine and arginine share a second site for protonation, and therefore another possible projection area. Both of these basic residues were recalculated with the protonation site on the side chain and showed a change in cross-sectional area. Lysine's theoretical mobility changed by 3% to a value of 1.413 cm^2/Vs, resulting in an experimental error of only 2.8% from the reported experimental value. Arginine also produced a better theoretical mobility value of 1.372 cm^2/Vs. This reduced the error to 1.5% from the reported experimental value. No new structures could be found for glycine to explain the large deviation in experimental and theoretical results. Because of the small size of glycine, interaction potentials could be involved, making the cross section appear larger then it actually is; however, because the mobility of alanine is 1.798 it seems unlikely that glycine has a smaller mobility (1.781) experimentally.

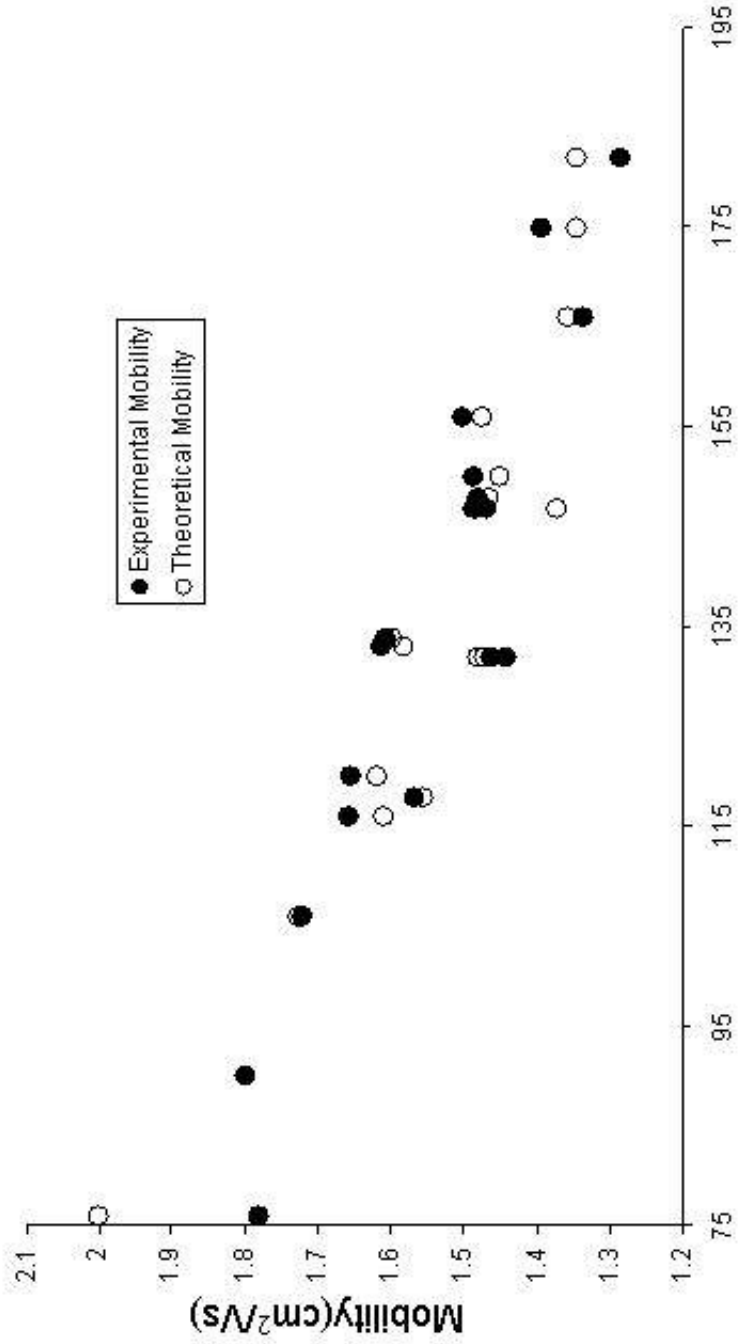

Figure 19. Experimental and theoretical plots of mobility versus mass for 19 amino acids.

Table I. Experimental and theoretical mobility (cm^2/Vs) values for 19 amino acids.

Amino Acid	Mass	Experimental Mobility	Calculated Mobility	Percent Difference
Gly	76	1.781	2.001	12.36
Ala	90	1.798	1.799	0.03
Ser	106	1.72	1.728	0.47
Pro	116	1.659	1.609	3.01
Val	118	1.566	1.556	0.67
Thr	120	1.656	1.618	2.27
Ile	132	1.463	1.479	1.06
Leu	132	1.441	1.469	1.98
Asn	133	1.613	1.582	1.92
Asp	134	1.606	1.598	0.51
Gln	147	1.483	1.486	0.18
Lys	147	1.469	1.373	6.55
Glu	148	1.48	1.464	1.06
Met	150	1.486	1.460	2.43
His	156	1.501	1.474	1.81
Phe	166	1.334	1.357	1.75
Arg	175	1.393	1.346	3.38
Tyr	182	1.284	1.299	1.17

MobCross was next integrated into a recipe for determining the most probable structure for a series of peptides ranging from 7 to 10 amino acid residues. Because molecular mechanics calculations using simulated annealing can produce a broad range of structures, the projection cross-section calculation was utilized on 300 low energy structures for each peptide and plotted in a distribution curve. Figure 20 shows the extent of the cross-sectional values for each of the peptides analyzed compared to the experimental value.[69] Errors as great as 40% difference from the reported experimental value can be attained with improper selection of a final annealing result.

Figure 21 shows a distribution of one of the calculated peptides, ADFTEISK. As can be seen, there exist a single cross-sectional distribution for each of the low energy molecular mechanics results. From the distribution, the peak max (most populated cross-section) is chosen as the most probable structure and compared to the experimental result. Table II shows the experimental and theoretical results of the peptides of interest with the calculated error of the recipe used. The method of using the molecular mechanics with simulated annealing in combination projection cross-section algorithm produced 80% within the 3% limit and 96% within 5%. Figure 22 shows the plot of the calculated cross-section using the before mentioned recipe compared to the excepted experimental results.

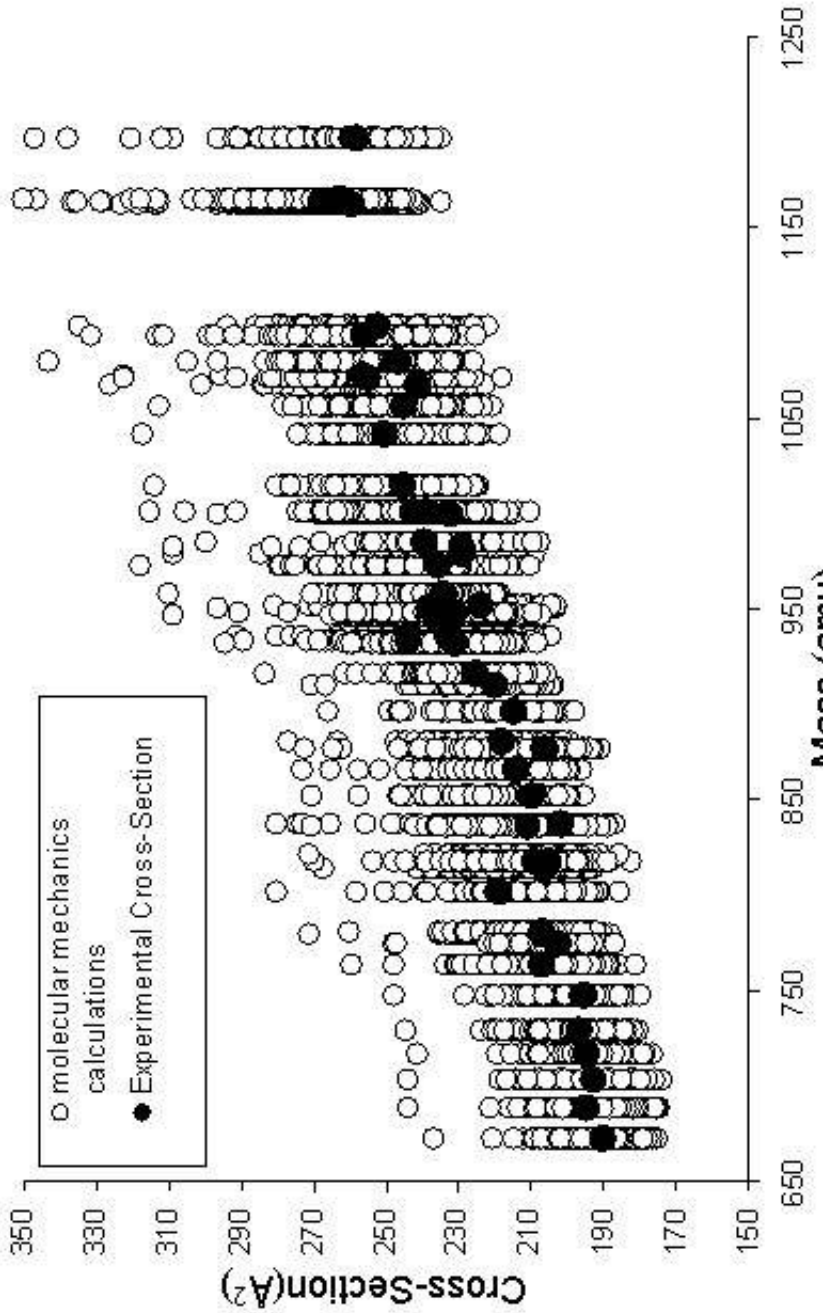

Figure 20. Distribution of theoretical values compared to the experimental cross-section for representative masses.

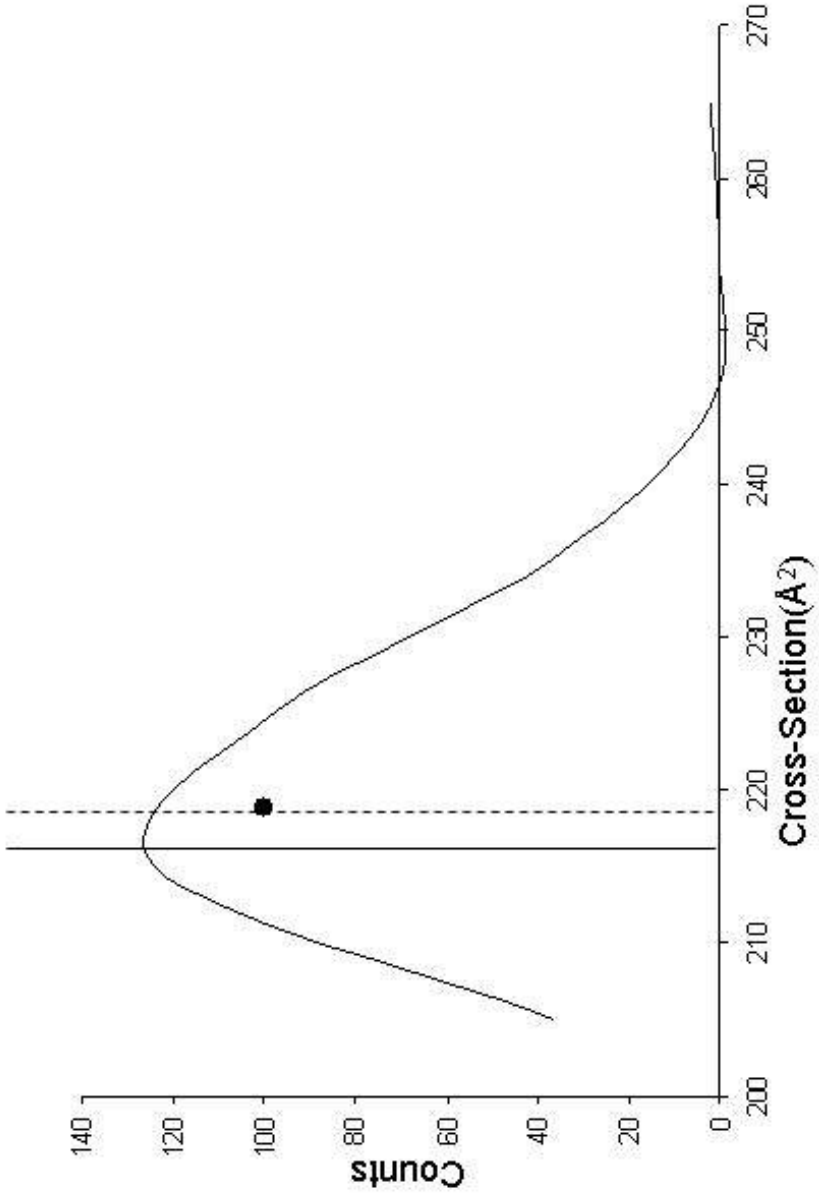

Figure 21. Cross-sectional distribution for theoretical results of the ADFTEISK peptide compared to the single experimental value.

Table II. Comparison of theoretical and experimental cross-sections and the percent difference.

Peptide	Mass	Exp. Cross Section	Theo. Cross	%Error	Peptide	Mass	Exp. Cross Section	Theo. Cross Section	%Error
vaaaltk	673.83	190.32	189.32	0.53	aavtgfwgk	937.09	233.00	228.08	2.11
vltsaak	689.83	194.37	191.92	1.26	slvsglwgk	947.12	236.29	238.11	0.77
vlsaadk	703.81	193.03	195.13	1.09	vltpdlyk	949.13	230.73	226.20	1.96
vadaltk	717.84	194.69	191.90	1.43	aavtafwgk	951.11	237.76	231.82	2.50
vlspadk	729.85	196.51	195.81	0.36	dlgeenfk	952.01	223.98	219.66	1.93
vsealtk	747.87	195.59	195.81	0.11	qsalaelvk	959.13	234.39	241.26	2.93
vlaavyk	763.96	206.94	204.73	1.07	eavlglwgk	973.16	235.37	244.83	4.02
vvtdltk	775.92	202.35	196.87	2.71	dgagdvafvk	979.08	229.25	239.66	4.54
mifagik	780.02	207.13	214.36	3.49	eyeatlek	983.06	229.28	235.42	2.68
vlpvpqk	780.99	206.94	202.51	2.14	tyettlek	985.08	239.55	230.64	3.72
alqasak	801.96	218.92	219.76	0.38	dlgeqyfk	1000.10	232.22	232.61	0.17
divgavlk	815.00	206.07	211.42	2.59	vlgeeyvk	1001.12	238.79	235.41	1.41
gasivedk	818.90	205.22	211.05	2.84	qtalvelvk	1001.21	242.43	238.54	1.61
vdpvmfk	818.95	208.72	198.60	4.85	qtalvellk	1015.24	245.01	240.45	1.86
mltaeek	821.97	209.77	213.72	1.88	mflgfpttk	1042.29	250.02	246.42	1.44
npdpwak	827.91	198.09	198.65	0.28	tfqsfpttk	1057.19	245.22	241.37	1.57
igdyagik	836.96	210.60	217.37	3.22	aqsdfgvdtk	1068.13	241.43	250.24	3.65
fgvngsek	837.91	201.76	217.64	7.87	mflsfpttk	1072.31	255.16	251.77	1.33
dsadgflk	852.92	209.30	210.94	0.78	fqplvdepk	1073.23	255.89	252.09	1.49
adfaevsk	866.95	214.17	215.00	0.39	taaywnaiek	1080.23	246.52	258.32	4.79
wnmqnqk	878.00	206.26	214.33	3.91	vlqsfsdglk	1094.25	255.95	252.69	1.27
adfaeisk	880.97	218.06	218.22	0.07	vldsfsngmk	1098.27	252.25	254.95	1.07
adftdvtk	896.97	214.56	208.12	3.00	fmmfesqnk	1162.38	259.37	253.85	2.13
adfteisk	911.00	219.61	215.34	1.95	lvneltefak	1164.34	267.51	267.92	0.15
idalnenk	917.01	225.09	222.95	0.95	lvnevtefak	1165.33	262.66	261.13	0.58
savtalwgk	933.09	231.09	230.51	0.25	seeeypdlsk	1197.24	257.78	266.99	3.18
livtqtmk	934.19	243.91	225.52	7.54					

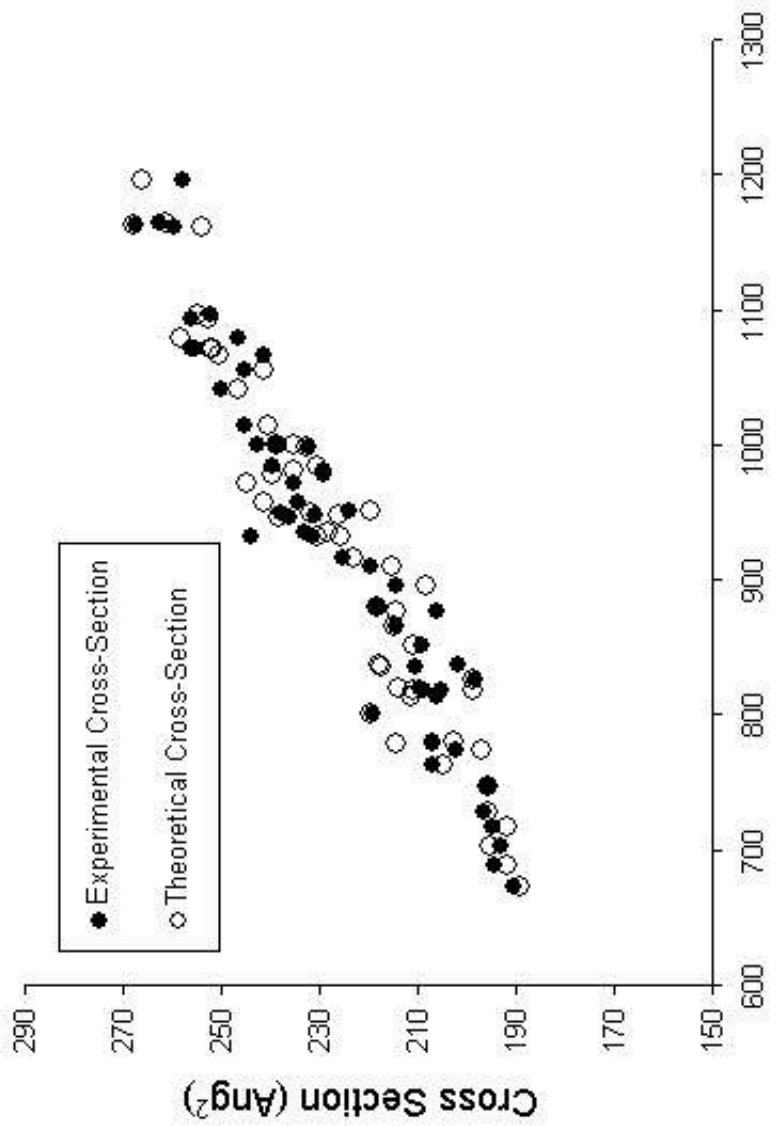

Figure 22. Plot of representative peptides cross-section versus mass for both experimental and theoretical calculations. Single theoretical value based on apex of distributional values.

CHAPTER V

DEVELOPMENT OF A VARIABLE-TEMPERATURE ION MOBILITY TIME-OF-FLIGHT MASS SPECTROMETER

Background

Over the past four decades, the understanding of gas phase ion chemistry has had tremendous growth.[70-71] Since the late 1960's, the drift tube has grown to be a useful technique in understanding ion-molecule collision phenomena and gas phase ion chemistry.[1,72] Almost since its inception, drift tube experiments have had the ability to control the buffer gas temperature.[73] Being able to control the temperature to study collision phenomena and probe reaction chemistry is vital and well understood today.

From chapter II, we have already seen the importance temperature plays on peak resolution. Temperature also plays a dominate role in the interaction between the buffer gas and the ion by lowering the centrifugal barrier, and allowing more efficient capture events.[74-76] Equation 7 includes the relative orbital angular momentum, L, for the potential surface.

$$L = \left(\frac{8kT\mu b^2}{\pi} \right)^{\frac{1}{2}} \tag{48}$$

Where k is the Boltzman constant, T is the gas temperature, μ is the reduced mass, and b is the impact parameter. Both the increase in ion-neutral interaction and the increase in resolution make a liquid nitrogen-cooled drift cell desirable for separation of small electronic isomers.

Experimental

The experiments were performed using a home-built liquid nitrogen-cooled ion mobility orthogonal time-of-flight mass spectrometer (Figure 23). The instrument consists of an electron impact source (EI), drift cell, channeltron detector collinear with the drift tube, orthogonal flight tube, and a microchannel plate (MCP) assembly for detection with orthogonal extraction. The assembly is housed within a stainless steel high vacuum cavity with 2 diffusion pumps, and a liquid-nitrogen feed through. A 750 L/s diffusion pump (Edwards, Willmington, MA) is placed below the drift tube to pump the high volume of gas used in the drift cell. The second 500L/s diffusion pump (Edwards) is placed below the time-of-flight (TOF) region to allow for at least $1x10^{-7}$ torr in the TOF region. Each instrument section will be broken down in the following sections.

The Ion Source

The electron impact ionization source is a modified Finnigan EI source from the 4000 series instrument (Finnigan MAT, Cincinnati, OH). The source produces an orthogonal electron beam from ion extraction. A plate was added to the front of the source to allow pulsed extraction of the ions. The ion extraction voltages are controlled by a pulse generator (Directed Energy, Inc, Fort Collins, CO). The ions are focused into the drift tube via a three membered Einzel lens.

The Drift Cell

The housing assembly of the IMS drift cell was machined from aluminum and the end caps machined from oxygen-free copper are mounted to the housing. The

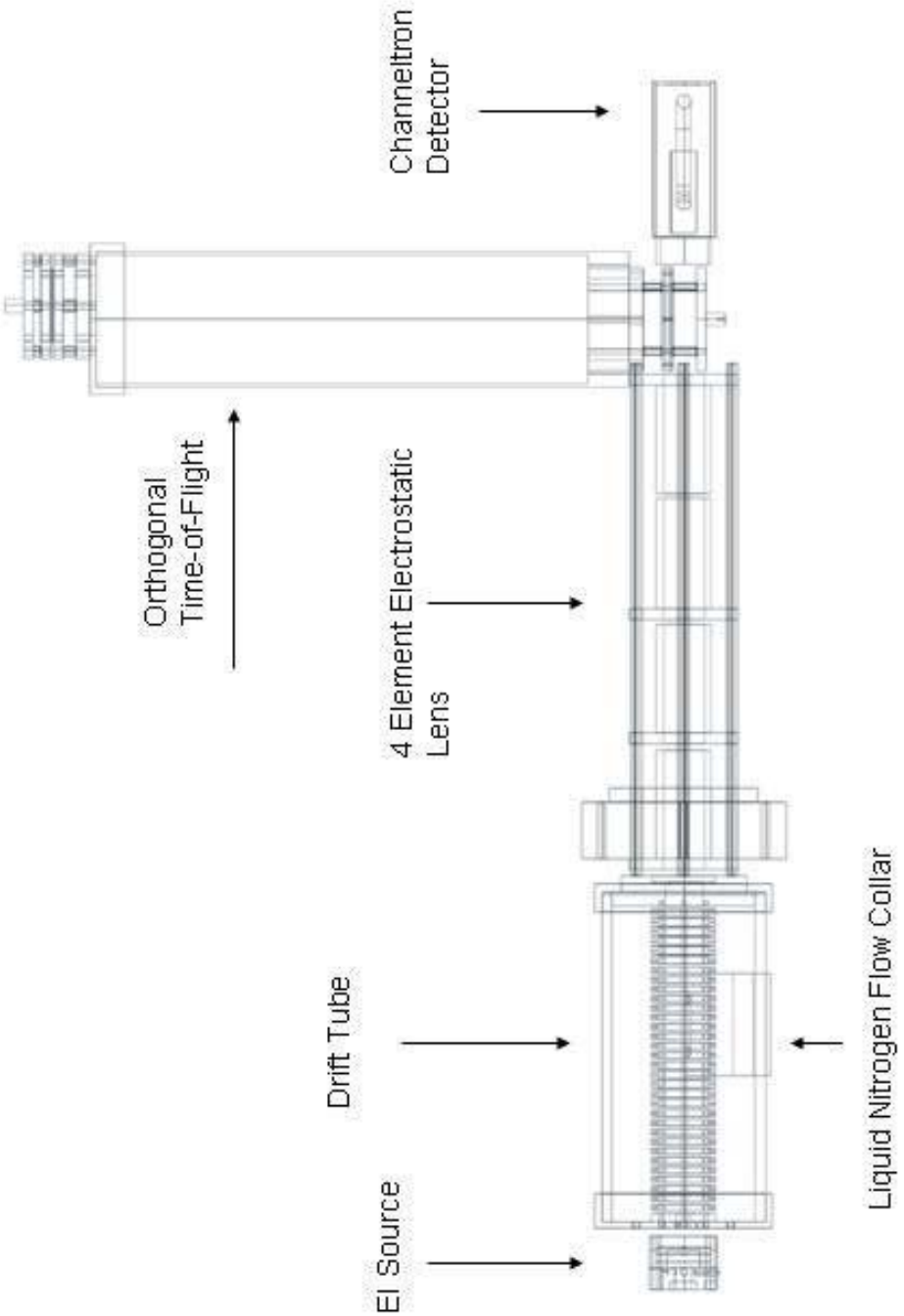

Figure 23: Schematic of the liquid nitrogen-cooled ion mobility – time-of-flight mass spectrometer.

aluminum housing has an outer diameter of 76.2 mm and an internal diameter of 66 mm, and is threaded to accept the end caps. The end caps have an outer diameter of 82.5 mm and are tapped to accept the drift gas inlet and temperature probe. The drift cell entrance orifice is 5mm and exit orifice is 0.5 mm. The drift tube houses 30-25.4 mm diameter lens elements spaced by 3.2 mm ruby balls and connected by 1 kΩ resistors to produce a linear field across the cell. A 59 mm diameter Macor® spacer is added to the end cap on the high voltage end of the drift cell for voltage insulation. An oxygen-free copper collar is place around the cell for the liquid nitrogen flow. Care was taken to ensure that the drift cell is thermally isolated from the surrounding instrument for maximum cooling efficiency and temperature stability.

The Lens and Mobility Detector

The drift cell is interfaced to the time-of-flight mass spectrometer by a 4 element electrostatic lens, which collimates and focuses the ions into the orthogonal TOF source. These lenses are 50.8 mm long with a 25.4 mm I.D. orifice and spaced with 3.2 mm ruby balls. The ions eluting the drift cell can be detected without mass analysis on an in-line Channeltron® (Burle, Lancaster, PA) electron multiplier. The ion signal can be collected on a LeCroy (Chestnut Ridge, NY) 9450 digital oscilloscope and signal averaged using the "summed average" process function.

The Time-of-Flight and Detector

The time-of-flight is positioned orthogonally to the drift cell and electrostatic lenses. The ions are focused into the pulsed extraction region which is controlled by a Directed Energy, Inc pulse generator. The ion packet of interest is extracted at 2 kV and

mass analyzed. The microchannel plate (Burle) detector is placed 8mm off the center line to compensate for the translational motion of the ions exiting the drift cell and the electrostatic focusing lens. The ions eluting the TOF are detected by using an 4 channel time-to-digital converter (Ionwerks, Houston, TX) and processed with Ionwerks TDCWin acquisition software.

Sample Introduction

The sample and drift gas inlet are controlled by 2 in-line leak valves (Nupro, Kurt J. Lesker, Pittsburgh, PA) for fine gas flow control. The drift cell pressure is calibrated by using the known mobility of Ar^+ in Ar drift gas at a particular drift cell temperature. This effectively eliminates the need for a capacitance manometer, which is unreliable at variable temperature and avoids unnecessary heating of the cell. The drift gas is liquid nitrogen-cooled prior to injection into the drift tube to aid in drift cell temperature control. All drift gases and sample gases are grade 5.0 (Praxair, Danbury, CT). The anhydrous methanol (Spectrum Chemical, Gardena, CA) is leaked into the ionization source using a variable leak valve (Varian, Lexington, MA) following freeze pump-thaw.

CHAPTER VI

VARIABLE-TEMPERATURE ION MOBILITY TIME-OF-FLIGHT MASS SPECTROMETRY STUDIES OF ELECTRONIC ISOMERS OF Kr^{2+} AND $CH_3OH^{+\bullet}$ RADICAL CATIONS

Background

Many ion mobility studies have investigated ion-neutral collision interactions of small mass ions (<200 amu).[77] The drift tube experiments can be used to probe thermodynamic and kinetic properties of colliding bodies, as well as for separation of isomeric (conformational and structural) and isobaric species. Charge transfer reactions for the rare gases is just one of many interactions that have been extensively studied.[78-81] Rare gas ions in their own neutral drift gas undergo symmetric charge transfer reactions (Equations 49 and 50), which are formally "spin forbidden", but have been shown to occur at relatively low collision energies (10 meV to 20 eV).[79,82]

$$A^+ + B \rightarrow A + B^+ \qquad 10/01 \qquad (49)$$

$$A^{2+} + B \rightarrow A + B^{2+} \qquad 20/02 \qquad (50)$$

$$A^{2+} + B \rightarrow A^+ + B^+ \qquad 20/11 \qquad (51)$$

These symmetric electron transfer reactions (10/01 and 20/02) were shown to be the dominant reaction pathways at these low energies by Hasted and Hussain.[79] Experimentally they demonstrated that the cross section of the 20/02 charge exchange was 5-10 times larger than that of the 20/11 exchange, and that the production of Kr^+ does not occur at collision energies below 20 eV.

The separation of the $^2P_{1/2}$ and $^2P_{3/2}$ states of Kr^+ and Xe^+ in their respective drift gases has been reported.[81,83-84] Also, Kr^{2+} and Xe^{2+} ions are reported, but only partially separated on the basis of mobility at 300K, which does not afford base line separation of the different electronic and spin states ($^3P_0$, $^3P_1$, $^3P_2$, $^1D_2$, and $^1S_0$).[85-87] A liquid nitrogen cooled drift tube experiment was designed by Koizumi *et al.* for high resolution separation and analysis of the doubly charged symmetric electron transfer reaction of Kr^{2+} and Xe^{2+}.[87] They showed that at temperatures of 88K the resolving power is sufficient to separate the different electronic states.

Variable temperature IMS was also demonstrated for the separation of conformational and electronic isomers of polyatomic ions.[25,88] Thus it may be practical to use IMS to address many of the long standing issues concerning structure and structural rearrangement reactions of gas-phase ions. Radom and coworkers showed that ionized methanol exists as two discrete structural forms, *viz.* the conventional $CH_3O^{\bullet+}H$ (methanol radical cation) and the distonic $CH_2^{\bullet}OH_2^+$ or methyleneoxonium radical cation.[89-91] On the basis of experimental and theoretical data, they proposed that the methyleneoxonium radical cation is a stable species, and in fact the distonic form is more stable than the conventional radical cation.[92]

In this report, we describe a new liquid nitrogen-cooled ion mobility orthogonal time-of-flight mass spectrometer. The instrument is evaluated by revisiting the Kr^{2+} charge transfer with Kr as the drift gas to illustrate the instrument's separation ability and peak resolution. We also demonstrate the use of variable temperature ion mobility

to separate conventional ($CH_3O^{+\bullet}H$) and distonic ($C^{\bullet}H_2O^{+}H_2$) radical cations of methanol.

Experimental

The instrument is configured to acquire ion signal after the mobility cell or time-of-flight mass spectrometer. The methanol ion signal was collected after the mobility cell. Mass assignments of the mobility peaks were determined by setting the digital delay generator to pulse extract the ions of interest into the time-of-flight mass spectrometer. For the krypton experiment the mass spectrometer detector was set to acquire only 42 m/z (Kr^{2+}). The resulting mobility trace represents the arrival time of the Kr^{2+} ion only.

Theoretical Details

All calculations were performed with Gaussian 98 (G98).[93] Our model for the Kr^{2+}/Kr^{0} collision complex was the Kr_2^{2+} dimer, and the ground and excited states were optimized using CASSCF(4,3)[94-95] for the spin multiplicity of 1 and 3. The Stuttgart RLC ECP[96] basis set was used with Kr. The potential energy surface for Kr_2^{2+} ion was scanned over an interaction distance of 1.8 to 4.0 Å. We use previous MP2/6-311+G(d,p) calculations on the methanol and methyleneoxonium radical cations, and the transition state corresponding to their interconversion to evaluate well depths and interaction distances for their potential energy surfaces.[90,97-99]

Results and Discussion

The motivation for designing a variable temperature ion mobility instrument is two-fold. That is, both ion mobility resolution (eq.17) and resolving power(eq.27)

increase as the temperature decreases, which is illustrated by combining the peak resolution equation (eq. 18) with the Nernst-Einstein relation (eq. 19);[100] The increase in resolution at decreased temperatures greatly facilitates separation of atomic and small molecule ions (resolving power), where the most significant factor limiting resolution is diffusional broadening.[33] Secondly, decreasing the temperature reduces the velocity of the neutrals thereby reducing the ion-neutral collision energy. Lowering the relative velocity of the collision partners decreases the collision barrier, thereby increasing the lifetime of the ion-neutral complex. In the absence of a strong ion-neutral interaction, hard sphere scattering is the only process that affects ion mobility and polarization and interactions are unimportant. This is most often seen as a good approximation for large ions (>500D), and not a good method for determining small molecule cross-sections. In this case the potential interaction surface is approximated by the Lennard-Jones potential only.

Equation 12 also underscores the importance of drift cell length on peak resolution. Our cell design is longer than most variable temperature drift cells, because this provides a two-fold increase in peak resolution. Although ion transmission and signal amplitude is decreased, this does not limit the scope of our experiments.

Krypton^{2+} Experiments

Figure 9 contains a plot of the ion signal versus arrival time of Kr^{2+} in Kr at 300 K(figure 9A) and at 90 K(figure 9B). Note that the peak resolution increases from R=5 to R=12.5 (as predicted by equation 17) when the temperature is decreased from 300 to 90 K. In addition, the resolving power increases by a factor of 4.3, revealing three peaks

in figure 9B that are unresolved (underneath Peak I) at 300 K. This increased resolution at 90K is sufficient to separate the different excited and spin states of Kr^{2+}. The electron impact (EI) energy is 80 eV, which is sufficient to populate all five states of Kr^{2+} ($^3P_0$, $^3P_1$, $^3P_2$ ~38 eV IE, and $^1D_2$, $^1S_0$ ~ 50 eV IE), having statistical weights of $^3P_0$=6.67 %, $^3P_1$=20.00 %, $^3P_2$=33.33 %, $^1D_2$=33.33 %, and $^1S_0$=6.67 %, respectively.

The separation of Kr^{2+} ions in the mobility drift tube occurs by symmetric charge transfer (eq. 50), and the abundance of the spin states are conserved owing to the "avoided crossing". The charge transfer is uniquely 2 e^- (eq. 50) at low collision energies (0.1-1 eV), because the production of two Kr^+ ions (by eq. 51) would generate a broad peak at later arrival times, which is not observed. This is thought to occur due to a high barrier height at the intersection of the potential energy surfaces of Kr_2^{2+} leading to the dissociation product of $Kr + Kr^{2+}$ or $Kr^+ + Kr^+$, respectively. Even though the products of the later dissociation are energetically favored, they are only observed at collision energies greater than 20 eV, when what is commonly referred to as the "avoided crossing" can be overcome.

Figure 24 contains a plot of Kr^{2+} signal versus the arrival time distribution at three ionization energies (Figure 24A, 80 eV; Figure 24B, 45 eV; and Figure 24C, 40 eV, respectively). Note that 4 peaks are observed of the 5 possible states. As the ionization energy is reduced from 80 to 40 eV, the intensity of two peaks are directly affected (i and iii), suggesting that these two ion signals are due to higher lying excited states ($^1D_2$, $^1S_0$) of Kr^{2+}. The integration of the ion signal of Peak iii (assuming a Gaussian profile) is approximately 35 % of the total integrated ion signal in Figure 24A.

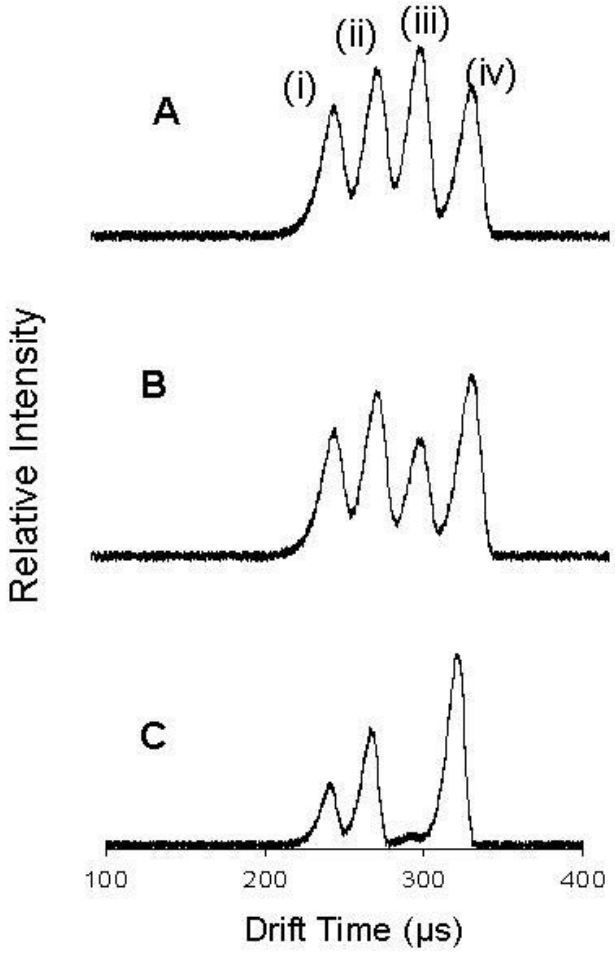

Figure 24. The ATD of Kr^{2+} in Kr at 0.5 Torr, 8 V/cm Eo, 90 K, and EI of 80 eV(**A**), 45 eV (**B**),and at 40 eV (**C**). Peaks labeled i-iv are discussed in the text.

By lowering the ionization energy to 40 eV (Figure 24C), Peak iii is dramatically depleted. Based on these observations and statistical weights of the states of Kr^{2+}, peak iii is assigned to $^1D_2$. Table III shows the relative abundance of peak I also decreases by lowering ionization energy. Because $^1S_0$ should also diminish at decreasing ionization energy, we propose that the $^1S_0$ peak co-elutes with one of the triplet states, indicated by the retention of 50% of the arrival time distribution signal at 40eV EI. At 40 eV, the remaining peaks are attributed to the three spin states of ^3P. These triplet states are further assigned based on their statistical weight ($^3P_0$(peak i)~8 %, $^3P_1$(peak ii)~19%, $^3P_2$(peak iv)~34%).

Complementary to these experiments, *ab initio* calculations of the potential energy surface for the singlet electronic excited states were performed. Figure 25 contains a plot of energy versus the reaction coordinate, which suggests the $^1S_0$ is slightly less reactive than the $^1D_2$ due to a shallower well, ε=2.5 eV for $^1S_0$ and 3.0 eV for $^1D_2$. At the MP2 level of theory, this interaction difference predicts that the $^1S_0$ should have a smaller collision cross-section, thereby increasing the mobility (faster drift time) of $^1S_0$ compared to the $^1D_2$. This interpretation provides additional support for the $^1S_0$ and $^1D_2$ peak assignments given above.

Methanol Radical Cation Preliminary Experiments

Figure 26 contains a plot of the arrival time distribution (ATD) for the methanol radical cation (m/z=32) and the fragment ions (m/z=31, 30) at 14 eV ionization energy in Ar drift gas at 90 K. The ATD for m/z 32 ion signal is bimodal, which we attribute to the presence of both the methanol radical cation (conventional) and methyleneoxonium

Table III. Electron impact energies (eV) and relative peak abundance for Figure 24.

EI Energy (eV)	Peak i	Peak ii	Peak iii	Peak iv
80	20	19	35	32
45	15	20	14	35
40	8	19	<1	34

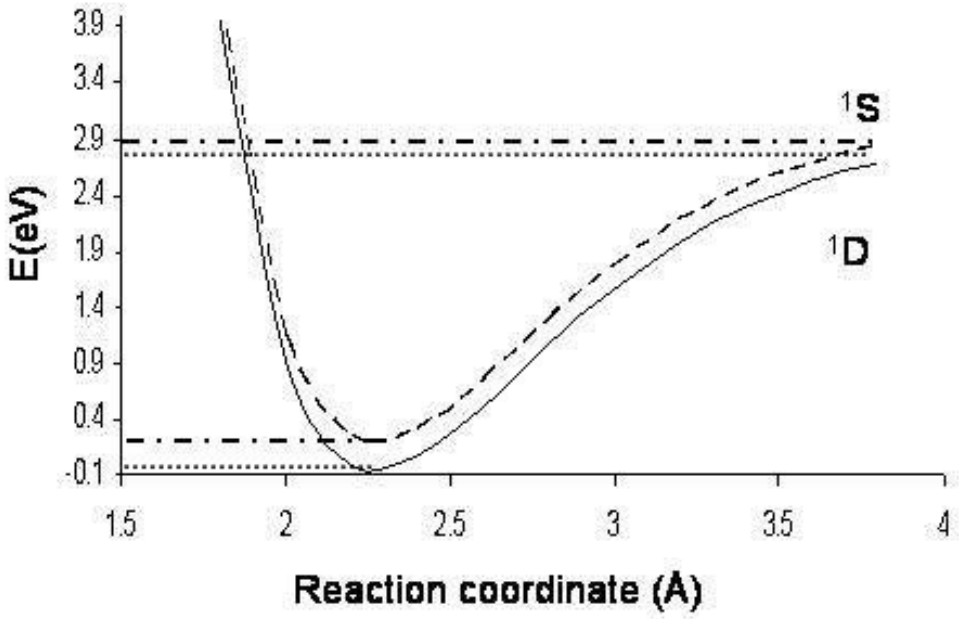

Figure 25. *ab initio* CASSCF(4,3) calculations of the singlet states of Kr^{2+} reacting with Kr.

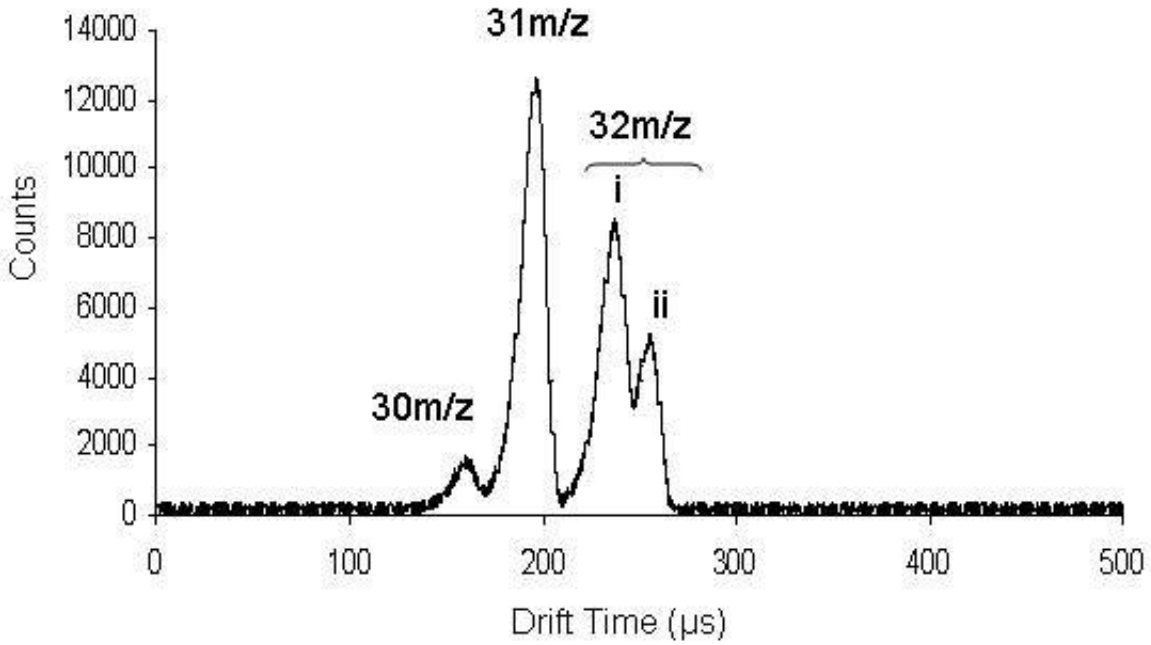

Figure 26. The ion signal versus drift time plot of methanol ionized at 14eV and separated at 8.5 V/cm•Torr in Argon at 90K. Labled peaks i and ii are discussed in the text.

radical cations (distonic). Under the experimental conditions used, interconversion between the two species is not observed on the time scale of the experiment (~250 μs), because the ions are immediately collisional cooled in the drift cell following ionization (collision energy <0.1 eV). Interconversion of the ion forms would be observed as coalescence of the two signals into one peak. Note that the peak width for m/z 31, which is composed of a single ion structure, and the two m/z 32 signals are approximately equal (~17μs). Note that the separation apparent in Figure 26 could not be observed at 300 K due to insufficient mobility resolution at elevated temperatures.

The potential energy surfaces for the interactions between the two radical cations with Ar is dissimilar due to the difference in dipole moment between the conventional and distonic radical cations (~0.2 Debye). Also, the hard sphere collision cross-section differs by nearly 7 % (33.5 $Å^2$ for the methanol radical cation and 35.9$Å^2$ for the methyleneoxonium radical cation) which is sufficient for mobility separation using the current instrument. The collision cross-section differences were predicted using "MobCross", a program developed in house utilizing the projection approximation to calculate the collision cross-section of gas phase ions.[100-101] Based on these observations we are able to assign the methanol radical cation peak to the ion signal at 228 μs (Peak i), and the methyleneoxonium peak to the signal at 252 μs (Peak ii).

Figure 27 illustrates the barrier height to dissociation and interconversion of the methanol radical cation. The barrier to interconversion was calculated by Radom and coworkers to be 0.6 eV greater than the conventional radical cation, which is approximately 0.1 eV higher than the loss of H• dissociation pathway. The

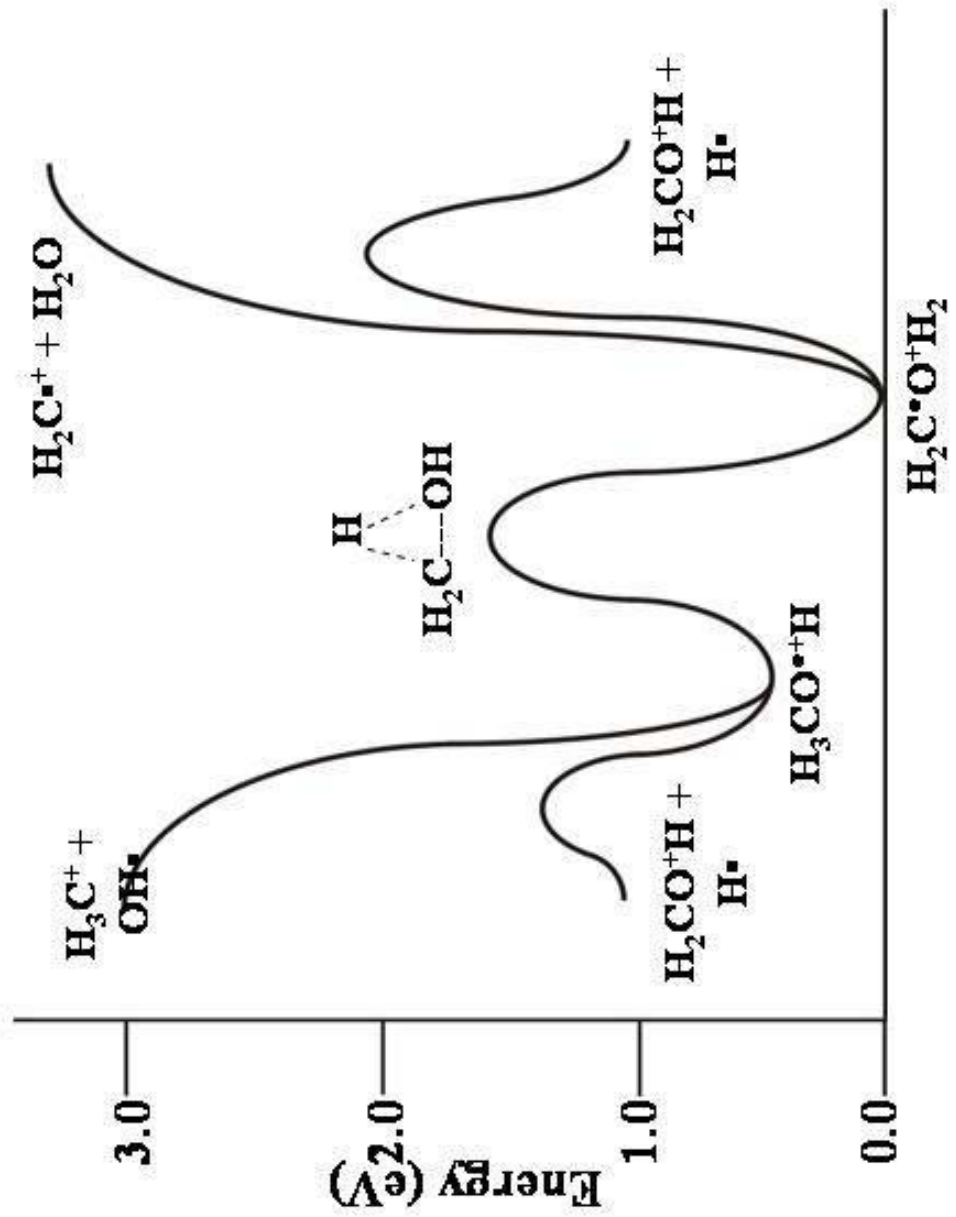

Figure 27. Reaction coordinate of the ionization and dissociation pathways of the methanol radical cation.

methyleneoxonium radical cation was calculated to be 0.3 eV more stable than the conventional radical cation[89]. Because of the presence of an energy barrier to interconversion, the distonic ion should be formed in much smaller abundance than the conventional radical cation. This is also consistent with our peak assignments of the arrival time order of the distonic and conventional radical cations. We have also measured the ATD of other CH_3X (X=NH_2 and F) and the data are also consistent with the proposed peak assignments.[102]

CHAPTER VII

SEPARATION OF CONVENTIONAL AND DISTONIC RADICAL CATIONS OF CH_3-X (X=OH, NH_2, F) USING VARIABLE TEMPERATURE ION MOBILITY TIME-OF-FLIGHT MASS SPECTROMETRY

Background

Variable temperature IMS may then be practical to address long standing issues concerning structural rearrangement reactions of gas-phase ions. Figure 28 shows the effect of the interaction between an ion and the buffer gas for different temperatures. Based on Bowers' equation[21] (eq. 7), by cooling the buffer gas we are able to probe ion-molecule interactions more efficiently. Holmes and coworkers have shown using collisional activated mass spectrometry the existence of a conventional and distonic (separation of charge and radical sites[103]) radical cations of CH_3X, where X is –OH, -NH_2, -F, -SH, -Cl, -Br, and –I.[104-105] Radom *et al.* used *ab initio* theoretical methods, including G2, which has been shown to provide relatively reliable energetics for comparing small organic molecules, to study these CH_3X radical cations.[91,106] Here, they calculated the relative stability of the conventional and distonic species, demonstrating that the distonic species is more stable for X=-OH, -NH_2, and –F in agreement with experiment. Other groups have also calculated these structures and thermodynamics using density functional theory density functional theory (DFT).[107] They also attempted to predict the effect of various buffer gases (Ar, Xe, N_2) on the barrier height for interconversion between the conventional and distonic forms. Frigden and Parnis demonstrated that B3LYP and BP86 functionals do not agree well with the

experimentally determined relative energies of the conventional and distonic methanol radical cations.

Truhlar and coworkers developed the MPW1K functional, which has empirically optimized parameters for reaction kinetics.[108-109] This method shows merit to the application of gas-phase radical cation structure and energetics. The mPW1PW91 level of theory has a low computational cost and has been shown to predict good kinetic values for a broad range of reactions.

In this report, we describe variable temperature ion mobility/mass spectrometry applied to the separation of the conventional and distonic radical cations of CH_3OH, CH_3NH_2, and CH_3F. We use different buffer gases to probe the separation of these species and confirm the lowering of the barrier to interconversion between the conventional and distonic forms. We apply several DFT functionals, including MPW1K and B3LYP hybrid functionals with various basis sets to determine the structure and energies, and compare these values to more commonly used *ab initio* calculations.

Experimental

A new instrument was employed for the study of the separation of the conventional and distonic radical cations. The instrument couples ion mobility with orthogonal time-of-flight. Interchangeable sources can be added to the instrument to make it more versatile; however, the electron impact was employed for the ionization of the CH_3-X compounds. Figure 23 shows the schematic of the instrument. Details of the instrument have been described previously.[44]

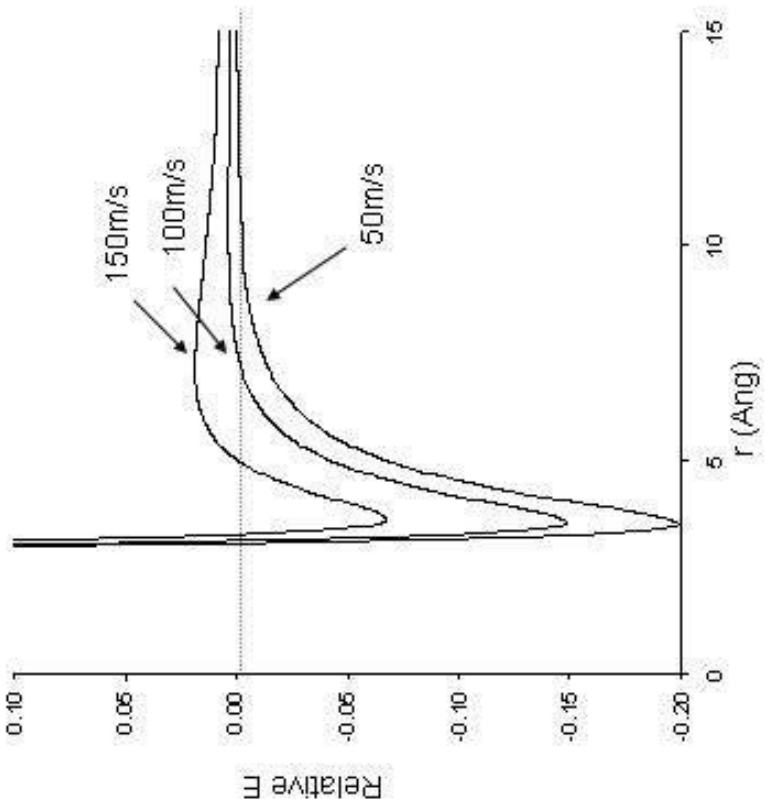

Figure 28. Plot of interaction potential for different relative speeds of buffergas, as related to temperature.

The anhydrous methanol (Spectrum Chemical, Gardena, CA) is leaked into the ionization source using a variable leak valve (Varian, Lexington, MA) following freeze pump-thaw. Anhydrous methylfluoride and methylamine (Aldrich, Milwaukee, WI) were leaked in through an in-line leak valve (Nupro, Kurt J. Lesker, Pittsburgh, PA) for fine gas flow control. The ionization energy for methanol, methylamine, and methylfluoride was 11.5, 10.5, and 14.0, respectively.

Computational Details

The theoretical calculations have been carried out using the Gaussian98[93] implementations of various wave function theories, second-order (MP2), third-order (MP3), and fourth order (MP4) Møller-Plosset[97], coupled cluster, with (CCSD(T)) and without (CCSD) pertubative triples; and various DFT theories, B3LYP [Becke three-parameter exchange functional (B3)[110] and the Lee-Yang-Parr correlation functional (LYP)[111]] and MPW1K[108] [the "modified Perdew-Wang 1-parameter model for kinetics" which is the modified Perdew-Wang exchange functional (mPW) and the Perdew-Wang correlation functional (PW91) with an empirically optimized addition of 42.8% Hartree-Fock (exact) exchange, fit using reaction energies and activation barriers of free radical reactions as described by Truhlar and coworkers[108]] density functional theory (DFT).[112] All *ab initio* calculations used the default SCF convergence for geometry optimizations (10^{-8}). All DFT calculations used the default pruned fine grids for energies (75, 302), default pruned course grids for gradients and Hessians (35, 110), and default SCF convergence for geometry optimizations (10^{-8}). BS1 utilized the 6-31G(d) basis sets of Pople and coworkers[113] for all atoms. BS2 replaces the basis set for carbon, oxygen,

nitrogen from BS1 with 6-31+G(d').[114] BS3 utilized the 6-311+G(d)[99] basis set for carbon, oxygen, nitrogen, and fluorine and uses Stuttgart relativistic, large core ECP (Stuttgart RLC-ECP)[115] basis set for argon, krypton, and xenon (Stuttgart designations:[116] Ar: ECP10MWB; Kr: ECP28MWB; Xe: ECP46MWB). Cartesian *d* functions were used with BS1 and BS2, and spherical harmonic *d* and *f* functions were used with BS3. All structures were fully optimized, and analytical frequency calculations were performed on all structures (except MP3 optimized structures) to ensure either a minimum or 1st order saddle point was achieved. All relative energies are electronic energies with zero point energy, unless otherwise noted. Throughout this paper, bond angles are in degrees, bond lengths are in angstroms, and energies are in electron volts (eV). The associated scheme in Figure 29 is of the systems we examined.

Results and Discussion

Theoretical

Table IV shows the results of the relative energies (ΔE) of the distonic radical cation compared to the conventional radical cation. For the ΔE between the methanol ($CH_3OH^{+\bullet}$) and methyleneoxonium ($CH_2OH_2^{+\bullet}$) radical cation and between the methylamine ($CH_3NH_2^{+\bullet}$) and methyleneammonium ($CH_2NH_3^{+\bullet}$) radical cation, the results are scattered low (B3LYP) and high (MP2), with MP3 showing improvement over the MP2 results. MPW1K/6-31 +G(d',p') are surprising close to the experimental values and are improved from the more computationally expensive MP3 calculations. Interestingly, all of the single wave function theories and DFT methods shows inconsistent behavior for the ΔE of the methylfluoride ($CH_3F^{+\bullet}$) and

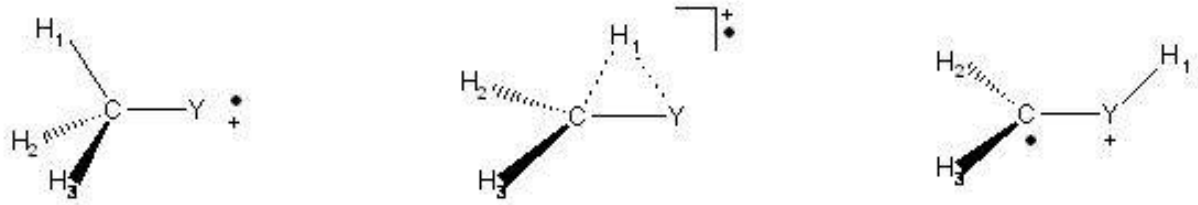

Figure 29: Schematic of a conventional radical cation (A), the transition state (B), and the distonic radical cation (C).

Table IV: Calculated energy differences (ΔE) of the distonic radical cations compared to their conventional forms in eV. All values have been corrected with ZPEC.

Level of Theory		$CH_2OH_2^{+\bullet}$	$CH_2NH_3^{+\bullet}$	$CH_2FH^{+\bullet}$
B3LYP	6-311+G(d,p)	-0.060	0.071	0.119
B3LYP	6-31+G(d',p')	-0.048	0.086	0.110
MP2	6-311+G(d,p)	-0.597	-0.164	-0.121
MP2//MP3	aug-cc-pVDZ	-0.511	-0.164	-0.096
MP3	6-31+G(d',p')	-0.355	-0.084	-0.373
MP3	aug-cc-pVDZ	-0.339	-0.087	-0.321
MPW1K	6-31+G(d',p')	-0.305	-0.006	-0.060
MPW1K	aug-cc-pVDZ	-0.265	0.004	-0.024
MPW1K	aug-cc-pVTZ	-0.298	-0.008	-0.027
G3B3		-0.311	-0.047	-0.166
Exp†		-0.314	-0.010	-0.497

methylenefluorodium ($CH_2FH^{+\bullet}$). This seems to be independent of the level of theory and basis set changes. Table V tabulates structural data of the methylfluoride radical cation. Small structural changes in the bond length and angle can be noted, but nothing extreme enough to warrant the erratic energy fluctuations. Table VI shows the bond lengths and bond angle for the distonic radical cation. Also here, small changes to the geometry can be seen; however, there is no trend associated with the changes in the energy. Appling any of these geometries to a G2 or G3 calculation will produce a similar ΔE (~0.12eV), as seen by Radom *et al.*[106]

Table VII shows the results from the *ab initio* single point energy on the B3LYP/G3Large geometries. The HF results over estimate the stability of the distonic isomer, while going to higher levels of perturbation theory, the energy difference of the distonic compared to the conventional gets smaller. The MP3 and MP4DQ results fortuitously come closer to the experimental results; however, increasing level of theory produces consistently lower results compare to experiment. Examination of the unrestricted HF wavefunction reveals the spin contamination of the ground state wavefunction of the conventional methylfluoride radical cation. Performing a restricted open shell HF calculation reveals multireference character in the wavefunction. Therefore, these single reference techniques will not converge to accurate results.

Ion Mobility Results

Figure 30 shows an arrival time distribution (ATD) versus m/z for methanol ionized at ~11.5eV (m/z 32) and the dissociation products (m/z 31, 30). The

Table V: Bond lengths (ang) and angles (degrees) for the optimized geometries of the methylfluoride radical cation.

Level of Theory		r(C-H_1)	r(C-Y)	$\angle H_1CY$
B3LYP	6-311+G(d,p)	1.2904	1.0887	116.71
B3LYP	6-31+G(d',p')	1.2995	1.0904	116.18
MP2	6-311+G(d,p)	1.2904	1.0877	118.47
MP3	6-31+G(d',p')	1.2838	1.0827	117.79
MP3	aug-cc-pVDZ	1.2834	1.0959	118.5
MPW1K	6-31+G(d',p')	1.2671	1.0852	117.73
MPW1K	aug-cc-pVDZ	1.2718	1.0887	118.06
MPW1K	aug-cc-pVTZ	1.2629	1.0818	118.18

Table VI: Bond lengths (ang) and angles (degrees) for the optimized geometries of the methylfluorodium radical cation.

Level of Theory		r(C-Y)	r(Y-H_1)	$\angle H_1YC$
B3LYP	6-311+G(d,p)	1.568	0.9551	114.26
B3LYP	6-31+G(d',p')	1.5911	0.9554	115.9
MP2	6-311+G(d,p)	1.551	0.9494	114.97
MP3	6-31+G(d',p')	1.566	0.9429	115.41
MP3	aug-cc-pVDZ	1.5768	0.9492	113.77
MPW1K	6-31+G(d',p')	1.5444	0.943	116.53
MPW1K	aug-cc-pVDZ	1.5413	0.9443	114.49
MPW1K	aug-cc-pVTZ	1.5169	0.9438	114.96

Table VII: Single-point energies (eV) of the distonic radical cation of methylfluoride compared to the conventional form without zero-point energy corrections.

Basis Set	HF	MP2	MP3	MP4D	MP4DQ	MP4SDQ	MP4STDQ	CCSD	CCSD(T)
6-31++G(d',p')	-0.835	-0.277	-0.386	-0.371	-0.396	-0.337	-0.257	-0.347	-0.284
6-31++G(d',p') with 6-211 for F	-0.835	-0.280	-0.387	-0.371	-0.398	-0.341	-0.261	-0.350	-0.284
6-311++G(d,p)	-0.794	-0.255	-0.364	-0.346	-0.372	-0.311	-0.226	-0.320	-0.250
6-311++G(d,p) with 6-2111 for F	-0.794	-0.252	-0.362	-0.343	-0.370	-0.309	-0.224	-0.317	-0.247
g3large	-0.719	-0.154	-0.267	-0.248	-0.281	-0.223	-0.129	-0.235	-0.159
g3large with 6-2111 for C and F	-0.719	-0.153	-0.267	-0.246	-0.280	-0.222	-0.126	-0.234	-0.156
cc-pvdz	-0.775	-0.229	-0.327	-0.313	-0.338	-0.280	-0.207	-0.289	-0.229
cc-pvdz and 7/611 for F	-0.775	-0.228	-0.328	-0.313	-0.338	-0.280	-0.206	-0.289	-0.229
aug-cc-pvdz	-0.770	-0.234	-0.334	-0.320	-0.347	-0.292	-0.218	-0.305	-0.246
aug-cc-pvdz and 7/611 for F	-0.769	-0.233	-0.334	-0.320	-0.346	-0.292	-0.217	-0.305	-0.245
aug-cc-pvtz	-0.748	-0.183	-0.296	-0.277	-0.311	-0.253	-0.158	-0.266	-0.189

mobility was run in 1 torr Ar at 90K. As can be seen, m/z 32 has 2 peaks associated with it, though not base line resolved. The integrated ratio is ~4:1 for the lower compared to the higher arrival time distribution. The mobility peak resolution (t/Δ) is ~11.3 and the mass resolution ($m/\Delta m$) is 52.3. The two peaks at m/z 32 are proposed to be the methanol and the methyleneoxonium radical cations formed from the ionization of methanol. A bimodal signal cannot be obtained for m/z = 32 at 300K.

Theoretical results from this group and others have proposed the existence of two stable species, the conventional radical cation ($CH_3OH^{+\bullet}$) and the distonic ($CH_2OH_2^{+\bullet}$). Experimental photoelectron spectroscopy and collisionally activated mass spectrometry have confirmed the existence of two stable m/z = 32 species upon ionization of methanol. The methyleneoxonium radical cation has been shown to be ~0.3 eV more stable. Under the experimental conditions used, interconversion between the two species is not observed on the time scale of the experiment (~250 μs), because the ions are immediately collisional cooled in the drift cell following ionization (collision energy <0.1 eV). Interconversion of the ion forms would be observed as coalescence of the two signals into one peak.

The peak assignments were determined by a look at potential energy surfaces for the interactions between the two radical cations in Ar. They are resolved due to the difference in dipole moment between the conventional and distonic radical cations (~0.2 Debye). Figure 31A shows the calculated attractive potential of the two species. Another discriminating factor is the hard sphere collision cross-section differs by nearly

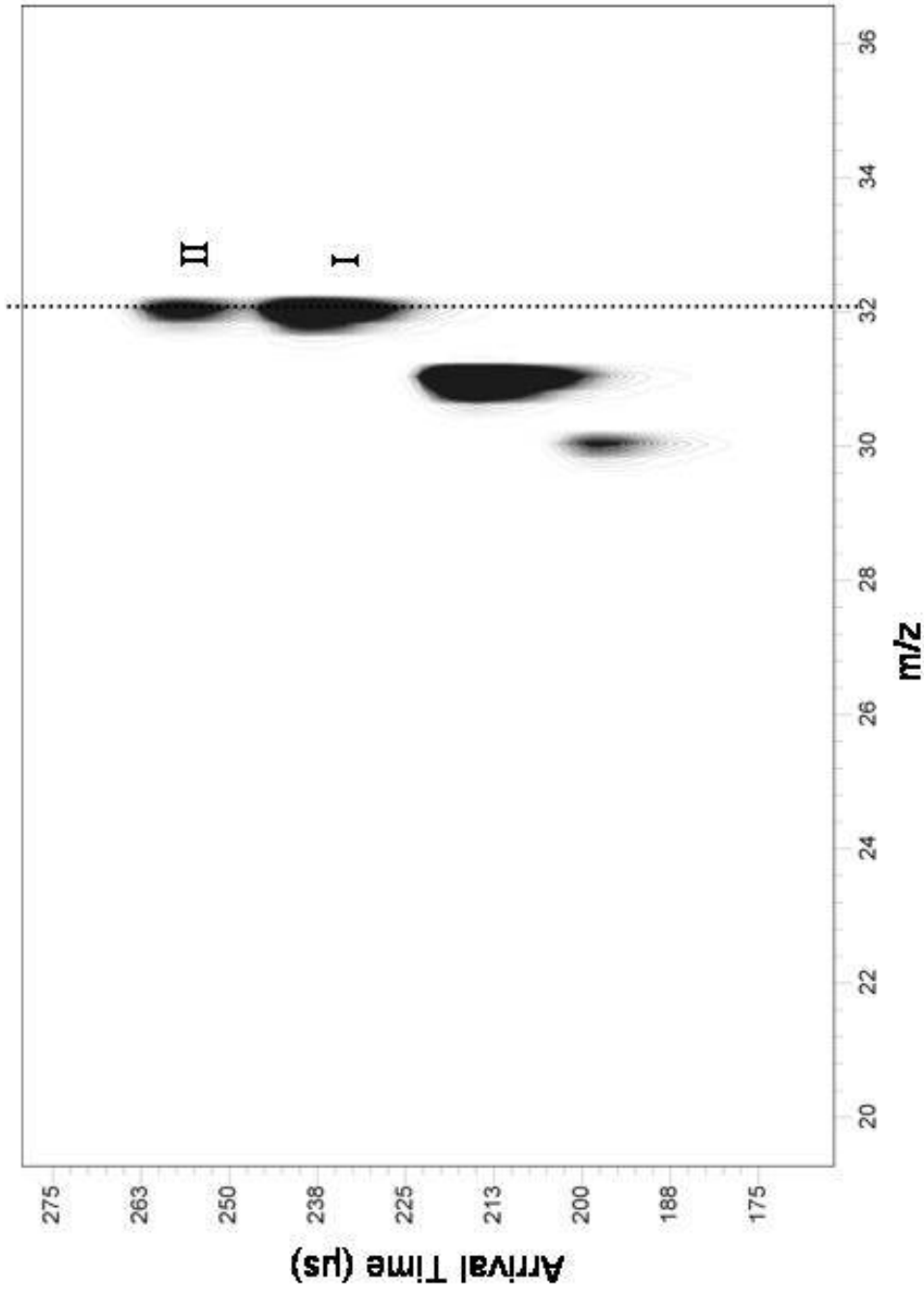

Figure 30: The arrival time distribution versus m/z for methanol (32m/z) and the dissociation products (31 and 30m/z). The plot was collected using 1 torr Ar buffer gas at 90K with an ionization potential of 11.5. The field applied across the drift cell was 8.2V/cm.

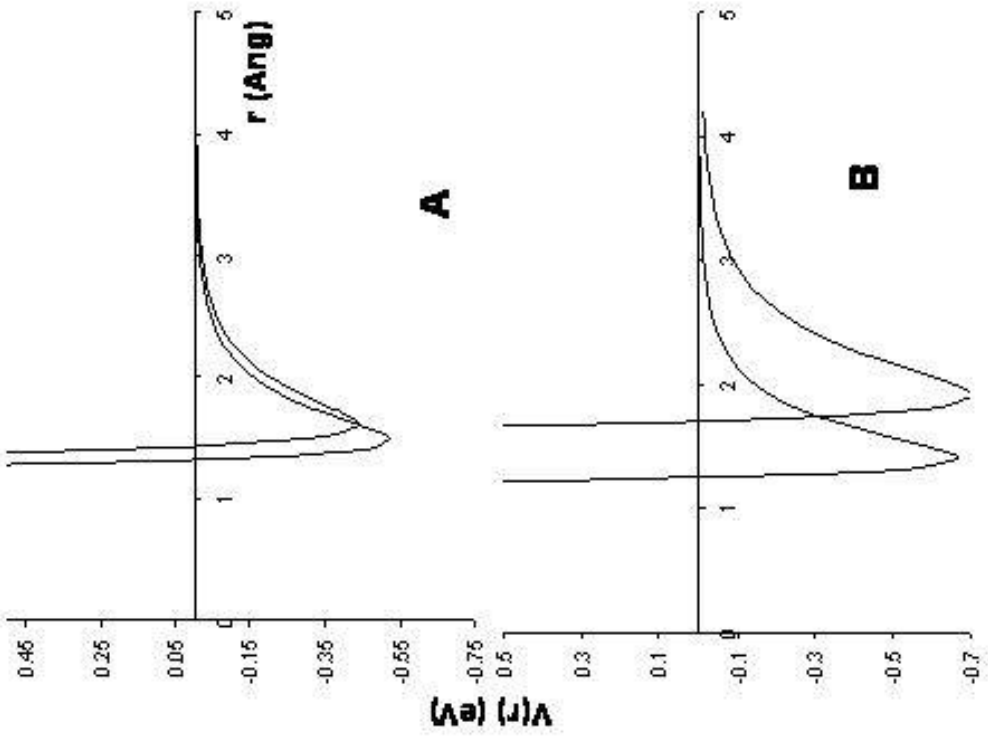

Figure 31: The attractive potential energy surface for the dipole-induced dipole interaction for methanol (A) and methylfluoride (B).

7 % (33.5 $Å^2$ for the methanol radical cation and 35.9$Å^2$ for the methyleneoxonium radical cation) which is sufficient for mobility separation with the current instrument's peak resolution. Therefore based on peak ratio, potential interaction, and cross-section, peak I is assigned the methanol radical cation and peak II the distonic form.

Similar experiments were performed for methylfluoride, which has been shown to have two stable electronic forms. Figure 31B shows an even greater dipole-induced dipole interaction difference, which should translate to an even better resolved separation between the conventional and distonic forms. Figure 32 shows the ATD versus m/z for the methylfluoride radical cation and the dissociation products. Here, baseline separation is achieved, which is expected due to the large dipole differences of the two species (~4.0 for methylfluoride radical cation and ~1.5 for the methylfluorodium radical cation). Once again separation between the 2 stable radical cations can not be achieved at temperatures greater than 200K.

Methylamine was the final CH_3-X compound explored. Figure 33 is the ATD versus m/z plot for ionized methylamine (31m/z) and the dissociation products (30 and 29m/z) ionized at 10.5 eV. Here, separation is not observed for the conventional and distonic forms of $CH_3NH_2^{\bullet+}$; however, peak resolution has changed from ~11 (seen for the 30 and 29m/z peaks) to 6.7 for the methylamine radical cation. We attribute this to the presence of both the conventional and distonic radical cations without the ability to fully resolve at 90K in Ar. This behavior is proposed to occur because of a narrow dipole moment difference in combination with an exact scattering cross-section of the two radical cation forms.

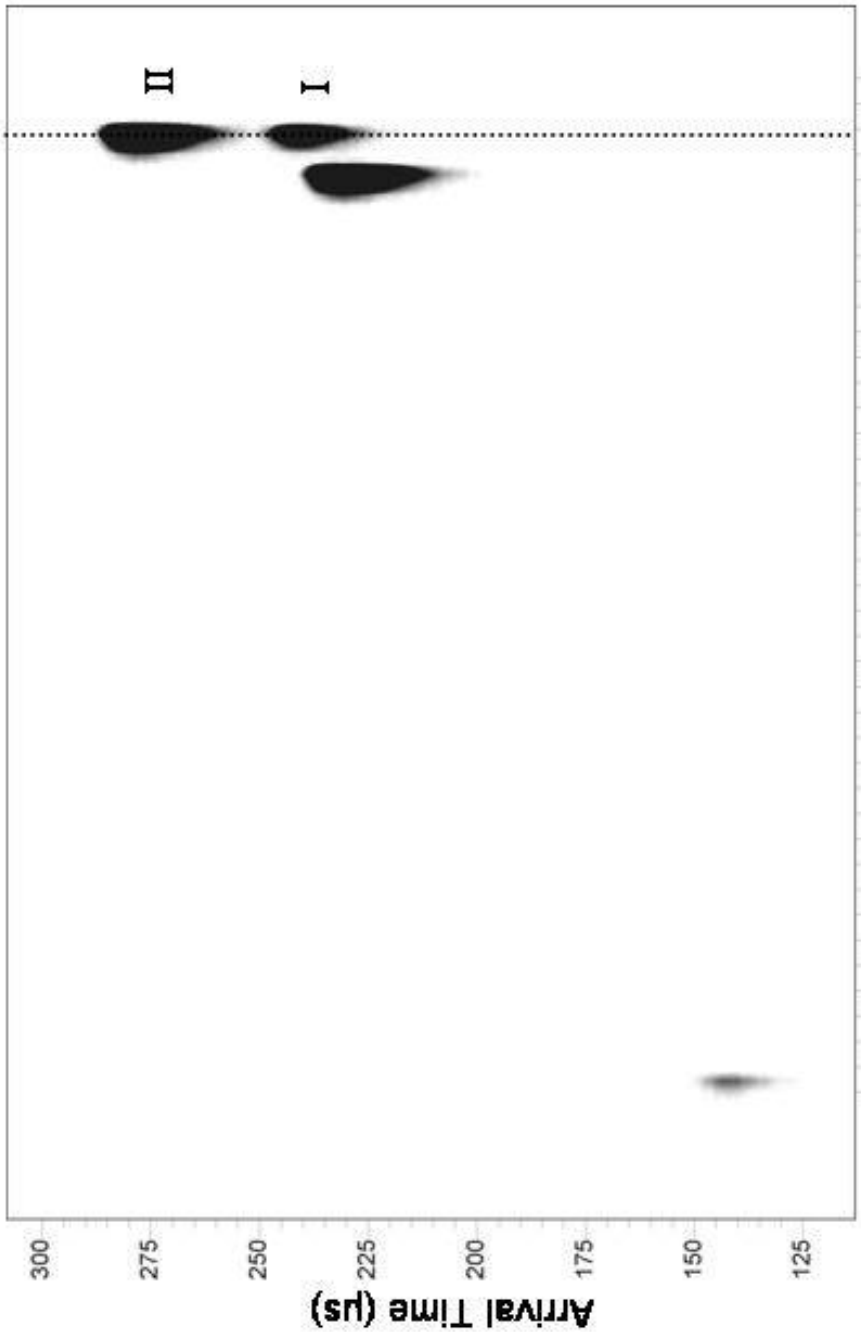

Figure 32: The arrival time distribution versus m/z for methylfluoride (34m/z) and the dissociation products (33 and 15m/z). The plot was collected using 1 torr Ar buffer gas at 90K with an ionization potential of 14.0. The field applied across the drift cell was 8.2V/cm.

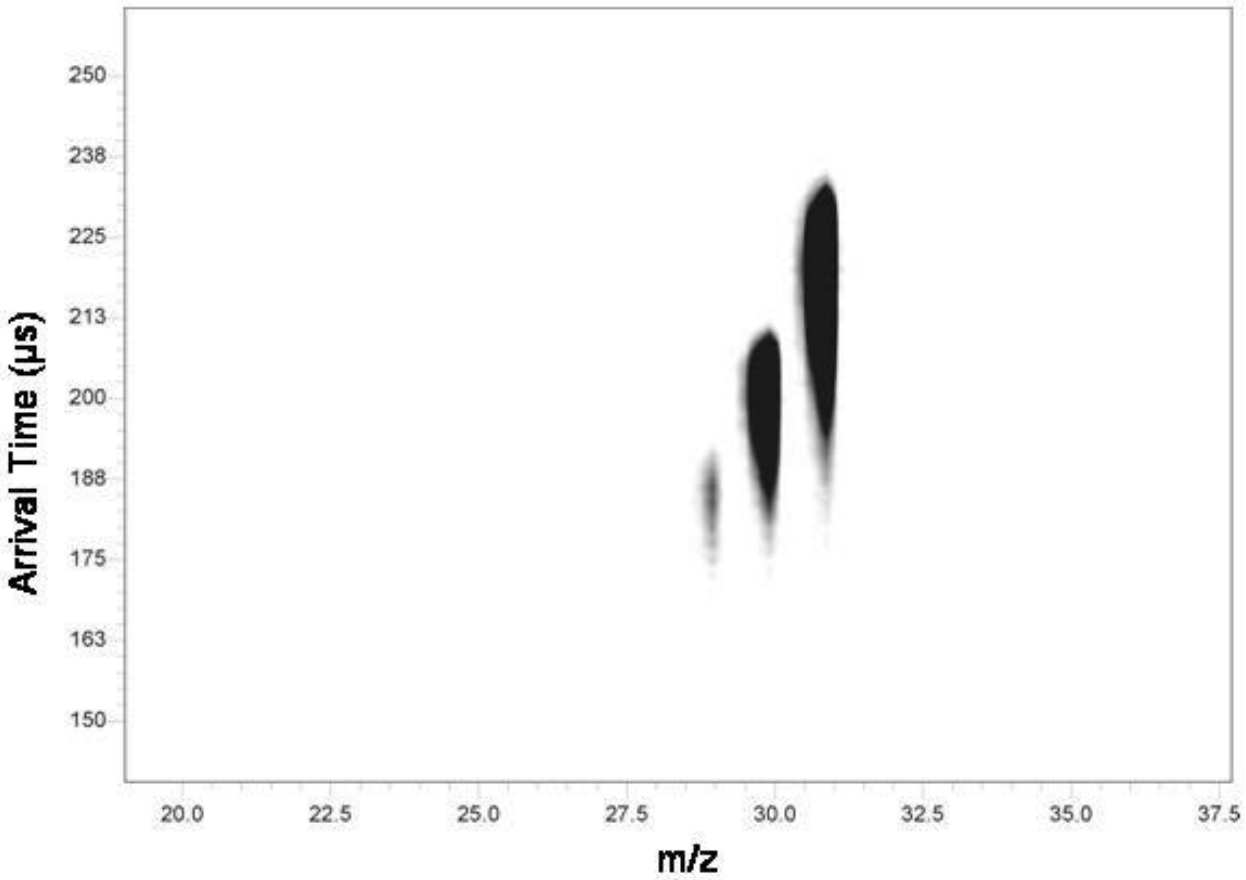

Figure 33: The arrival time distribution versus m/z for methylamine (31 m/z) and the dissociation products (30 and 29m/z). The plot was collected using 1 torr Ar buffer gas at 90K with an ionization potential of 10.5. The field applied across the drift cell was 8.2V/cm.

It has been shown by Holmes *et al.* that the barrier to isomerization between the conventional and distonic forms of methylfluoride can be lowered in the presence of increasing mass noble gases. This is thought to occur due to the noble gas acting as a neutral base to catalyze the 1,2-H shift between the methylfluoride and methylfluorodium radical cations. MP3/6-311+G(d,p) calculations were performed on the $CH_3F^{+\bullet}$ transition state in the presence of Ar, Kr, and Xe buffer gases. The barrier lowered from 0.96eV in Ar, 0.50eV in Kr, and 0.02eV in Xe with respect to the conventional radical cation energy. By using the Xe buffer gas, theory predicts only the more favorable distonic species (0.497 eV lower in energy than the conventional form) should elute from the buffer gas.

Figure 34 shows the arrival time distribution plots of the 34m/z mass only in Ar (A), Kr (B), and Xe (C). The methylfluoride radical cation has eluted the drift cell as one peak in the presence of Xe buffer gas. The resolution is expected to decrease with the increase in buffer gas mass; however, the resolution for the 34m/z peak is ~7.0 $t/\Delta t$ which corresponds to the resolution of the known single isomer of 33m/z (~6.8 $t/\Delta t$).

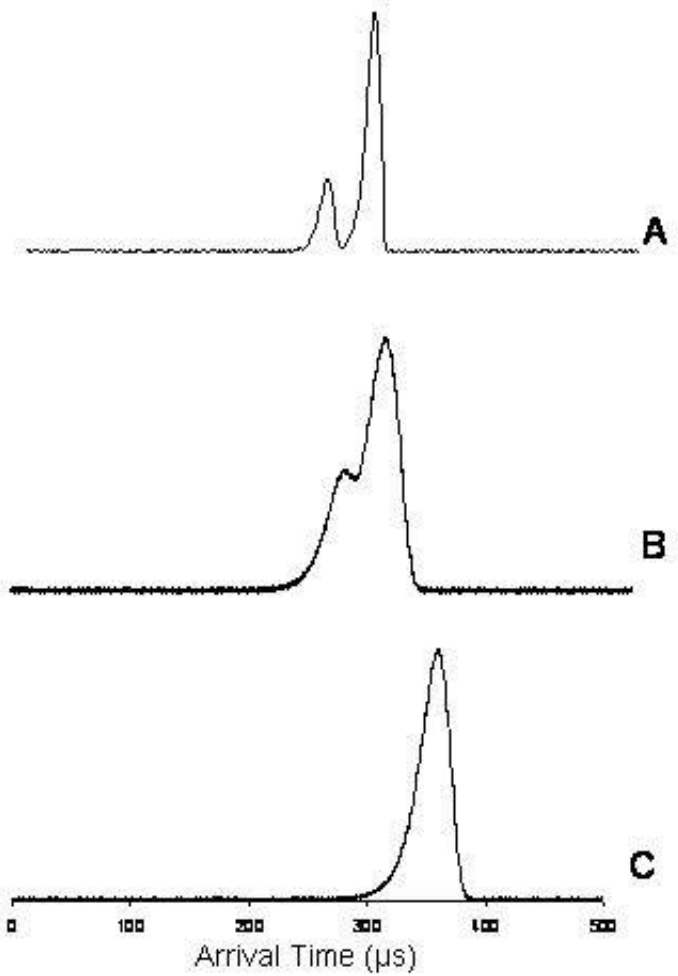

Figure 34: The arrival time distribution of methylfluoride in Ar (A), Kr (B), and Xe (C) buffer gases. The plots were collected at 1 torr, and 90K, 95K, and 104K, respectively.

CHAPTER VIII

SEPARATION OF THE KETO AND ENOL FORMS OF THE ACETONE RADICAL CATION AND THE IDENTIFICATION OF THE M/Z=58 DISSOCIATION PRODUCT FROM 2-PENTANONE AND 2-HEPTANONE USING VARIABLE TEMPERATURE ION MOBILITY

Background

One of the most widely studied mass spectral fragmentation processes is the γ-H transfer from an aliphatic group to the carbonyl group of a ketone to produce a m/z=58 ion (Figure 35).[117] This process, also known as the "McLafferty rearrangement"[118-119] has been a focus of mass spectral analysis since its conception. For species containing an alkyl group, R-CH_2CH_2-, joined with a carbonyl group (Figure 36a), a six-membered ring transition state is formed which allows for transfer of the γ-H.[119-121] Beauchamp showed evidence using ion cyclotron resonance spectrometry of the existence of an ion with the structure of Figure 36b.[122] Once the transfer is complete, charge is retained on the oxygen atom, and β-cleavage occurs, resulting in an odd electron enol ion.

Metastable ion abundances[123], kinetic energy measurements[124], and isotopic labeling[125] experiments have been performed using sector mass spectrometers[126], ion cyclotron resonance mass spectrometers[127], and ion traps to study the validity of McLafferty's mechanism. The main support for this rearrangement is the production of the odd electron enol ion at m/z=58. Most of the experiments performed to date have

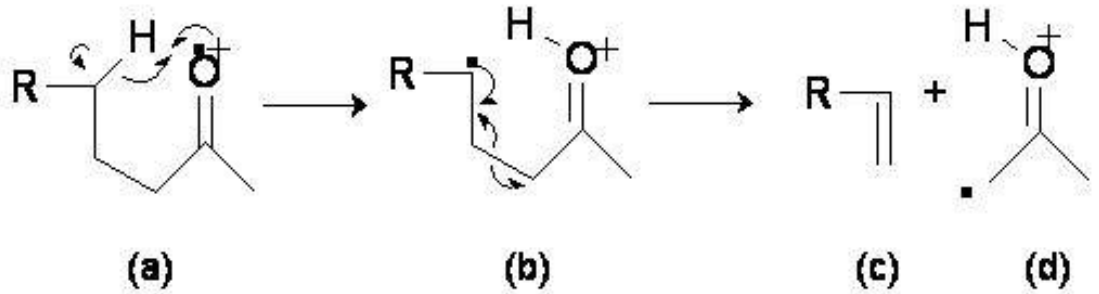

Figure 35. Schematic of the γ-H rearrangement to the unsaturated group with β-cleavage, also known as the "McLafferty rearrangement".

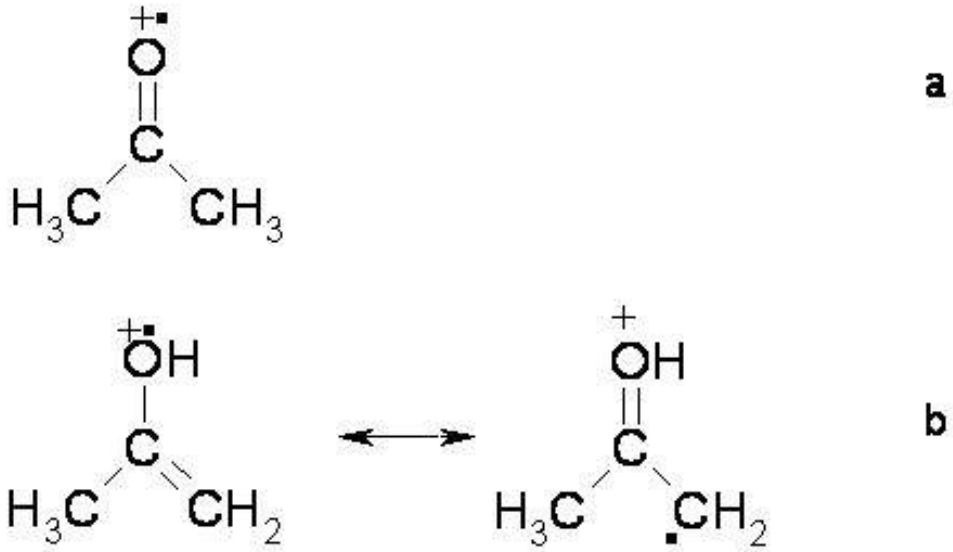

Figure 36. Representation of the (a) keto form and (b) resonance enol forms of the acetone radical cation.

agreed that the m/z=58 species is the enol form as opposed to the keto form, however, no direct method has been employed to definitively rule out the keto form.

It is well known that thermodynamics favor the keto isomer over the enol isomer for neutral species; however, it has been shown both experimentally and theoretically that the enol form (figure 36b) of the acetone radical cation is 0.3 eV more stable than its keto (figure 36a) counterpart.[128-131] There exists a barrier to interconversion of 1.1 eV between the keto and enol forms, allowing for studies of the isomeric species when cooled.[132]

Experimental

The variable temperature ion mobility/ time-of-flight instrument was employed for the study of the separation of the keto and enol forms of the acetone radical cation. The electron impact source was employed for the ionization of acetone, 2-pentanone, and 2-heptanone. The ionization energy was 12, 11, and 11eV respectively. Details of the instrument have been described previously in chapter IV.

The anhydrous acetone (Aldrich, , Milwaukee, WI) is leaked into the ionization source using a variable leak valve (Varian, Lexington, MA) following freeze pump-thaw. Once the keto and enol forms (m/z=58) were determined, anhydrous 2-pentanone and 2-heptanone (Aldrich) were leaked in under the same above conditions, and analyzed. All analysis was performed with the drift tube at 92K.

Computational Details

All calculations were performed with Gaussian 98 (G98).[39] Table VIII shows the results of the energy calculations using B3LYP with the 6-311 +G(d,p) and 6-31

Table VIII: Calculated energy(eV) differences (ΔE) between the keto and more stable enol, and the transition state and the enol forms of the acetone radical cations All values have been corrected with ZPEC.

Level of Theory		$CH_3OHCH_2^{+\bullet}$	TS
b3lyp	6-311 +G(d,p)	-0.372	1.677
b3lyp	6-31 +G(d',p')	-0.363	1.672
mp3	6-31 +G(d',p')	-0.483	1.664

+G(d',p') basis sets, and MP3 using the 6-311 +G(d,p) basis set. These calculations illustrate that the enol form of the acetone radical cation is markedly more stable than the keto form,[abc] which agrees with accepted experimental and theoretical calculations. Transiton state calculations were also performed under the same conditions. Due to the reproducibility of the results, and a 9.6% error with cited literature values[a], no other calculations were necessary.

The transition state of 1.6eV between the keto and enol forms is low enough to allow for ionization and interconversion upon electron impact with acetone, to form both species. The transition state is high enough to avoid interconversion due to collision with the buffer gas, due to the cooling effect in the mobility cell. This should allow the production of the enol form due to a "McLafferty rearrangement" to remain stable, and not interconvert in the mobility cell.

Results and Discussion

Figure 37 shows the arrival time distribution (ATD) for acetone and the dissociation products versus m/z. The drift cell was run at 92K in 1 torr Ar, and the acetone was ionized at 12.0eV. Two peaks are resolved, though not baseline resolution, at m/z=58. The two peaks are proposed to be the keto and enol forms of the C_3H_6O radical cation. These peaks are unable to be resolved at temperatures greater than 150K in Ar.

Collision-induced dissociation/reaction dynamic and energy resolved electron beam coupled to a quadrupole mass spectrometer experiments have shown that the keto ($CH_3COCH_3^{+*}$) and enol ($CH_3COHCH_2^{+*}$) forms exist for the acetone radical cation.

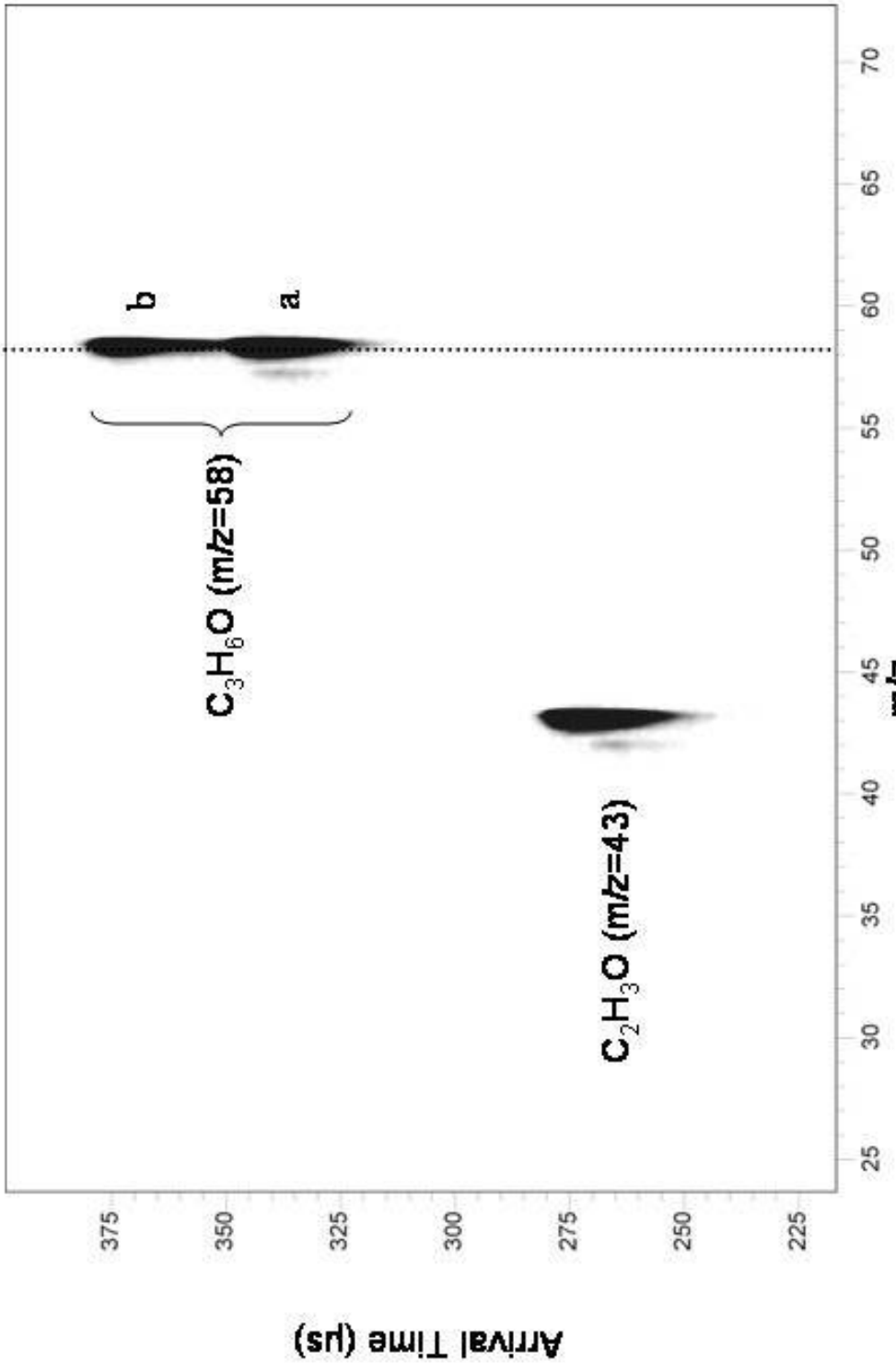

Figure 37. Ion mobility arrival time distribution versus m/z for acetone ionized at 12.0eV showing the (a) keto and (b) enol forms at m/z=58.

This gives the greatest evidence for the assigmnment of these m/z=58 peaks. The enol radial cation has also been shown both experimentally and theoretically to be the more stable isomer with a 1.6eV barrier to interconversion. This high barrier affords the ability to cool the ions with collision in the Ar buffer gas after ionization, and interconversion in the drift cell is not observed. Coalescence of the two peaks would be observed if interconversion occurred.

Using cross-section calculations and theoretical results, peak assignments were made based on the interaction of each species with the buffer gas. From the calculations, both the keto and enol forms have the same projection cross-section (~22 angstoms^2), but the dipole moment of the enol form (μ=2.5 Debye) was greater than the keto form (μ=1.6 Debye). The greater dipole moment allows for a greater dipole-induced dipole interaction with the Ar buffer gas, which causes a longer retention time for the enol form in the buffer gas. From these predictions the keto form (Figure 37 a) will elute before the enol form (Figure 37 b). The arrival time for the keto form is 343μs and the enol form is 374μs.

The "McLafferty rearrangement" predicts that the m/z=58 dissociation ion is the enol form for molecules containing an alkyl group, R-CH_2CH_2-, joined with a carbonyl group. Now that the m/z=58 peaks have been identified, it is possible to probe molecules that produce the m/z=58 to determine which isomer is the product of dissociation. Both 2-pentanone and 2-heptanone produce the m/z=58 peak, and should obey the rules for the "McLafferty rearrangement".

Figure 38 shows the dissociation product ion spectrum of mobility arrival time versus mass-to-charge for 2-pentanone ($CH_3CH_2CH_2COCH_3$). Here we see the common product ion peaks m/z=58, 57, and 43 for the ionization of 2-pentanone. Ionization was performed at 11eV and the mobility was determined in 1 torr Ar buffer gas at 92K. Only one m/z=58 peak is observed at an arrival time of 374μs. No recordable peak can be observed at 343μs. From this evidence it can be seen that the enol form is the sole product ion at m/z=58 for 2-pentanone.

2-heptanone was also analyzed at an ionization potential of 11eV in 1 torr Ar at 92K. Figure 39 shows the partial spectrum (m/z<70) of the arrival time distribution versus m/z for the product ions of 2-heptanone. Here we see the common product ion peaks m/z=71, 58, 57, and 43 for the ionization of 2-heptanone. Only one product ion at m/z=58 was observed at the arrival time of 374μs, corresponding to the enol isomer of the C_3H_6O radical cation.

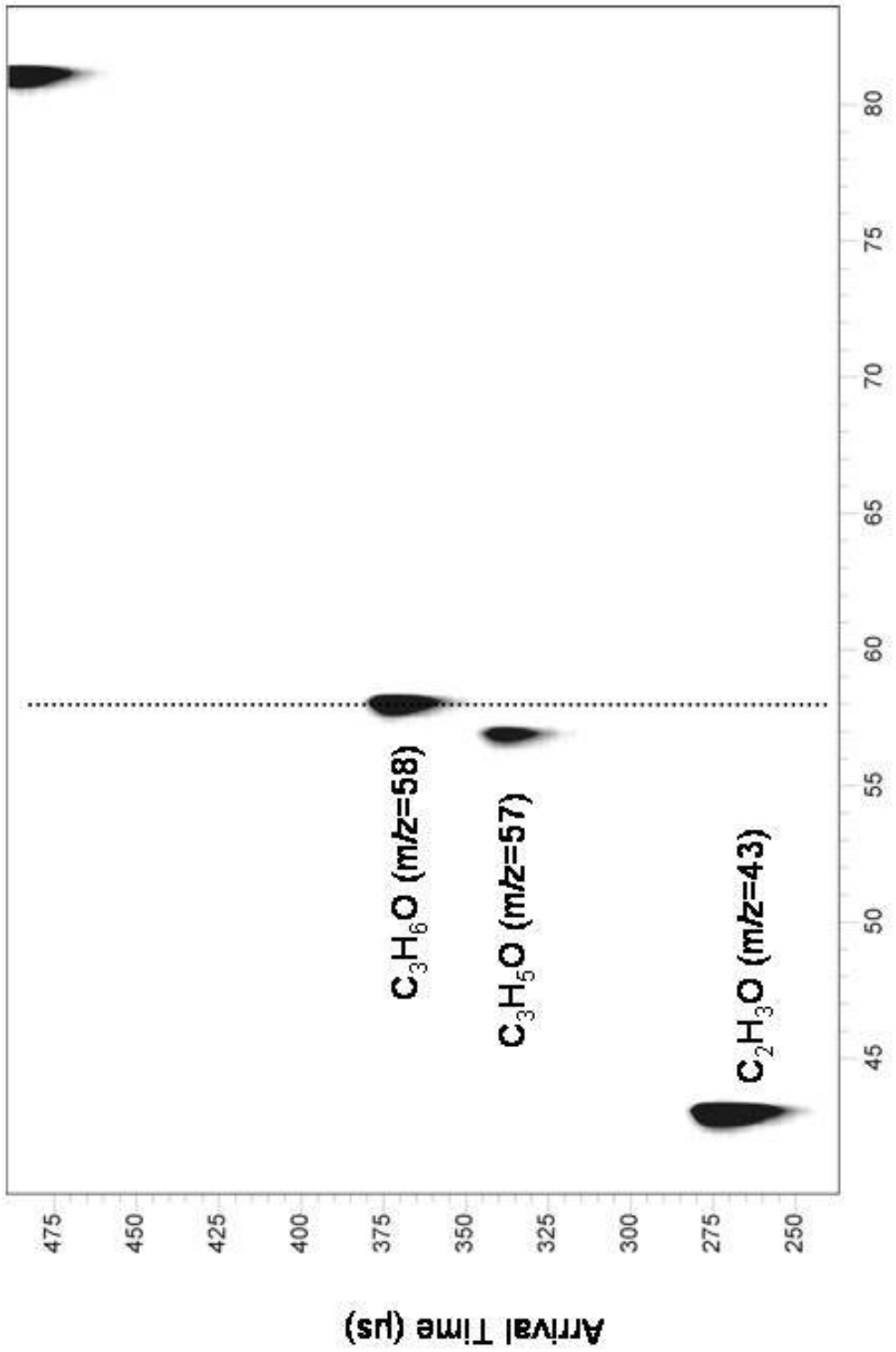

Figure 38. Ion mobility arrival time distribution versus m/z for 2-pentanone ionized at 11.0eV.

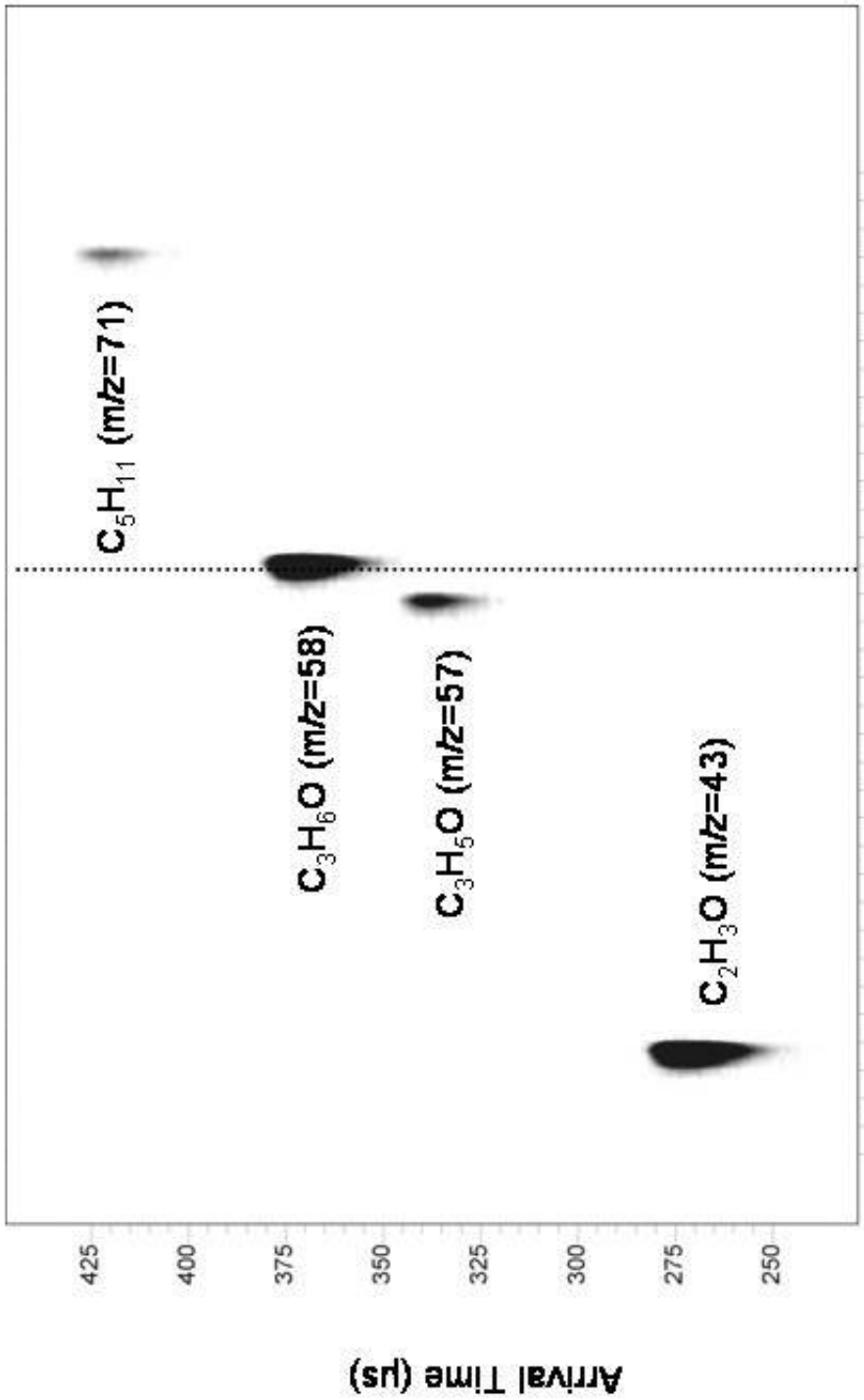

Figure 39. Segment of the ion mobility arrival time distribution versus m/z for 2-heptanone ionized at 11.0eV

CHAPTER IX

CONCLUSIONS

Resolution

The resolution equations presented here establish a framework for effecting low pressure ion mobility instrument design. As seen in equation 26, issues related to temperature, transmission, and overall length of the drift region should be taken into account. Using Wannier's relation, the calculation of diffusion can be applied to a broader range of applied fields. This gives the investigator greater flexibility to evaluate the potential resolution over a broader range of experimental conditions. Using Wannier's relation to calculate the approximate diffusion coefficient provides more accurate representation of current mobility resolution and transmission equations. For high mass analysis, we have shown that the resolution equations reduce to the low-field limit; therefore, the resolution for larger ions (*i.e.,* peptides and proteins >1000m/z) can be increased by raising the applied fields.

Programming

I have shown here the development of a radial ion trajectory program for proof of concept in the use of a periodic electrostatic field for ion mobility cell design. It was illustrated that the same principles applied to electron beam confinement can be used to simulate ion motion within a periodic field. As much as a multiple of 35 increase in ion transmission was predicted to occur over the conventional linear model. The use of a

periodic electrostatic lens array should increase ion transmission over a broad range of masses and applied electric fields.

The other program, MobCross, has been shown to be an effective projection cross-section simulation program in the analysis of amino acids and peptides. The improved speed of the program due to the use of the quaternion method has made it a good tool to complement ion mobility data.

MobCross was able to demonstrate, compared to experimental data, the charge location of the basic amino acids, lysine and arginine. With the charge site on the N-terminal instead of the side chain, a difference in the cross-section was significant to illustrate the more proper location of the proton on the amino acid. Also MobCross showed the ability, when combined with molecular mechanics calculations, to discriminate between the broad range of low energy results due to the simulated annealing process. Outliers from the combination of molecular mechanics and projection cross-section calculations can show short comings in the molecular mechanics program, or discriminate peptides that may have interesting chemistry and folding properties.

Separations

I demonstrated that ion mobility provides a powerful means to separate isobaric ions, which can be applied to the separation of conventional and distonic radical cations, and the keto and enol forms of the acetone radical cation. This provides direct evidence that ionization of methanol and methylfluoride yield two stable radical cation species in the gas phase adding to the current array of indirect experimental and theoretical results on conventional and distonic radical cation forms. This also provides direct evidence of

the existence of both the keto and enol forms as stable m/z=58 isomers of the acetone radical cation. Liquid nitrogen-cooled ion mobility spectrometry exhibits increased resolving power (through an increase in ion-neutral interactions) as well as a 3 fold increase in peak resolution when operated at 90 K. The coupling of IM and mass spectrometry provides a powerful experimental tool for ion chemists to separate isomeric ions and make it possible to explore structure specific ion-molecule reaction chemistry.

Theoretical Calculations

I have also demonstrated improved theoretical results. I showed the modified Perdew-Wang calculations give accurate results for both the methanol and methylamine. The use of this DFT method saves computational expense. I showed that the problem with the methylflouride calculations may lie in the use of single reference techniques; however, the MP4DQ do produce more correlative results to that of experimental values.

The Future

There seems to be endless possibilities for an application instrument of this nature. There is still a great many gas phase ion chemistry problems yet to be explored. Perhaps this instrumentation can resolve the questions about the m/z=78 peak once benzene has been ionized. Ring structures as opposed to chains may be easily resolved in a cooled buffer gas. Also isobaric atomic species could be separated by probing with either the interaction potential differences or charge exchange differences.

Changes could be made in the experiment to open the door even wider. Different sources, like laser ablation, MALDI, and chemical ionization could be used. Using other buffer gases, as CO_2, N_2, and CH_4 among many others, can probe different chemistry.

REFERENCES

1. Mason, E. A.; McDaniel, E. W. *Transport Properties of Ions in Gases*; Wiley: New York, NY, 1988.

2. Carr, T.W. *Plasma Chromatography*; Plenum Press: New York,NY, 1984.

3. Eiceman, G.A.; Karpas, Z. *Ion Mobility Spectrometry*; CRC Press: Boca Raton, FL, 1994.

4. Eiceman, G.A. *Trends Anal. Chem.* **2002**, 21, 259.

5. Beegle, L.W.; Kanik, I.; Matz, L.; Hill, H.H. *Anal. Chem.* **2001**, 73, 3028.

6. Clemmer, D.E.; Jarrold, M.F. *J. Mass. Spetrom.* **1997**, 32, 577.

7. Couterman, A.E.; Clemmer, D.E. *J. Am. Chem. Soc.* **2001**, 123, 1490.

8. Wu, C.; Siems, W.F.; Klasmeier, J.; Hill, H.H. *Anal. Chem.* **2000**, 72, 391.

9. Wyttenbach, T.; Kemper, P.R.; Bowers, M.T. *Int. J. Mass Spect.* **2001**, 212, 13.

10. Kooman, J.M.; Ruotolo, B.T.; Gillig, K.J.; McLean, J.A.; Kang, M.; Fuhrer, K.; Gonin, M.; Schultz, J.A.; Dunbar, K.R.; Russell, D.H. *Anal. Bioanal. Chem.* **2002**, 373, 612.

11. Ruotolo, B.T.; Verbeck, G.F.; Thomson, L.M.; Woods, A.S.; Gillig, K.J.; Russell, D.H. *J. Proteome Res.* **2002**, 1, 303.

12. Stone, E.G.; Gillig, K.J.; Ruotolo, B.T.; Russell, D.H. *Int. J. Mass Spect.* **2001**, 212, 519.

13. Harland, P.W.; McIntosh, B.J.; Simpson, R.W.; Thomas, N.R. *J. Chem. Soc. Faraday Trans. 2* **1986**, 82, 2039.

14. Helm, H.; Elford, M.T. *J. Phys. B* **1977,** 10, 983.

15. Koizumi, T.; Kobayashi, N.; Kaneko, Y. *J. Phys. Soc. Jap.* **1980**, 48, 1678.

16. Parent, D.C.; Bowers, M.T. *J. Chem. Phys.* **1981**, 60, 257.

17. McDaniel, E.W.; Moseley, J.T. *Phys. Rev. A* **1971**, 3, 1040**.**

18. Wannier, G.H. *Bell Sys. Tech. J.* **1953**, Jan, 171.

19. Mesleh, M.F.; Hunter, J.M.; Shvartsburg, A.A.; Schatz, G.C.; Jarrold, M.F. *J. Phys. Chem.* **1996**, 100, 16082.

20. Chapman, S.; Cowling, T.G. *The Mathematical Theory of Non-Uniform Gases*; Cambridge Press: London, 1958.

21. Su, T.; Su, E.C.F.; Bowers, M.T. *Int. J. Mass Spectrom. Ion Phys.* **1978**, 28, 285.

22. Karasek, F.W. *Anal Chem* **1974**, 46, 710A.

23. Carr, T.W. *Plasma Chromatography*; Plenum Press: New York, NY, 1984.

24. Eiceman, G.A.; Karapas, Z. *Ion Mobility Spectrometry*; CRC Press:Boca Raton, FL, 1994.

25. Kemper, P.R.; Bowers, M.T. *J Phys Chem* **1991**, 95 ,5134.

26. Clemmer, D.E; Jarrold, M.F. *J Mass Spectrosc* **1997,** 32*,*577.

27. Couterman, A.E.; Clemmer, D.E. *J Am Chem Soc* **2001**, 123*,* 1490.

28. Wu, C.; Siems, W.F.; Klasmeier, J.; Hill, H.H. *Anal Chem* **2000**, 72*,* 391.

29. Wyttenbach, T.; Kemper, P.R.; Bowers, M.T. *Int J Mass Spect* **2001,** 212*,* 13.

30. Kooman, J.M.; Ruotolo, B.T.; Gillig, K.J.; McLean, J.A.; Kang, M.; Fuhrer, K.; Gonin, M.; Schultz, J.A.; Dunbar, K.R.; Russell, D.H. *Submitted to J Anal Bioanal Chem*.

31. Ruotolo, B.T.; Verbeck, G.F.; Thomson, L.M.; Woods, A.S.; Gillig, K.J.; Russell, D.H. *J Proteomics Res*, **2002**, 1, 303.

32. Stone, E.G.; Gillig, K.J.; Ruotolo, B.T.; Russell, D.H. *Int J Mass Spect*. **2001**, 212, 519.

33. Asbury, G.R.; Hill, H.H. *Anal Chem* **2000,** 72*,* 580.

34. Giddings, J.C. *Anal Chem.***1984**, 56, 1258A.

35. Wannier, G.H. *Bell System Tech. J*. **1953,** 32, 170.

36. McDaniel, E.W.; Moseley, J.T. *Phys. Rev. A*. **1971,** 3, 1040.

37. Revercomb, H.E.; Mason, E.A. *Anal. Chem*. **1975**, 47, 970.

38. Watts, P.; Wilder, A. *Int. J. Mass Spect*. **1992**, 112*,* 179.

39. Rokushika, S.; Hatano, H.; Baim, M.A.; Hill, H.H. *Anal. Chem*. **1985,** 57, 1902.

40. Ashbury, G.R.; Hill, H.H. *J. Microcolumn Sep*. **2000,** 12*,* 172.

41. Crank, J. *The Mathematics of Diffusion*, Oxford: New York, NY, 1975.

42. Kemper, P.R.; Bowers, M.T. *J. Am. Soc. Mass Spectrom*. **1990**, 1, 197.

43. Gillig, K.J.; Ruotolo, B.T.; Verbeck, G.F.; Stone, E.G.; Russell, D.H. *Rev. Sci. Inst.*, **Submittd**.

44. Verbeck, G.F.; Russell, D.H. *Eur. J. Mass Spect.* **2003**, 9, *579.*

45. Javahery, G.; Thomson, B. *J. Am. Soc. Mass Spect*. **1997,** 8 , 697.

46. Bluhm, B.K.; Gillig, K.J.; Russell, D.H. *Rev. Sci. Inst*. **2000**, 71*,* 4078.

47. Karger, B.L.; Snyder, L.R.; Horvath, C. *An Introduction to Separation Science*; Wiley: New York, NY, 1973.

48. Courant, E.D.; Livingston, M.S.; Snyder, H.S. *Phys. Rev.* **1952**, 98, 1190.

49. Clogston, A.M.; Heffner, H. *J. Appl. Phys.* **1954**, 25, 436.

50. Tien, P.K. *J. Appl. Phys.* **1954**, 25, 1281.

51. Szilagyi, M. *Proc. 5th Internat. Congress on Microwave Tubes* **1965**, 339.

52. Szilagyi, M. *Radio Eng. Electron. Phys.* **1966**, 11, 751.

53. Borghi, R.P.; Dunn, D.A. *J. Appl. Phys.* **1963**, 34, 692.

54. Szilagyi, M. *Electron and Ion Optics*; Plenum Press,: New York, NY, 1988**.**

55. Humphries, S. *Principles of Charged Particle Acceleration*; J. Wiley: New York, NY, 1986.

56. Wollnik, H. *Optics of Charged Particles*; Academic Press: New York, NY, 1987**.**

57. Zworykin, V.K.; Morton, G.A.; Ramberg, E.G. *Electron Optics and the Electron Microscope*; J. Wiley: New York, NY, 1945**.**

58. Mason, E.A.; O'Hara H., Smith, F.J. *J. Phys. B: Atom. Molec. Phys.* **1972**, 5, 169.

59. Lin, S.L.; Bardsley, J.N. *J. Chem. Phys.* **1977**, 66, 435.

60. Harland, P.W.; McIntosh, B.J.; Simpson, R.W.; Thomas, N.R. *J. Chem. Soc., Faraday Trans.* **1986**, 82, 2039.

61. Gau, Y.; Guo, S. *Jpn. J. Appl. Phys.* **1997**, 36, 943.

62. Berant, Z.; Shahai, O.; Karpas, Z. *J. Phys. Chem.* **1991**, 95, 7534.

63. Shvartsburg, A.A.; Jarrold, M.F. *Chem. Phys. Lett.* **1996**, 261, 86.

64. von Helden, G.; Hsu, M.; Gotts, N.; Bowers, M.T. *J. Phys. Chem.* **1993**, 97, 8182.

65. von Helden, G. *Investigations of the Structure and Energetics of Gas Phase Cluster Ions using Ion Chromatography*, Ph.D. dissertation, University of California, Santa Barbara, 1994.

66. Frenkel, D.; Smit, B. *Understanding Molecular Simulations*; Academic Press: San Diego, CA, 1996.

67. Vesely, F. J. *J. Comp. Phys.* **1982**, 47, 291.

68. Beegle, L.W.; Kanik, I; Matz, L.; Hill, H.H. *Anal. Chem.* **2001**, 73, 3028.

69. Mosier, P.D.; Counterman, A.E.; Jurs, P.C.; Clemmer, D.E. *Anal. Chem.* **2002**, 74, 1360.

70. Bowers, M.T. *Gas Phase Ion Chemistry*; Academic Press: San Diego, CA, 1979.

71. Russell, D.H. *Gas Phase Inorganic Chemistry*; Plenum Press: New York, NY, 1989**.**

72. Blum, W.; Rolandi, L. *Particle Detection with Drift Chambers*; Springer-Verlag: Berlin, 1994.

73. Ng, C.; Baer, T.; Pervis, I. *Unimolecular and Bimolecular Ion-Molecule Reaction Dynamics*; John Wiley & Sons: New York, NY, 1994.

74. Parent, D.C.; Bowers, M.T. *Chem. Phys.* **1981**, 60, 257.

75. Bass, L.; Su, T.; Bowers, M.T. *Int. J. Mass Spectrom. Ion Phys.* **1978**, 28, 389.

76. Liu, W.F.; Conway, D.C. *J. Chem. Phys.* **1975**, 62, 3070.

77. Viehland, L.A.; Mason, E.A. *At. Data Nuc. Data Tab.* **1995**, 60, 37.

78. Ast, T.; Terwilliger, D.T.; Beynon, B.H.; Cooks R.G. *J. Chem. Phys.* **1975**, 62, 3855.

79. Hasted, J.B.; Hussain, M. *Proc. Phys. Soc.* **1964**, 83, 911.

80. Hasted, J.B.; Phil, D.; Smith, R.A. *Proc. Roy. Soc.* **1956**, A235, 354.

81. Helm, H. *J. Phys. B: Atom. Molec. Phys.* **1976**, 9, 2931.

82. Gorzdanov, T.P.; Janev, R.K.; Lazur, V.Y. *Phys. Scr.* **1985**, 32, 64.

83. Okuno, K.; Koizumi, T.; Kaneko, Y. *Phys. Rev. Lett.* **1978**, 40, 1708.

84. Adams, N.G.; Smith, D.; Alge, E. *J. Phys. B: Atom. Molec. Phys.* **1980**, 13, 3235.

85. Bluhm, B.K.; North, S.; Russell, D.H. *J. Chem. Phys.* **2001**, 14, 1709.

86. Koizumi, T.; Okuno, K.; Kobayashi, N.; Kaneko, Y. *J. Phys. Soc. Jap.* **1982**, 51, 2650.

87. Koizumi, T.; Tsurugai, T.; Ogawa, I. *J. Phys. Soc. Jap.* **1987**, 56, 17.

88. Gidden, J.; Kemper, P.R.; Shammel, E.; Fee, D.P.; Anderson, S.; Bowers, M.T. *Int. J. Mass Spectrom.* **2003**, 222, 63.

89. Ma, N.L.; Smith, B.J.; Radom, L. *J. Phys. Chem.* **1992**, 96, 5804.

90. Bouma, W.J.; Nobes, R.H.; Radom, L. *J. Am. Chem. Soc.* **1982**, 104, 2929.

91. Ma, N.L.; Smith, B.J.; Pople, J.A.; Radom, L. *J. Am. Chem. Soc.* **1991**, 113, 7903.

92. Guilhaus, M.; Shelby, D.; Mlynski, V. *Mass Spectrom. Rev.* **2000**, 19, 65.

93. Frisch, M.J.; Trucks, G.W.; Schlegel, H.B.; Scuseria, G.E.; Robb, M.A.; Cheeseman, J.R.; Zakrzewski, V.G.; Montgomery, J.A.; Stratmann, R.E.; Burant, J.C.; Dapprich, S.; Millam, J.M.; Daniels, A.D.; Kudin, K.N.; Strain, M.C.; Farkas, O; Tomasi, J.; Barone, V.; Cossi, M.; Cammi, R.; Mennucci, B.; Pomelli, C.; Adamo, C; Clifford, S.; Ochterski, J.; Petersson, G.A.; Ayala, P.Y.; Cui, Q.; Morokuma, K.; Salvador, P.; Dannenberg, J.J.; Malick, D.K.; Rabuck, A.D.; Raghavachari, K.; Foresman, J.B.; Cioslowski, J.; Ortiz, J.V.; Baboul, A.G.; Stefanov, B.B.; Liu, G.; Liashenko, A.; Piskorz, P.; Komaromi, I.; Gomperts, R.; Martin, R.L.; Fox, D.J.; Keith, T.; Al-Laham, M.A.; Peng, C.Y.; Nanayakkara, A.; Challacombe, M.; Gill, P.M.W.; Johnson, B.; Chen, W.; Wong, M.W.; Andres, J.L.; Gonzalez, C.; Head-Gordon, M.; Replogle, E.S.; Pople, J.A.; Gaussian 98 [Software]; Gaussian, Inc.; Pittsburgh, PA, 2001.

94. Hegarty, D.; Robb, M.A. *Mol. Phys.* **1979**, 38, 1795.

95. Eade, R.H.E; Robb, M.A. *Chem. Phys. Lett.* **1981**, 83, 362.

96. Kuechle, W.; Dolg, M.; Stoll, H.; Preuss, H. *Mol. Phys.* **1991**, 74, 1245.

97. Møller, C.; Plesset, M.S. *Phys. Rev.* **1986**, 46, 618.

98. Pople, J.A.; Binkley, J.S.; Seeger, R. *Int. J. Quantum Chem.* **1976**, S10, 1.

99. Krishnan, R.; Binkley, J.S.; Seeger, R.; Pople, J.A. *J. Chem. Phys.* **1980**, 72, 650.

100. Verbeck, G.F.; Ruotolo, B.T.; Gillig, K.J.; Russell, D.H. *J. Am. Soc. Mass Spectrom.* **2004,** 15, 1320.

101. Bowers, M.T.; Kemper, P.R.; von Helden, G.; van Koppen, P.A.M. *Science* **1993**, 260, 1446.

102. Verbeck, G.F.; Webster, C.E.; Hall, M.B.;Russell, D.H. *Int. J. Mass Spectrom.* **Submitted.**

103. Hammerum, S. *Mass Spectrom. Rev.* **1988**, 7, 123.

104. Holmes, J.L.; Lossing, F.P.; Terlouw, J.K.; Burgers, P.C. *J. Am. Chem. Soc.* **1982,** 104, 2931.

105. Holmes, J.L.; Lossing, F.P.; Terlouw, J.K.; Burgers, P.C. *Can. J. Chem.* **1983,** 61, 2305.

106. Gauld, J.W.; Radom, L. *J. Phys. Chem.* **1994**, 98, 777.

107. Fridgen, T.D.; Parnis, J.M. *Int. J. Mass Spectrom.* **1999**, 190, 181.

108. Lynch, B.J.; Fast, P.L.; Harris, M.; Truhlar, D.G. *J. Phys. Chem. A* **2000**, 104, 4811.

109. Lynch, B.J.; Truhlar, D.G. *J. Phys. Chem. A* **2001,** 105, 2936.

110. Becke, A. D. *J. Chem. Phys.* **1993**, 98, 5648.

111. Lee, C.; Yang, W.; Parr, R. G. *Phys. Rev. B*, **1988**, 37, 785.

112. Parr, R. G.; Yang, W. *Density Functional Theory of Atoms and Molecules*; Oxford University Press: New York, NY, 1989.

113. Ditchfield, R.; Hehre, W. J. ; Pople, J. A. *J. Chem. Phys.* **1971**, 54, 724; Hehre, W. J.; Ditchfield, R., Pople, J. A. *J. Chem. Phys.* **1972**, 56, 2257; Hariharan, P.C.; Pople, J.A. *Theoret. Chimica Acta* **1973**, 28, 213; Francl, M. M. Pietro, W. J.; Hehre, W. J.; Binkley, J. S.; Gordon, M. S.; DeFrees, D.J.; Pople, J. A. *J. Chem. Phys.* **1982**, 77, 3654.

114. Petersson, G. A.; Al-Laham, M. A. *J. Chem. Phys.* **1991**, 94, 6081; Petersson, G. A.; Bennett, A.; Tensfeldt, T. G.; Al-Laham, M. A.; Shirley, W. A.; Mantzaris, J. *J. Chem. Phys.* **1988**, 89, 2193. P.C. Hariharan and J.A. Pople, *Theoret. Chimica Acta* **1973**, 28, 213; Francl, M.M.; Petro, W.J.; Hehre, W.J.; Binkley, J.S.; Gordon, M.S.; DeFrees, D.J.; Pople, J.A. *J. Chem. Phys.* **1982**, 77, 3654; T. Clark, J. Chandrasekhar, P.v.R. Schleyer, *J. Comp. Chem.* **1983**, 4, 294; Krishnam, R.; Binkley, J.S.; Seeger, R.; Pople, J.A. *J. Chem. Phys.* **1980**, 72, 650; Gill, P.M.W.; Johnson, B.G.; Pople, J.A.; Frisch, M. J. *Chem. Phys. Lett.* **1992**, 197, 499.

115. Nicklass, A.; Dolg, M.; Stoll, H.; Preuss, H. *J. Chem. Phys.* **1995**, 102, 8942

116. Werner, H.J. *http://www.theochem.uni-stuttgart.de/pseudopotentials*; Universität Stuttgart: Stuttgart, 2003.

117. McLafferty, F.W. *Anal. Chem.* **1959**, 31, 82.

118. Budzikiewicz, H.; Djerassi, C.; Williams, D.H. *Mass Spectrometry of Organic Compounds;* Holden-Day, Inc.: San Francisco, CA, 1967.

119. McLafferty, F.W.; Turecek, F. *Interpretation of Mass Spectra* University Science Books: Sausalito, CA, 1993.

120. Diekman, J.; MacLoed, J.K.; Djerassi, C.; Baldeschwieler, J.D. *J. Am. Chem. Soc.* **1969**, 91, 2069.

121. Beynon, J.H.; Caprioli, R.M.; Cooks, R.G. *Org. Mass Spectrom.* **1974**, 9, 1.

122. Beauchamp, J.L. *Ann. Rev. Phys. Chem.* **1971**, 22, 527.

123. McLafferty, F.W.; Pike, W.T. *J. Am. Chem. Soc.* **1967**, 89, 5953.

124. McAdoo, D.J.; McLafferty, F.W.; Parks, T.E. *J. Am. Chem. Soc.* **1972**, 94, 1601.

125. Beynon, J.H.; Caprioli, R.M.; Channon, T. *Org. Mass Spectrom.* **1971**, 5, 967.

126. Eadon, G.; Djerassi, C.; Beynon, J.H.; Caprioli, R.M. *Org. Mass Spectrom.* **1971**, 5, 917.

127. Eadon, G.; Diekman, J.; Djerassi, C. *J. Am. Chem. Soc.* **1970**, 92, 6205.

128. Holmes, J.L.; Lossing, F.P. *J. Am. Chem. Soc.* **1980**, 102, 1591.

129. Holmes, J.L.; Lossing, F.P. *J. Am. Chem. Soc.* **1982**, 104, 2648.

130. Qian, K.; Shukla, A.; Howard, S.; Anderson, S.; Futrell, J. *J. Phys. Chem.* **1989**, 93, 3889.

131. Qian, K.; Shukla, A.; Futrell, J. *J. Chem. Phys.* **1990**, 92, 5988.

132. Trikoupis, M.A.; Burgers, P.C.; Ruttink, P.J.A.; Terlouw, J.K. *Int. J. Mas. Spectrom.* **2002**, 217, 97.

APPENDIX A

PERIODIC FOCUSING PROGRAM

```
Imports System.Drawing
Imports System.Drawing.Drawing2D
Imports System.Drawing.Imaging
Imports System.Drawing.Text
Imports System.IO
Imports System.Math

Public Class IonMotionMain
    Inherits System.Windows.Forms.Form

    Dim temp, press, mob, numden As Single
    Dim kb, coul, avogad, gasconst As Single
    Dim ionrad, buffrad, lambda As Single
    Dim numcoll, celllength As Single
    Dim posr, posz As Single
    Dim Eo, Emax, Eoff, ringgap As Single
    Dim i, j, k, m, n, p As Integer
    Dim Em, timestep As Single
    Dim bz, br, Ez, Erad, az, ar As Single
    Dim diffe, diffwa, diffwr, transcal As Single
    Dim buffmass, ionmass As Single
    Dim Esi As Single
    Dim numstartions As Single
    Dim driftt, driftv, ringID As Single
    Dim diffrad, radv As Single
    Dim rpos(100000) As Single
    Dim xpos, ypos As Single
    Dim xpoint, ypoint As Single
    Dim rndC, maxC, rndtheta As Single
    Dim exitrad, posrint As Single
    Dim posrscat, posrstep As Single
    Dim posrfin(100000), posrlinfin(100000) As Single
    Dim numcounts As Long
    Dim count(100000), countper(100000) As Integer
    Dim highn As Integer
```

```
#Region " Windows Form Designer generated code "

    Public Sub New()
        MyBase.New()

        'This call is required by the Windows Form Designer.
        InitializeComponent()

        'Add any initialization after the InitializeComponent() call

    End Sub

    'Form overrides dispose to clean up the component list.
    Protected Overloads Overrides Sub Dispose(ByVal disposing As Boolean)
        If disposing Then
            If Not (components Is Nothing) Then
                components.Dispose()
            End If
        End If
        MyBase.Dispose(disposing)
    End Sub


    Private Sub MenuItem3_Click(ByVal sender As System.Object, ByVal e As
System.EventArgs) Handles MenuItem3.Click
        End
    End Sub

    Private Sub MenuItem10_Click(ByVal sender As System.Object, ByVal e As
System.EventArgs) Handles MenuItem10.Click

        FileOpen(1, "c:\download\ionmotion.txt", OpenMode.Output)
        'setup pic area
        Dim maxwidth, maxheight As Single
        maxwidth = picView.Width
        maxheight = picView.Height
        ringID = txtID.Text
        Dim g As Graphics
        Dim h As Graphics
        g = picView.CreateGraphics
        h = picView2.CreateGraphics
        g.Clear(Color.LightGray)
        h.Clear(Color.LightGray)
```

```
        Dim myPen1 As New Pen(Color.Magenta)
        Dim myPen2 As New Pen(Color.Red)
        Dim myPen3 As New Pen(Color.Blue)


        'set up drift cell conditions
        numcounts = 10000
        press = txtPressure.Text
        temp = txtTemp.Text
        mob = txtRedmob.Text * 760 / press * temp / 273.15 / 10000
        Esi = txtEo.Text * 100
        celllength = txtLength.Text / 100
        driftv = mob * Esi
        driftt = celllength / driftv
        buffmass = txtBuffmass.Text / 1000 / avogad
        ionmass = txtIonmass.Text / 1000 / avogad
        buffrad = 0.00000000012
        ionrad = txtIonRad.Text * 0.0000000001
        numden = press * avogad / (gasconst * temp)
        lambda = 1 / (1.414 * 3.14159 * numden * (ionrad + buffrad) ^ 2)
        numcoll = celllength / lambda


        'calculate the ion distribution due to diffusion
        txtDriftt.Text = driftt
        exitrad = txtApt.Text
        diffe = kb * temp * mob / coul
        diffwa = diffe + buffmass / 3 * ((ionmass + 3.2 * buffmass) / (ionmass + 1.908 *
buffmass)) * Esi ^ 2 * mob ^ 3 / coul
        diffwr = diffe + buffmass / 3 * ((ionmass + buffmass) / (ionmass + 1.908 *
buffmass)) * Esi ^ 2 * mob ^ 3 / coul
        transcal = 100 * (1 - (Exp(-(exitrad ^ 2) / (4 * diffwr * driftt))))
        txtTranscal.Text = transcal

        'find max value of C
        maxC = 1 / (Sqrt(3.14159 * diffwr * driftt)) * Exp(-(0.00000000001 ^ 2) / 4 *
diffwr * driftt)
        'perform distribution
        i = 1
        k = 0
        m = 0
        Do Until i = numcounts + 1
            rndC = Rnd() * maxC
            rndtheta = Rnd() * 2 * 3.14159265
```

```
        rpos(i) = Sqrt(4 * diffwr * driftt * Log(1 / (rndC * Sqrt(3.14159 * diffwr *
driftt))))
        xpos = rpos(i) * Cos(rndtheta)
        xpoint = xpos * 100 / ringID + 100
        ypos = rpos(i) * Sin(rndtheta)
        ypoint = ypos * 100 / ringID + 100
        If rpos(i) > ringID Then
           g.DrawEllipse(myPen2, xpoint, ypoint, 1, 1)
           k = k + 1
        ElseIf rpos(i) < exitrad Then
           g.DrawEllipse(myPen1, xpoint, ypoint, 1, 1)
           m = m + 1
        Else
           g.DrawEllipse(myPen3, xpoint, ypoint, 1, 1)
        End If
        i = i + 1
     Loop
     txtTranssim.Text = m / 10000 * 100
     txtLost.Text = k / 10000 * 100

     'Simulation of Periodic


     'calculate acceleration in x,y, and z directions
     Eo = txtEo.Text
     Em = txtEamp.Text
     Eoff = txtEoffset.Text
     ringgap = txtRingSpace.Text
     timestep = 0.0000001
     k = 0
     m = 0
     Do Until j = numcounts + 1
        posr = rpos(j)
        posrstep = rpos(j) * (driftv * timestep) / celllength
        posz = 0
        Do Until posz > celllength * 100

           bz = Sin(Eoff + 2 * 3.14159 * posz / ringgap)
           br = -Cos(Eoff + 2 * 3.14159 * posz / ringgap)
           Ez = Eo + Em * bz + posr ^ 2 * Em * 3.14159 ^ 2 / (ringgap ^ 2) * bz + posr ^
4 * Em * 3.14159 ^ 4 / (4 * ringgap ^ 4) * bz
           Erad = posr * Em * 3.14159 / ringgap * br + posr ^ 3 * Em * 3.14159 ^ 3 / (2
* ringgap ^ 3) * br
           az = Ez * 100 * coul / ionmass
```

```
            ar = Erad * 100 * coul / ionmass
            posrscat = (Rnd() - 0.5) * 1 / numcounts
            posz = posz + driftv * timestep * 100
            posr = posr + 0.5 * ar * timestep ^ 2 + posrscat
            posr = Abs(posr)

        Loop
        rndtheta = Rnd() * 2 * 3.14159265
        xpos = posr * Cos(rndtheta)
        xpoint = xpos * 100 / ringID + 100
        ypos = posr * Sin(rndtheta)
        ypoint = ypos * 100 / ringID + 100
        If posr > ringID Then
            h.DrawEllipse(myPen2, xpoint, ypoint, 1, 1)
            k = k + 1
        ElseIf posr < exitrad Then
            h.DrawEllipse(myPen1, xpoint, ypoint, 1, 1)
            m = m + 1
        Else
            h.DrawEllipse(myPen3, xpoint, ypoint, 1, 1)
        End If

        'record the distribution profile for the radial values
        n = 1
        Do
            If rpos(j) < n * 0.0001 Then
                count(n) = count(n) + 1
                If n > highn Then
                    highn = n
                End If
                GoTo record
            End If
            n = n + 1
        Loop
record:
        p = 1
        Do
            If posr < p * 0.0001 Then
                countper(p) = countper(p) + 1
                If p > highn Then
                    highn = p
                End If
                GoTo record2
            End If
```

```
            p = p + 1
        Loop
record2:
        'WriteLine(1, rpos(j), posr)
        j = j + 1
    Loop

    WriteLine(1, highn)
    n = 1
    Do Until n = highn + 1
        WriteLine(1, count(n), countper(n))
        n = n + 1
    Loop

    txtTranssimp.Text = m / 10000 * 100
    txtLostp.Text = k / 10000 * 100
    FileClose(1)


End Sub

Private Sub IonMotionMain_Load(ByVal sender As System.Object, ByVal e As
System.EventArgs) Handles MyBase.Load

    kb = 1.380662E-23
    coul = 1.6022E-19
    avogad = 6.022E+23
    gasconst = 0.062363
    Randomize()

End Sub


End Class
```

APPENDIX B

MOBCROSS PROGRAM

```
Imports System.Drawing
Imports System.Drawing.Drawing2D
Imports System.Drawing.Imaging
Imports System.Drawing.Text
Imports System.IO
Imports System.Math

Public Class frmMain
    Inherits System.Windows.Forms.Form
    Dim buffgas As Integer
    Dim precision As Single
    Dim fileout As String
    Dim cartfilename As String
    Dim i, j, k, m, n As Integer
    Dim atomnum(5000), atomicnum(5000), atomtype(5000) As Integer
    Dim xcoord(5000), ycoord(5000), zcoord(5000) As Single
    Dim numatoms As Integer
    Dim amu(5000), atomicradii(5000) As Single
    Dim totalmass As Single
    Dim Response As DialogResult
    Dim xcm, ycm, zcm As Single
    Dim xcenter, ycenter, zcenter As Single
    Dim Rad(5000) As Single
    Dim maxrad, bufradius, bufmass As Single
    Dim g As Graphics
    Dim maxwidth As Integer
    Dim maxheight As Integer
    Dim areaPen As New Pen(Color.DarkSalmon)
    Dim atomPen(5000) As Pen
    Dim pen1 As New Pen(Color.Black)
    Dim pen2 As New Pen(Color.Green)
    Dim pen3 As New Pen(Color.Blue)
    Dim pen4 As New Pen(Color.Red)
    Dim pen5 As New Pen(Color.Violet)
    Dim pen6 As New Pen(Color.Orange)
    Dim pen7 As New Pen(Color.Black)
    Dim pen8 As New Pen(Color.White)
    Dim atomcolor As Color
    Dim atomoutline As Color
```

```
    Dim xpos, ypos As Single
    Dim atomleft, atomright, atomtop, atombottom As Integer
    Dim atomradius As Single
    Dim z(4) As Single
    Dim S1, S2 As Single
    Dim q1, q2, q3, q4 As Single
    Dim Lambda As Single
    Dim quant(3, 3) As Single
    Dim orgx, orgy, orgz As Single
    Dim orgxc, orgyc, orgzc As Single
    Dim xrnd, yrnd As Single
    Dim radialval, rsqr, prodxy As Single
    Dim numhits, numrot As Integer
    Dim totalarea, molarea, atomden As Single
    Dim line As String

    Private Sub MenuItem6_Click(ByVal sender As System.Object, ByVal e As
System.EventArgs) Handles MenuItem6.Click

        End

    End Sub

    Private Sub MenuItem5_Click(ByVal sender As System.Object, ByVal e As
System.EventArgs) Handles MenuItem5.Click

        Dim g As Graphics
        Dim maxwidth As Integer
        Dim maxheight As Integer
        maxwidth = Width
        maxheight = Height
        g = Me.CreateGraphics
        Dim myPen As New Pen(Color.Red)
        myPen.Width = 1
        g.DrawLine(myPen, 1, 1, maxwidth, maxheight)

    End Sub

    Private Sub Input_Conditions()

        'Read in Run Parameters
        FileOpen(1, "c:\windows\system\conditions.ini", OpenMode.Input)
        Input(1, buffgas)
        Input(1, precision)
```

```
        Input(1, fileout)
        FileClose(1)

        If buffgas = 0 Then
            bufradius = 0.0
            bufmass = 0.0
        ElseIf buffgas = 1 Then
            bufradius = 1.22
            bufmass = 4.003
        ElseIf buffgas = 2 Then
            bufradius = 1.6
            bufmass = 20.18
        ElseIf buffgas = 3 Then
            bufradius = 1.91
            bufmass = 39.95
        ElseIf buffgas = 4 Then
            bufradius = 1.98
            bufmass = 83.8
        ElseIf buffgas = 5 Then
            bufradius = 2.18
            bufmass = 131.3
        ElseIf buffgas = 6 Then
            bufradius = 2.2
            bufmass = 28.02
        ElseIf buffgas = 7 Then
            bufradius = 2.7
            bufmass = 16.03
        End If
        'reset variables
        numatoms = 0
        totalmass = 0

    End Sub

    Private Sub MenuItem7_Click(ByVal sender As System.Object, ByVal e As
System.EventArgs) Handles MenuItem7.Click

        Call Input_Conditions()

        With OpenCartDialog
            .CheckFileExists = True
            .ShowReadOnly = False
            .Filter = "All Files|*.*|Text Files|*.txt"
            .FilterIndex = 2
```

```
        If .ShowDialog = DialogResult.OK Then
           cartfilename = OpenCartDialog.FileName
        Else : GoTo Cancel_Event
        End If
      End With

      FileOpen(1, cartfilename, OpenMode.Input)

      i = 1
      Do   ' Loop until end of file.
        Input(1, atomnum(i))
        Input(1, atomicnum(i))
        Input(1, atomtype(i))
        Input(1, xcoord(i))
        Input(1, ycoord(i))
        Input(1, zcoord(i))

        i = i + 1 ' Print to the output window.
      Loop Until EOF(1)
      FileClose(1)
      numatoms = i - 1

      Call Mol_Info()
      Call Find_CM()
      Call Refresh_Graphic()
Cancel_Event:
   End Sub

   Private Sub Find_CM()

      'Finds the center of mass and center of the molecule
      'and adjusts the coordinate system to center of mass

      i = 1
      xcm = 0
      ycm = 0
      zcm = 0
      xcenter = 0
      ycenter = 0
      zcenter = 0

      Do Until i = numatoms + 1

        xcm = xcm + xcoord(i) * amu(i)
```

```
        ycm = ycm + ycoord(i) * amu(i)
        zcm = zcm + zcoord(i) * amu(i)
        xcenter = xcenter + xcoord(i)
        ycenter = ycenter + ycoord(i)
        zcenter = zcenter + zcoord(i)
        i = i + 1

    Loop

    xcm = xcm / totalmass
    ycm = ycm / totalmass
    zcm = zcm / totalmass
    xcenter = xcenter / numatoms - xcm
    ycenter = ycenter / numatoms - ycm
    zcenter = zcenter / numatoms - zcm


    i = 1
    Do Until i = numatoms + 1

        xcoord(i) = xcoord(i) - xcm
        ycoord(i) = ycoord(i) - ycm
        zcoord(i) = zcoord(i) - zcm
        i = i + 1

    Loop

    j = 1
    maxrad = 0
    'find max radius of sphere in order to produce single circle area about the molecule
    Do Until j = numatoms + 1

        Rad(j) = Sqrt(xcoord(j) ^ 2 + ycoord(j) ^ 2 + zcoord(j) ^ 2) + atomicradii(j) +
bufradius

        If maxrad <= Rad(j) Then
            maxrad = Rad(j)
        Else
            maxrad = maxrad
        End If

        j = j + 1

    Loop
```

```
    End Sub

    Private Sub Rotate_Mol()

find:
        i = 1
        Do Until i = 5

            Randomize()
            z(i) = (2 * Rnd() - 1)
            i = i + 1
        Loop

        S1 = z(1) ^ 2 + z(2) ^ 2
        S2 = z(3) ^ 2 + z(4) ^ 2
        If S1 >= 1 Then
            GoTo find
        Else
            S1 = S1
        End If

        If S2 >= 1 Then
            GoTo find
        Else
            S2 = S2
        End If

        q1 = z(1)
        q2 = z(2)
        q3 = z(3) * Sqrt((1 - S1) / S2)
        q4 = z(4) * Sqrt((1 - S1) / S2)
        Lambda = q1 ^ 2 + q2 ^ 2 + q3 ^ 2 + q4 ^ 2

        quant(1, 1) = q1 ^ 2 + q2 ^ 2 - q3 ^ 2 - q4 ^ 2
        quant(2, 1) = 2 * (q2 * q3 - q1 * q4)
        quant(3, 1) = 2 * (q2 * q4 + q1 * q3)
        quant(1, 2) = 2 * (q2 * q3 + q1 * q4)
        quant(2, 2) = q1 ^ 2 - q2 ^ 2 + q3 ^ 2 - q4 ^ 2
        quant(3, 2) = 2 * (q3 * q4 - q1 * q2)
        quant(1, 3) = 2 * (q2 * q4 - q1 * q3)
        quant(2, 3) = 2 * (q3 * q4 + q1 * q2)
        quant(3, 3) = q1 ^ 2 - q2 ^ 2 - q3 ^ 2 + q4 ^ 2
```

```
        k = 1
        Do Until k = numatoms + 1

            orgx = xcoord(k)
            orgy = ycoord(k)
            orgz = zcoord(k)

            xcoord(k) = orgx * quant(1, 1) + orgy * quant(1, 2) + orgz * quant(1, 3)
            ycoord(k) = orgx * quant(2, 1) + orgy * quant(2, 2) + orgz * quant(2, 3)
            zcoord(k) = orgx * quant(3, 1) + orgy * quant(3, 2) + orgz * quant(3, 3)
            k = k + 1
        Loop

        orgxc = xcenter
        orgyc = ycenter
        orgzc = zcenter

        xcenter = orgxc * quant(1, 1) + orgyc * quant(1, 2) + orgzc * quant(1, 3)
        ycenter = orgxc * quant(2, 1) + orgyc * quant(2, 2) + orgzc * quant(2, 3)
        zcenter = orgxc * quant(3, 1) + orgyc * quant(3, 2) + orgzc * quant(3, 3)

    End Sub

    Private Sub MenuItem12_Click(ByVal sender As System.Object, ByVal e As
System.EventArgs) Handles MenuItem12.Click

        g.Clear(Color.Gray)
        Call Rotate_Mol()
        Call Refresh_Graphic()

    End Sub

    Private Sub frmMain_Load(ByVal sender As System.Object, ByVal e As
System.EventArgs) Handles MyBase.Load

        g = Me.CreateGraphics
        Call Input_Conditions()


    End Sub

    Private Sub MenuItem9_Click(ByVal sender As System.Object, ByVal e As
System.EventArgs) Handles MenuItem9.Click
```

```
        g.Clear(Color.Gray)
        Dim frm As New Form2()
        frm.Show()

    End Sub

    Private Sub MenuItem13_Click(ByVal sender As System.Object, ByVal e As
System.EventArgs) Handles MenuItem13.Click

        g.DrawEllipse(areaPen, 0, 0, 500, 500)

        k = 1
        Do Until k = numatoms + 1

            xpos = xcoord(k) * 250 / maxrad + 250
            ypos = ycoord(k) * 250 / maxrad + 250
            atomradius = atomicradii(k) * 250 / maxrad
            xpos = xpos - atomradius
            ypos = ypos - atomradius

            g.FillEllipse(Brushes.Black, xpos, ypos, atomradius * 2, atomradius * 2)

            k = k + 1
        Loop



    End Sub

    Private Sub MenuItem14_Click(ByVal sender As System.Object, ByVal e As
System.EventArgs) Handles MenuItem14.Click

        Me.Cursor = Cursors.WaitCursor

        FileOpen(2, fileout, OpenMode.Output)

        numhits = 0
        Randomize()
        totalarea = 3.141592654 * maxrad ^ 2
        n = 1
        numrot = Int(1 / precision)
        Do Until n = numrot + 1
```

```
        Call Rotate_Mol()

        m = 1
        Do Until m = 5001
findxy:
            xrnd = (2 * Rnd() - 1) * maxrad
            xrnd = xrnd - xcenter
            yrnd = (2 * Rnd() - 1) * maxrad
            yrnd = yrnd - xcenter
            rsqr = maxrad ^ 2
            prodxy = xrnd ^ 2 + yrnd ^ 2

            If rsqr < prodxy Then
               GoTo findxy
            End If

            j = 1
            Do Until j = numatoms + 1
               radialval = Sqrt((xcoord(j) - xrnd) ^ 2 + (ycoord(j) - yrnd) ^ 2)
               If radialval <= atomicradii(j) + bufradius Then
                  numhits = numhits + 1
                  GoTo Iterations
               End If
               j = j + 1
            Loop
Iterations:
            m = m + 1
         Loop
         n = n + 1
      Loop
      molarea = totalarea * numhits / (5000 * numrot)
      atomden = totalmass / molarea
      WriteLine(2, totalmass, precision, molarea, atomden)

      FileClose(2)
      Me.Cursor = Cursors.Default
      g.Clear(Color.Gray)
      Dim frmout As New frmCross()
      frmout.Show()


   End Sub

   Private Sub CalCross()
```

```
        numhits = 0
        Randomize()
        totalarea = 3.141592654 * maxrad ^ 2
        n = 1
        numrot = Int(1 / precision)
        Do Until n = numrot + 1

           Call Rotate_Mol()

           m = 1
           Do Until m = 5001
findxy:
              xrnd = (2 * Rnd() - 1) * maxrad
              xrnd = xrnd - xcenter
              yrnd = (2 * Rnd() - 1) * maxrad
              yrnd = yrnd - xcenter
              rsqr = maxrad ^ 2
              prodxy = xrnd ^ 2 + yrnd ^ 2

              If rsqr < prodxy Then
                 GoTo findxy
              End If

              j = 1
              Do Until j = numatoms + 1
                 radialval = Sqrt((xcoord(j) - xrnd) ^ 2 + (ycoord(j) - yrnd) ^ 2)
                 If radialval <= atomicradii(j) + bufradius Then
                    numhits = numhits + 1
                    GoTo Iterations
                 End If
                 j = j + 1
              Loop
Iterations:
              m = m + 1
           Loop
           n = n + 1
        Loop
        molarea = totalarea * numhits / (5000 * numrot)
        atomden = totalmass / molarea
        'WriteLine(2, totalmass, precision, molarea, atomden)

     End Sub
```

```
    Private Sub OpenCarFile()

        With OpenCartDialog
            .CheckFileExists = True
            .ShowReadOnly = False
            .Filter = "All Files|*.*|Text Files|*.car"
            .FilterIndex = 2
            If .ShowDialog = DialogResult.OK Then
                cartfilename = OpenCartDialog.FileName
            Else : GoTo Cancel_Event1
            End If
        End With

        FileOpen(1, cartfilename, OpenMode.Input)
Cancel_Event1:

    End Sub

    Private Sub OpenOutputFile()

        FileOpen(2, "c:/download/test.txt", OpenMode.Output)

    End Sub

    Private Sub CloseCarFile()

        FileClose(1)

    End Sub

    Private Sub CloseOutputFile()

        FileClose(2)

    End Sub

    Private Sub MenuItem8_Click(ByVal sender As System.Object, ByVal e As
System.EventArgs) Handles MenuItem8.Click

        Call Input_Conditions()
        Call OpenCarFile()
        Call OpenOutputFile()

        Call ReadInCar()
```

```
        Call Mol_Info()
        Call Find_CM()
        Call Refresh_Graphic()

        Call CloseCarFile()
        Call CloseOutputFile()

Cancel_Event:

    End Sub

    Private Sub ReadInCar()

        Dim Atomlbl(5000) As String
        Dim xcoor As String
        Dim ycoor As String
        Dim zcoor As String
        Dim resname As String
        Dim resnum As String
        Dim atomlbl2 As String
        Dim atomicname(5000) As String
        Dim charge As String

        k = 1
        Do Until k = 5
            line = LineInput(1)
            k = k + 1
        Loop
        i = 1
        Do
            Atomlbl(i) = InputString(1, 7)
            If Atomlbl(i) Like "end*" Then
                GoTo ExitLoop
            Else
                xcoor = InputString(1, 15)
                xcoord(i) = Single.Parse(xcoor)
                ycoor = InputString(1, 15)
                ycoord(i) = Single.Parse(ycoor)
                zcoor = InputString(1, 14)
                zcoord(i) = Single.Parse(zcoor)
                resname = InputString(1, 5)
                resnum = InputString(1, 7)
                atomlbl2 = InputString(1, 8)
```

```
            atomicname(i) = InputString(1, 3)
            If atomicname(i) = "H  " Then
               atomicnum(i) = 1
            ElseIf atomicname(i) = "Li " Then
               atomicnum(i) = 3
            ElseIf atomicname(i) = "C  " Then
               atomicnum(i) = 6
            ElseIf atomicname(i) = "N  " Then
               atomicnum(i) = 7
            ElseIf atomicname(i) = "O  " Then
               atomicnum(i) = 8
            ElseIf atomicname(i) = "F " Then
               atomicnum(i) = 9
            ElseIf atomicname(i) = "Na " Then
               atomicnum(i) = 11
            ElseIf atomicname(i) = "P  " Then
               atomicnum(i) = 15
            ElseIf atomicname(i) = "S  " Then
               atomicnum(i) = 16
            ElseIf atomicname(i) = "Cl " Then
               atomicnum(i) = 17
            ElseIf atomicname(i) = "Cs " Then
               atomicnum(i) = 55
            ElseIf atomicname(i) = "Li " Then
               atomicnum(i) = 3
            Else
               Response = MessageBox.Show("One or more atoms not in registry",
"Warning", MessageBoxButtons.AbortRetryIgnore, MessageBoxIcon.Exclamation,
MessageBoxDefaultButton.Button1, MessageBoxOptions.DefaultDesktopOnly)
            End If
            charge = InputString(1, 8)
            'WriteLine(2, atomicname(i), atomicnum(i), xcoord(i), ycoord(i), zcoord(i))
            i = i + 1
         End If

      Loop


ExitLoop:

      line = LineInput(1)
      'WriteLine(2, line)
      numatoms = i - 1
      'WriteLine(2, numatoms)
```

```
End Sub

Private Sub Mol_Info()

   totalmass = 0
   i = 1
   Do Until i = numatoms + 1

      If atomicnum(i) = 1 Then
         amu(i) = 1.00794
         atomicradii(i) = 1.19
         atomPen(i) = pen1
      ElseIf atomicnum(i) = 2 Then
         amu(i) = 4.002602
         atomicradii(i) = 1.05
         atomPen(i) = pen5
      ElseIf atomicnum(i) = 3 Then
         amu(i) = 6.941
         atomicradii(i) = 1.25
         atomPen(i) = pen5
      ElseIf atomicnum(i) = 6 Then
         amu(i) = 12.011
         atomicradii(i) = 1.52
         atomPen(i) = pen2
      ElseIf atomicnum(i) = 7 Then
         amu(i) = 14.00674
         atomicradii(i) = 1.52
         atomPen(i) = pen3
      ElseIf atomicnum(i) = 8 Then
         amu(i) = 15.9994
         atomicradii(i) = 1.52
         atomPen(i) = pen4
      ElseIf atomicnum(i) = 9 Then
         amu(i) = 18.9984032
         atomicradii(i) = 1.27
         atomPen(i) = pen6
      ElseIf atomicnum(i) = 11 Then
         amu(i) = 22.989768
         atomicradii(i) = 1.76
         atomPen(i) = pen6
      ElseIf atomicnum(i) = 14 Then
         amu(i) = 28.0855
```

```
            atomicradii(i) = 1.75
            atomPen(i) = pen5
        ElseIf atomicnum(i) = 15 Then
            amu(i) = 30.973762
            atomicradii(i) = 1.75
            atomPen(i) = pen5
        ElseIf atomicnum(i) = 16 Then
            amu(i) = 32.066
            atomicradii(i) = 1.75
            atomPen(i) = pen6
        ElseIf atomicnum(i) = 17 Then
            amu(i) = 35.4527
            atomicradii(i) = 1.65
            atomPen(i) = pen6
        ElseIf atomicnum(i) = 53 Then
            amu(i) = 126.90447
            atomicradii(i) = 2.1
            atomPen(i) = pen5
        ElseIf atomicnum(i) = 55 Then
            amu(i) = 132.90543
            atomicradii(i) = 2.15
            atomPen(i) = pen5
        Else
            Response = MessageBox.Show("One or more atoms not in registry",
"Warning", MessageBoxButtons.AbortRetryIgnore, MessageBoxIcon.Exclamation,
MessageBoxDefaultButton.Button1, MessageBoxOptions.DefaultDesktopOnly)
        End If

        totalmass = totalmass + amu(i)
        i = i + 1

    Loop

End Sub

Private Sub Refresh_Graphic()

    'set up pane for graphics output

    g.Clear(Color.Gray)
    maxwidth = Me.Width
    maxheight = Me.Height
    areaPen.Width = 1
    g.DrawEllipse(areaPen, 0, 0, 500, 500)
```

```
        k = 1
        Do Until k = numatoms + 1

            xpos = xcoord(k) * 250 / maxrad + 250
            ypos = ycoord(k) * 250 / maxrad + 250
            atomradius = atomicradii(k) * 250 / maxrad
            xpos = xpos - atomradius
            ypos = ypos - atomradius
            g.DrawEllipse(atomPen(k), xpos, ypos, atomradius * 2, atomradius * 2)
            k = k + 1
        Loop

    End Sub

    Private Sub MenuItem15_Click(ByVal sender As System.Object, ByVal e As
System.EventArgs) Handles MenuItem15.Click

        Call Refresh_Graphic()

    End Sub

    Private Sub MenuItem16_Click(ByVal sender As System.Object, ByVal e As
System.EventArgs) Handles MenuItem16.Click

        g.Clear(Color.Gray)

        Call Array_Sort()

        k = 1
        Do Until k = numatoms + 1
            xpos = xcoord(k) * 250 / maxrad + 250
            ypos = ycoord(k) * 250 / maxrad + 250
            atomradius = atomicradii(k) * 250 / maxrad
            xpos = xpos - atomradius
            ypos = ypos - atomradius
            If atomicnum(k) = 1 Then
                atomcolor = Color.White
            ElseIf atomicnum(k) = 2 Then
                atomcolor = Color.Aqua
            ElseIf atomicnum(k) = 3 Then
                atomcolor = Color.Aqua
            ElseIf atomicnum(k) = 6 Then
                atomcolor = Color.Gray
```

```
        ElseIf atomicnum(k) = 7 Then
            atomcolor = Color.Blue
        ElseIf atomicnum(k) = 8 Then
            atomcolor = Color.Red
        ElseIf atomicnum(k) = 9 Then
            atomcolor = Color.Green
        ElseIf atomicnum(k) = 11 Then
            atomcolor = Color.LightGray
        ElseIf atomicnum(k) = 14 Then
            atomcolor = Color.LightGray
        ElseIf atomicnum(k) = 15 Then
            atomcolor = Color.LightGreen
        ElseIf atomicnum(k) = 16 Then
            atomcolor = Color.Yellow
        ElseIf atomicnum(k) = 17 Then
            atomcolor = Color.Green
        ElseIf atomicnum(k) = 53 Then
            atomcolor = Color.Green
        ElseIf atomicnum(k) = 55 Then
            atomcolor = Color.Orange
        Else
            atomcolor = Color.Aqua
        End If
        Call DrawSphere()

        k = k + 1
    Loop

End Sub

Public Sub DrawSphere()

    Dim obBrush As SolidBrush
    Dim obLBrush As LinearGradientBrush
    Dim obRect As Rectangle

    '//DRAW SPHERE.

    obBrush = New SolidBrush(atomcolor)
    obRect = New Rectangle()
    With obRect
        .X = xpos
        .Y = ypos
        .Width = atomradius * 2
```

```
        .Height = atomradius * 2
    End With
    obLBrush = New LinearGradientBrush(obRect, Color.Black, atomcolor, _
        LinearGradientMode.ForwardDiagonal)
    g.FillEllipse(obLBrush, obRect)


End Sub

Private Sub Array_Sort()

    Dim znum, ynum, xnum, atnum, atrad As Single

    For j = 2 To numatoms
        znum = zcoord(j)
        xnum = xcoord(j)
        ynum = ycoord(j)
        atnum = atomicnum(j)
        atrad = atomicradii(j)

        For k = j - 1 To 1 Step -1
            If zcoord(k) <= znum Then Exit For
            zcoord(k + 1) = zcoord(k)
            xcoord(k + 1) = xcoord(k)
            ycoord(k + 1) = ycoord(k)
            atomicnum(k + 1) = atomicnum(k)
            atomicradii(k + 1) = atomicradii(k)

        Next k
        If zcoord(k) > znum Then k = 0
        zcoord(k + 1) = znum
        xcoord(k + 1) = xnum
        ycoord(k + 1) = ynum
        atomicnum(k + 1) = atnum
        atomicradii(k + 1) = atrad
    Next j

End Sub

Private Sub MenuItem17_Click(ByVal sender As System.Object, ByVal e As
System.EventArgs) Handles MenuItem17.Click

    Dim numit As Integer
    Dim numfiles As Integer
```

```
        Dim filename(30) As String
        Dim OpenFilename As String

        numfiles = 1
        filename(1) = "VLTSAAK.car"
        filename(2) = "VSEALTK.car"
        filename(3) = "VVTDLTK.car"
        filename(4) = "WNMQNGK.car"
        filename(5) = "YLGEEYVK.car"
        filename(6) = "IDALNENK.car"
        filename(7) = "IGDYAGIK.car"
        filename(8) = "LIVTQTMK.car"
        filename(9) = "LVNELTEFAK.car"
        filename(10) = "LVNEVTEFAK.car"
        filename(11) = "MFLGFPTTK.car"
        filename(12) = "MFLSFPTTK.car"
        filename(13) = "MIFAGIK.car"
        filename(14) = "MLTAEEK.car"
        filename(15) = "NPDPWAK.car"

        Call Input_Conditions()
        Call OpenOutputFile()

        Me.Cursor = Cursors.WaitCursor

        Do

            OpenFilename = "C:\Documents and Settings\vgk\car_file\" +
filename(numfiles)
            FileOpen(1, OpenFilename, OpenMode.Input)


            numit = 1
            Do

                Call ReadInCar()
                Call Mol_Info()
                Call Find_CM()
                Call Refresh_Graphic()
                Call CalCross()
                WriteLine(2, filename(numfiles), numit, totalmass, precision, molarea,
atomden)
                numit = numit + 1
```

```
            Loop Until EOF(1)

            numfiles = numfiles + 1
            FileClose(1)

        Loop Until numfiles = 15

        Call CloseOutputFile()
        Me.Cursor = Cursors.Default

    End Sub

End Class
```

VITA

GUIDO FRIDOLIN VERBECK, IV

Home Address:
1449 Overton Lane
Knoxville, TN 37923

EDUCATION

Texas A&M University, Department of Chemistry, College Station, TX
Ph.D. (August 2004), Advisor: Dr. David H. Russell, GPA – 3.8/4.0

University of Alabama at Birmingham, Department of Chemistry, Birmingham, AL
M.S. (May 1999), Advisor: Dr. Stephen C. Beale, GPA – 3.3/4.0

Northeast Louisiana University, Department of Chemistry, Monroe, LA
B.S. (December 1996), GPA – 3.2/4.0

EXPERIENCE

1999-2003
GRADUATE RESEARCH ASSISTANT
Texas A&M Univeristy, Department of Chemistry, College Station, TX

1997-1999
GRADUATE RESEARCH ASSISTANT
University of Alabama at Birmingham, Department of Chemistry, Birmingham, AL

1995-1996
QUALITY CONTROL CHEMIST
ANGUS Chemical Company, Inc., Sterlington, Louisiana

HONORS AND AWARDS

- George Kuntz Fellowship, Office of Graduate Studies, Texas A&M University, Fall 2003
- Procter & Gamble Fellowship, Department of Chemistry, Texas A&M University, 2002-2003
- Eagle Scout, Boy Scouts of America, 1988

PROFESSIONAL AFFILIATIONS

- Sigma Xi Professional Research Society
- American Chemical Society